

Travail de fin d'études et stage[BR]- Travail de fin d'études : Design of Hybrid Composites for FS Race Car Monocoques :An Experimental and Numerical Approach[BR]- Stage

Auteur : Iserentant, Tanguy

Promoteur(s) : Béchet, Eric; Bruyneel, Michaël

Faculté : Faculté des Sciences appliquées

Diplôme : Master en ingénieur civil mécanicien, à finalité spécialisée en technologies durables en automobile

Année académique : 2023-2024

URI/URL : <http://hdl.handle.net/2268.2/20877>

Avertissement à l'attention des usagers :

Tous les documents placés en accès ouvert sur le site le site MatheO sont protégés par le droit d'auteur. Conformément aux principes énoncés par la "Budapest Open Access Initiative"(BOAI, 2002), l'utilisateur du site peut lire, télécharger, copier, transmettre, imprimer, chercher ou faire un lien vers le texte intégral de ces documents, les disséquer pour les indexer, s'en servir de données pour un logiciel, ou s'en servir à toute autre fin légale (ou prévue par la réglementation relative au droit d'auteur). Toute utilisation du document à des fins commerciales est strictement interdite.

Par ailleurs, l'utilisateur s'engage à respecter les droits moraux de l'auteur, principalement le droit à l'intégrité de l'oeuvre et le droit de paternité et ce dans toute utilisation que l'utilisateur entreprend. Ainsi, à titre d'exemple, lorsqu'il reproduira un document par extrait ou dans son intégralité, l'utilisateur citera de manière complète les sources telles que mentionnées ci-dessus. Toute utilisation non explicitement autorisée ci-avant (telle que par exemple, la modification du document ou son résumé) nécessite l'autorisation préalable et expresse des auteurs ou de leurs ayants droit.



Master's Thesis
for the degree of Master of Science in Mechanical Engineering
with specialization in Sustainable Automotive Engineering

Design of Hybrid Composites for FS Race Car Monocoques:
An Experimental and Numerical Approach

Author

Tanguy Iserentant

Supervisors

Professor Eric Béchet
University of Liège

Professor Michaël Bruyneel
University of Liège

The Formula Student competition challenges student teams worldwide to design, build, and race single-seater formula racing cars, pushing the limits of innovation in automotive engineering. As ecological concerns become increasingly prominent, the need for greener materials in high-performance vehicles is essential. This thesis focuses on the design of a more sustainable hybrid composite lay-up for a Formula Student race car monocoque, aiming to achieve mechanical properties comparable to traditional carbon fiber while maintaining a similar weight. The research introduces flax fibers as a natural alternative, integrated into carbon-flax hybrid composites that exhibit enhanced crashworthiness, especially in critical zones such as the front bulkhead. For safety reasons, all these composite parts of the monocoque that may be subjected to impact must undergo perimeter shear testing.

The investigation was structured into two primary components. The first component involved an experimental study assessing the influence of stacking sequence and flax fiber mass fraction on the mechanical properties of the hybrid composites. Vacuum-assisted resin infusion was employed to manufacture high-quality samples, while perimeter shear tests were conducted to evaluate their resistance to puncture and impact. Results indicated that hybrid composites with flax fibers placed in the outer layers, and alternating carbon and flax fibers within the lay-up, demonstrated superior resistance compared to traditional carbon fiber composites. A specific configuration achieved a peak force of 27454 [N] with just 10 layers, thus allowing the theorization of hybrid configurations for the front bulkhead, leading to a reduction in its mass of 22% and its CO₂ footprint by over 43% compared to the current lay-up.

The second component of the research focused on developing a reliable numerical model to simulate the perimeter shear test using Ansys. The model was designed to replicate experimental conditions, and the objective was to obtain the force-displacement curves from multistep simulations and determine the first ply failure of the sample. The simulation incorporated frictional contacts and accounted for large deflections, achieving a high degree of accuracy in predicting force-displacement curves. Therefore, the dependency on extensive laboratory testing is reduced and valuable insights into stress distribution are provided.

All the steps related to a new testing strategy have been thoroughly covered in this work, from the lay-up design to experimental testing, including numerical simulations and sample fabrication. The conclusions of this thesis suggest that carbon-flax hybrid composites are promising materials for use in critical areas of a monocoque structure, such as the front bulkhead, which are subjected to high impact loads and that must resist perforation. Although these results are promising, further research is required to refine the damage modeling and optimize the hybrid composite properties for practical applications in Formula Student vehicles.

Keywords: Hybrid composites | Carbon fiber | Flax fiber | Perimeter shear test | Damages modeling

Acknowledgements

First and foremost, I would like to express my gratitude to my academic supervisors, Professors Michaël Bruyneel and Eric Béchet, for all the support they provided during this internship. The numerous meetings spent trying to solve my challenges were immensely helpful, and I am deeply appreciative of the time they dedicated to me.

Next, I would like to thank Simon Verstraete and Manu Santermans (Formula Electric Belgium) for supervising and assisting me over the past six months. Their advice and expertise in composite material manufacturing allowed me to thrive in this fascinating subject. I would also like to express my gratitude to Gurleen, Tijs, Jordy, Wim, and, of course, the entire team for all the little help and the moments we shared together. It was an extraordinary experience working in the field of motorsport.

I certainly cannot forget to thank Antoine, William, Émile, and Thiébaud for their support and encouragement during this period, which was not always easy. Thank you for your help and for the years we spent together.

I would also like to acknowledge all my friends, from Herve to Bologna, who will have the courage to read this thesis!

Enfin, je tiens à exprimer un immense remerciement à ma famille qui m'a aidé et soutenu durant toutes ces années. Jamais je n'aurais pu y parvenir sans votre soutien, malgré toutes ces heures de travail. Je me rends compte de la chance que j'ai eue d'être soutenu de cette manière, d'avoir pu réaliser les études de mes rêves à Bologne, mais aussi d'avoir pu déménager pendant six mois à Leuven. Merci pour tout, je vous aime.

Contents

1	Introduction	1
1.1	Context	1
1.2	Carbon fiber and sustainability	3
1.3	Monocoque design	4
1.4	Objectives	6
2	Materials study	10
2.1	Material choice	10
2.2	Structure and composition of composites	14
2.3	Mechanics of composite	16
2.3.1	Classical lamination theory	16
2.3.2	Failure criteria and damage mechanisms	20
2.3.3	Material damages modeling	23
2.4	Analysis of carbon-flax hybrid composites	24
2.4.1	Tensile properties	25
2.4.2	Bending properties	25
2.4.3	Impact properties	26
2.5	Conclusion	27
3	Design and analysis of hybrid composites	28
3.1	Manufacturing process	28
3.1.1	Prepreg compression molding	29
3.1.2	Prepreg autoclave curing	30
3.1.3	Vacuum-assisted resin infusion	30
3.2	Analysis of hybridization	31
3.2.1	Influence of fibers orientation and of material selection.	36
3.2.2	Influence of the stack-up sequence and flax fiber mass fraction.	37
3.2.3	Advanced hybrid stack-up sequences	43
3.3	Conclusion	47
4	Numerical model of the perimeter shear test	49
4.1	Modeling and parameterization	49
4.1.1	Geometry	50
4.1.2	Mesh	51
4.1.3	Contact definition	54
4.1.4	Boundary conditions and number of solution steps	55
4.1.5	Solver parameters	56

4.2	Simulation parameters calibration	56
4.2.1	Contact calibration	58
4.2.2	Analysis of the number of solution steps	63
4.2.3	Mesh convergence analysis	64
4.3	Damage parameters calibration	66
4.3.1	Calibration process	67
4.3.2	Analysis of the results	70
4.4	Flax fiber parameters calibration	78
4.4.1	Calibration process	79
4.4.2	Analysis of the results	80
4.5	Conclusion	84
5	Conclusion	85

List of Figures

1.1	The Formula Electric Belgium team for the 2023-2024 year.	2
1.2	Comet.	3
1.3	Schematic representation of monocoque zones.	5
1.4	Illustration of a sandwich structure.	5
1.5	Model of the monocoque of Comet.	7
1.6	Isometric view of the perimeter shear test, units in [mm]. From [19].	8
1.7	Results of the perimeter shear test on the FBH, showing the evolution of force with respect to displacement.	9
1.8	Test strategy for composite materials applied to the FBH.	9
2.1	Front impact absorbing structure in flax fiber. From [18].	11
2.2	Material selection for fibers for maximizing the specific stiffness and minimizing the CO ₂ footprint. Synthetic fibers are in black and natural fibers in beige.	12
2.3	Material selection for fibers for maximizing the specific tensile strength and minimizing the CO ₂ footprint. Synthetic fibers are in black and natural fibers in beige.	12
2.4	Material selection for fibers for maximizing the specific elongation and minimizing the CO ₂ footprint. Synthetic fibers are in black and natural fibers in beige.	13
2.5	Unidirectional ply. From [25].	15
2.6	Plain weave ply. From [25].	15
2.7	Twill 2x2 ply. From [25].	15
2.8	Unidirectional ply with its axis systems. From [25].	16
2.9	Stacking of plies. From [25].	19
2.10	Ply modulus as a function of the ply angle. Adapted from [27].	19
2.11	Failure modes in composites. Adapted from [25].	21
2.12	Comparison of the different failure envelopes defined by the failure criteria. From [31].	23
2.13	Representation of the effects of damage on a ply. From [25].	24
2.14	Representation of the effects of damage on a laminate. From [25].	24
2.15	Specific energy absorption energy for an impact test of 25 [J]. Adapted from [37]. . .	27
3.1	Sample that was not fully cured.	29
3.2	Vacuum-assisted resin infusion setup.	31
3.3	Illustration of the vacuum-assisted resin infusion setup.	31
3.4	Illustration of the stack-up sequences of samples 1 and 2.	32
3.5	Illustration of the stack-up sequences of samples 5.	35
3.6	Force-displacement curves of experimental data for samples 3. The displacements are normalized.	37
3.7	Force-displacement curves of experimental data for samples 4a. The displacements are normalized.	37

3.8	Force-displacement curves of experimental data for samples 6a. The displacements are normalized.	37
3.9	Force-displacement curves of experimental data for samples 6b. The displacements are normalized.	37
3.10	Force-displacement curves of experimental data for samples 1a. The displacements are normalized.	38
3.11	Force-displacement curves of experimental data for samples 1b. The displacements are normalized.	39
3.12	Force-displacement curves of experimental data for samples 1c. The displacements are normalized.	39
3.13	Force-displacement curves of experimental data for samples 2a. The displacements are normalized.	40
3.14	Force-displacement curves of experimental data for samples 2b. The displacements are normalized.	40
3.15	Force-displacement curves of experimental data for samples 2c. The displacements are normalized.	41
3.16	Force-displacement curves of experimental data for samples 4b. The displacements are normalized.	41
3.17	Bottom view of the sample 2a.	43
3.18	Force-displacement curves of experimental data for samples 5a. The displacements are normalized.	43
3.19	Force-displacement curves of experimental data for samples 5b. The displacements are normalized.	44
3.20	Force-displacement curves of experimental data for samples 5c. The displacements are normalized.	44
3.21	Force-displacement curves of experimental data for samples 5d. The displacements are normalized.	45
3.22	Force-displacement curves of experimental data for samples 5e. The displacements are normalized.	45
3.23	Bottom view of the sample 5e.	47
4.1	Sample under experimental conditions for the perimeter shear test.	50
4.2	3D geometric model of the perimeter shear test.	51
4.3	Side view of the geometric model.	51
4.4	Central zone of the sample.	52
4.5	Intermediate zone of the sample.	52
4.6	Outer zone of the sample.	53
4.7	Central zone of the support.	53
4.8	Outer zone of the support.	53
4.9	Mesh of the plate.	53
4.10	Mesh of the support.	53
4.11	Isometric view of the meshed assembly.	54
4.12	Boundary conditions and contacts.	54
4.13	Sample 7.	57
4.14	Bonded edge for contact between the sample and the support.	58
4.15	Bonded edge for contact between the support and the sample.	58

4.16	Surface defined for bonded and frictional contact between the sample and the load applicator.	59
4.17	Isometric view of the new geometry.	61
4.18	Surface defined for frictional contact between the sample and the support.	61
4.19	Surface defined for frictional contact between the support and the sample.	61
4.20	Force-displacement curves for different types of simulations compared with experimental curves for samples 7. Displacement are normalized.	62
4.21	Displacement for Bonded-Bonded contacts without considering large deflection. . .	62
4.22	Displacement for Friction-Friction contacts, considering large deflections.	62
4.23	Buckling phenomenon observed during an experimental test of samples 7.	63
4.24	New mesh of the support.	65
4.25	Isometric view of the new mesh.	65
4.26	Maximum displacement as a function of the number of elements.	65
4.27	Maximum Von Mises stress as a function of the number of elements.	65
4.28	Variation of the Von Mises stress along the path.	66
4.29	Path corresponding to the median of the plate.	66
4.30	Von Mises stress in the ply from which the path was extracted.	66
4.31	Force-displacement curves for different types of simulations compared with experimental curves for samples 8c. Displacement are normalized.	69
4.32	Force-displacement curves for different types of simulations compared with experimental curves for samples 8a. Displacement are normalized.	70
4.33	Force-displacement curves comparing the simulation results with experimental data for samples 8b. The displacements are normalized.	71
4.34	Force-displacement curves comparing the simulation results with experimental data for samples 8c. The displacements are normalized.	71
4.35	Force-displacement curves comparing the simulation results with experimental data for samples 8d. The displacements are normalized.	72
4.36	Displacement. Top view of sample 8a.	73
4.37	Displacement. Side view of sample 8a.	73
4.38	Displacement. Top view of sample 8b.	73
4.39	Displacement. Side view of sample 8b.	73
4.40	Displacement. Top view of sample 8c.	73
4.41	Displacement. Side view of sample 8c.	73
4.42	Displacement. Top view of sample 8d.	74
4.43	Displacement. Side view of sample 8d.	74
4.44	Von Mises stress. Top view of sample 8a.	74
4.45	Von Mises stress. Bottom view of sample 8b.	74
4.46	Von Mises stress. Top view of sample 8b.	74
4.47	Von Mises stress. Bottom view of sample 8b.	74
4.48	Von Mises stress. Top view of sample 8c.	75
4.49	Von Mises stress. Bottom view of sample 8c.	75
4.50	Von Mises stress. Top view of sample 8d.	75
4.51	Von Mises stress. Bottom view of sample 8d.	75
4.52	Von Mises stress. Cross-sectional view of sample 8c	75
4.53	Max stress criterion inverse reserve factor. Top view of sample 8c.	76
4.54	Max stress criterion inverse reserve factor. Bottom view of sample 8c.	76
4.55	Tsai-Wu criterion inverse reserve factor. Top view of sample 8c.	76

4.56	Tsai-Wu criterion inverse reserve factor. Bottom view of sample 8c.	76
4.57	Tsai-Wu criterion inverse reserve factor. Top view of sample 8a.	76
4.58	Tsai-Wu criterion inverse reserve factor. Bottom view of sample 8a.	76
4.59	Tsai-Wu criterion inverse reserve factor. Top view of sample 8b.	77
4.60	Tsai-Wu criterion inverse reserve factor. Bottom view of sample 8b.	77
4.61	Tsai-Wu criterion inverse reserve factor. Top view of sample 8d.	77
4.62	Tsai-Wu criterion inverse reserve factor. Bottom view of sample 8d.	77
4.63	Top view of the sample 8c.	77
4.64	Bottom view of the sample 8c.	77
4.65	Force-displacement curves for different types of simulations compared with experi- mental curves for samples 6a. Displacement are normalized.	80
4.66	Force-displacement curves comparing the simulation results with experimental data for samples 6a. The displacements are normalized.	81
4.67	Force-displacement curves comparing the simulation results with experimental data for samples 6b. The displacements are normalized.	81
4.68	Displacement. Top view of sample 6a.	82
4.69	Displacement. Side view of sample 6a.	82
4.70	Displacement. Top view of sample 6b.	82
4.71	Displacement. Side view of sample 6b.	82
4.72	Von Mises stress. Top view of sample 6a.	82
4.73	Von Mises stress. Bottom view of sample 6a.	82
4.74	Von Mises stress. Top view of sample 6b.	83
4.75	Von Mises stress. Bottom view of sample 6b.	83
4.76	Von Mises stress. Cross-sectional view of sample 6a.	83
4.77	Tsai-Wu criterion inverse reserve factor. Top view of sample 6a.	83
4.78	Tsai-Wu criterion inverse reserve factor. Bottom view of sample 6a.	83
4.79	Tsai-Wu criterion inverse reserve factor. Top view of sample 6b.	84
4.80	Tsai-Wu criterion inverse reserve factor. Bottom view of sample 6b.	84
4.81	Top view of the sample 6b.	84
4.82	Bottom view of the sample 6b.	84

List of Tables

2.1	Main mechanical properties of selected materials. The data are exported from Granta EduPack.	13
3.1	Stack-up sequence and thickness of the samples 1 and 2 produced.	32
3.2	Mass properties of the samples 1 and 2 produced.	33
3.3	Stack-up sequence and thickness of the samples 3 and 4 produced.	34
3.4	Mass properties of the samples 3 and 4 produced.	34
3.5	Stack-up sequence and thickness of the samples 5 produced.	34
3.6	Mass properties of the samples 5 produced.	35
3.7	Stack-up sequence and thickness of the samples 6 produced.	36
3.8	Mass properties of the samples 6 produced.	36
3.9	Mass properties of the samples 1 and 2 produced.	42
3.10	Mass properties of the samples 5 produced.	46
4.1	Main mechanical properties of the selected material. The data are exported from ESAComp.	57
4.2	Lay-up and thickness of the samples 7 produced and used for simulations.	57
4.3	Comparison of the results obtained by varying the number of solution steps in a simulation with frictional contacts. All other simulation parameters are identical to those presented in Section 4.2.1. Von Mises stresses are used as an equivalent stress for comparison.	63
4.4	Representation of various mesh configurations used in the convergence study.	64
4.5	Main mechanical properties of selected materials. The data are exported from ESAComp and Hexcel datasheets [63]. The data with * correspond to values corrected from experiments.	67
4.6	Lay-up and thickness of the samples 8 produced and used for simulations.	68
4.7	Damage variables for woven and unidirectional CFRP plies.	68
4.8	Main mechanical properties of selected materials. The data are selected from different articles [22, 23, 65, 66].	78
4.9	Lay-up and thickness of the samples 6 produced and used for simulations. The thickness is determined here by ACP.	79
4.10	Damage variables for woven FRP plies.	79

List of symbols

Prepreg: Pre-impregnated

CFRP: Carbon Fiber-Reinforced Polymer

FBH: Front Bulkhead

UD: Unidirectional

FPF: First ply failure

HFRP: Hybrid Fiber-Reinforced Polymers

FFRP: Flax Fiber-Reinforced Polymers

ACP: Ansys Mechanical Composite PrepPost

LD: Large Deflection

CHAPTER 1

Introduction

Today, the automotive world is undergoing a revolution. From the engine to the chassis, new sustainability requirements are being added to performance and safety constraints, pushing the limits of innovation. Motorsport has always been the driving force behind this innovation, gradually incorporating the most advanced technologies into everyday vehicles. Therefore, the engineers of tomorrow have a role to play in this transition, embodying the spirit of innovation, teamwork, and sustainability that is at the heart of Formula Student.

1.1 Context

Formula Student

Formula Student is an international design competition originally created by the Institution of Mechanical Engineers in 1998. The concept behind this competition is that teams of students develop and manufacture a single-seater formula racing car based on a series of rules, and then challenge university teams from all around the world during events that take place on famous racetracks during summer [1].

These teams are considered by the motorsport industry as the benchmark for engineering graduates to attain, transitioning them from university to a competitive workplace [2]. Indeed, students have only nine months and a limited budget to design from scratch a high performance and reliable car, which needs to be innovative. The competition involves combustion cars as well as electric cars and is not only a race on track. During several days, the car is subjected to different tests called static events. During this first phase of the competition, judges will analyze the design of the car, the business strategy, the sustainability, and creativity of the solutions, as well as safety through the scrutineering. The dynamic events are the second phase of the competition and require a qualification provided by the scrutineers. It is composed of different disciplines like the skid pad, the acceleration, the autocross, the endurance, and the energy efficiency that permit to evaluate the performances and the reliability of the car. It is evident, then, that Formula Student primarily stands as an engineering competition, where design exerts a far greater influence than the drivers themselves.

Formula Electric Belgium

Formula Electric Belgium is a student-based race team from Katholieke Universiteit Leuven that pushes green innovation to performance. Indeed, the philosophy guiding the car development is to

promote ecological interests through electric mobility, innovation, and education. For that, the team is composed of 6 departments which are Composites, Aerodynamics, Electronics, Vehicle Dynamics, Powertrain and Driverless. The research and development of the innovative technologies that will equip the next generation of cars is mostly done by master's theses. The team also highlights the opportunity for the students to gain practical experience and to improve their social skills.

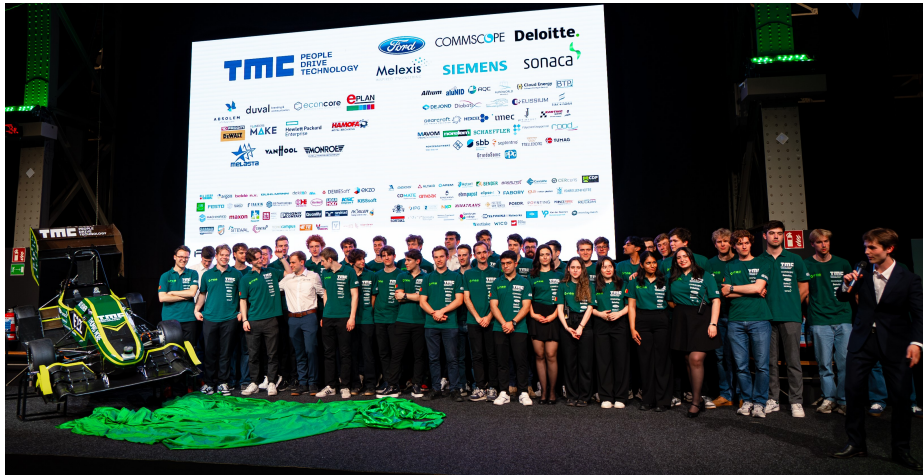


Figure 1.1: The Formula Electric Belgium team for the 2023-2024 year.

Comet

Comet is the 10th and most recent electric race car from Formula Electric Belgium. It is an open-wheel car powered by four customized asynchronous motors and a 600 [V] LiPo battery. The design philosophy of a Formula Student car revolves around creating a high-performance, lightweight, and agile vehicle that can compete effectively in Formula Student competitions where racetracks are always narrow and very sinuous. Therefore, in order to optimize grip, a semi-active-suspension and a full aerodynamic package were implemented. The chassis is a monocoque made of carbon/epoxy pre-impregnated fibers composing a sandwich structure. A special feature of this car is that it is also autonomous using a LiDAR technology.

Despite being compact, Comet has a maximum power of 140 [kW] and reaches 100 [km/h] in under 2.5 [s] thanks to its lightweight design, weighing just 224 [kg], 31.8 [kg] of which just for the monocoque. However, the high performances on track are not the only important achievement of Comet. Indeed, promoting green innovation was another significant objective of the design. By utilizing 3D-printed recyclable molds instead of aluminum-machined molds, CO₂ emissions for mold production were reduced by 90%. Additionally, thanks to the incorporation of flax fiber wings, the environmental impact of these wings was reduced by 20% compared to carbon fiber ones [3].



Figure 1.2: Comet.

1.2 Carbon fiber and sustainability

Nowadays, carbon fiber reinforced polymer (CFRP) is used in a multitude of advanced applications of aerospace and automotive sectors where high stiffness and strength, lightweight and great fatigue characteristics are critical requirements. However, this highly engineered materials is a relatively recent discovery, since it was accidentally created in 1958 by Roger Bacon. Its first industrial application was in 1968 on Rolls-Royce RB-211 turbofan engines that had carbon fiber composite compressor blades, but it was quickly demonstrated that carbon fiber was too brittle when subjected to impact [4] due to the low interlaminar shear strength and the materials' lack of strain-to-failure [5].

Although the first few applications of CFRP were for aerospace, the automotive industry has also played a key role in the development of carbon fiber. Indeed, in 1981, McLaren used for the first time in history CFRP to design a Formula One monocoque that was much stronger and lighter than classical aluminium chassis. This advancement has thus enabled better performance and an increase of safety, allowing carbon fiber monocoques to become standard equipment in motorsport [6]. However, the last decade has shown a focus of the automotive industry on innovative lightweight technologies to reduce emissions of road-cars and increase the autonomy of electric vehicles. CFRP was once again the solution to this problem, since it can reduce the weight of a vehicle without compromising strength and durability, permitting therefore a high crashworthiness. Formula Electric Belgium designed its first CFRP monocoque in 2015 thus allowing a decrease in mass of 40% compared to the old steel frame.

Despite all these advantages and its contribution to the ecological transition of the automotive industry, it is difficult to characterize carbon fiber as a sustainable material due to the following reasons:

- **Production is energy-intensive:** Stabilization and carbonization are two manufacturing processes that require a big quantity of energy and produce CO₂ emissions. Indeed, the production of 1 [kg] of carbon fiber induces 29.1 [kg CO₂ eq.] and 59% of these emissions are linked solely to the above-mentioned processes. Moreover, it is estimated that 464.2 [MJ] of fossil resources are consumed for the production of 1 [kg] of carbon fiber, including 48% just for the manufacturing processes [7].
- **Non-renewable raw materials:** Polyacrylonitrile is a non-renewable synthetic polymer resin used as raw material for the carbon fiber and derived from petrochemicals. It is responsible for 50% of the consumption of the fossil resources in carbon fiber production and for 37% of the total CO₂ emissions [7].
- **Limited recyclability and not biodegradable:** Due to its high performances, epoxy is the most used matrix for CFRP. However, this latter is a thermoset resin which, once hardened, cannot be melted and reshaped. This makes their recycling more difficult compared to thermoplastic materials. Moreover, carbon fibers and epoxy are not biodegradable and can therefore not be naturally decomposed when they reach the end of their industrial use [4].

In recent years, extensive research has been conducted to reduce the environmental impact of carbon fiber, particularly by substituting it with natural fibers that require less energy to manufacture, absorb CO₂ and emit O₂ during cultivation. Combined with bio epoxy, natural fibers permit to obtain composite materials that are biodegradable and more sustainable [8]. As previously explained, with the same goal of green innovation, Formula Electric Belgium has already used flax fiber in the past to reduce the environmental impact of the wings. However, unlike the monocoque, these parts are not structural parts and are not the most consuming in terms of carbon fiber quantity.

1.3 Monocoque design

A monocoque can be defined as a "*fabricated structural assembly made of composite materials that supports all functional vehicle systems*" [9]. The dimensions are induced by the functional limitations and the rule-book [9]. The design itself aims to minimize the weight while maximizing the following characteristics:

- **Stiffness:** This parameter has a great influence on the car's handling, since it permits to decrease the deformation of the chassis when it is submitted to road loads and therefore allows the suspension system to have a better control of the kinematics of the car [10].
- **Crashworthiness:** It relates to the ability of the monocoque to protect the pilot during an impact. High strength, energy absorption capacity and toughness of the different parts of the monocoque are therefore vital parameters. Indeed, it is important to have a structure that is able to absorb the energy of the impact without failing in a brittle manner [11].

To achieve these objectives, a zone based lay-up optimization is used. As it can be seen in Figure 1.3, the monocoque is divided into separate structural zones in the form of a sandwich structure

and by optimizing the orientation and stacking sequence of carbon fibers, the material's mechanical properties can be tailored to meet specific design requirements. Since the monocoque does not need the same material properties in each direction, each of the zones has its own lay-up and the more there are layers of carbon fiber, the higher the strength [12].

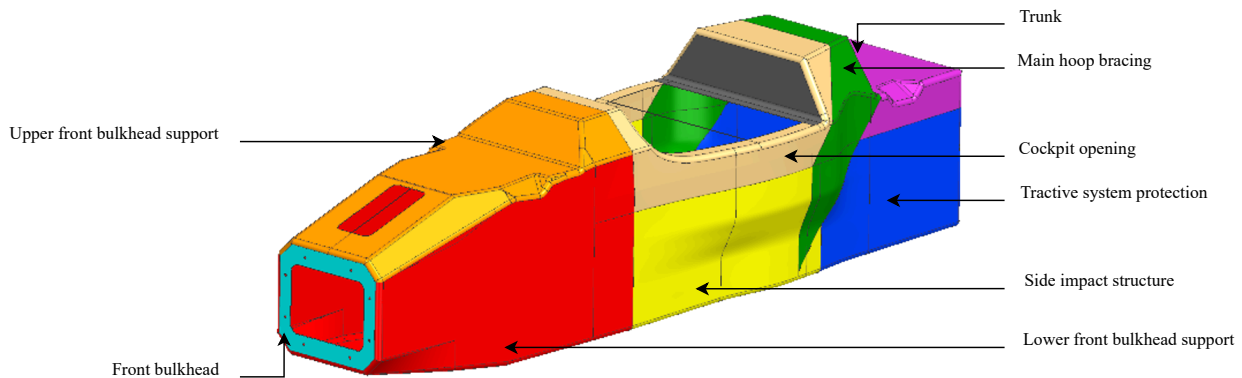


Figure 1.3: Schematic representation of monocoque zones.

The sandwich structure illustrated in Figure 1.8 is composed of few layers of carbon/epoxy pre-impregnated fibers (prepreg), a core and after few layers of carbon/epoxy prepreg again. The core of the sandwich structure significantly increases the overall thickness of the assembly, consequently exerting a substantial impact on its stiffness while keeping the weight low [13]. It permits the CFRP layers to have a better resistance to the buckling, the wrinkling, the out-of-plane shear and at the same time to take up the in-plane loads. Two core materials are used in the monocoque:

- **Aluminium honeycomb:** This anisotropic core is used in the majority of the monocoque, thanks to its high stiffness and strength in the perpendicular direction to the faces. The smaller the cell sizes, the higher the performance of the honeycomb and its adhesion to the carbon fiber will be [12].
- **Balsa wood:** For some parts subjected to high shear loads, this anisotropic material is used. Indeed, its shear capability out-of-plane does not change with direction, since the grain of the wood is oriented in the transverse direction [13].



Figure 1.4: Illustration of a sandwich structure.

Knowing that, it is therefore the choice of the core material, fibers orientation, and the number of layers that will mainly determine the mechanical properties of each area of the monocoque. For

safety reasons, all the composite parts of the primary structure must be tested following the Formula Student rule-book [9] to prove their equivalence with respect to steel structures. Indeed, for each zone defined of the monocoque, a three point bending test permit to measure the stiffness, the deflection and the energy absorption of representative samples of the lay-up. However, for zones that can be subjected to impacts, a perimeter shear test must also be carried out to measure the displacement and force corresponding to a puncture of the sample.

Recently, the advent of composites using natural fibers has highlighted their great toughness, which helps prevent brittle-like crash behavior under high strain loads [8, 14]. As a result, it is now possible to design hybrid composite that combine the strength of carbon fibers with tougher natural fibers, permitting hybrid composites to remain functional even when overloaded [15]. These characteristics are therefore promising for the design of high crashworthiness monocoques.

1.4 Objectives

The aim of this work is to find a more sustainable composite lay-up for a Formula Student race car monocoque, allowing for mechanical properties equivalent to carbon fiber while maintaining a similar weight. Flax fibers will be used in order to create a hybrid composite with a high crashworthiness. To achieve this objective, two sub-goals are defined and will be presented in this section in order to answer to the two main research questions:

- **What is the influence of the stacking sequence and flax fiber mass fraction on the properties of hybrid composites?**
- **How to construct a reliable numerical model of the perimeter shear test to permit a better understanding of the stress distribution and limit the laboratory tests?**

Design of a hybrid lay-up for the front bulkhead

The front bulkhead (FBH) is located at the very front of the monocoque and is defined as "*a planar structure that defines the forward plane of the chassis and provides protection for the driver's feet*" [9]. It is connected to the impact attenuator by the anti intrusion plate that covers the feet of the driver. This part of the monocoque is the first to be affected in the event of a frontal impact. Due to the large amount of energy dissipated during this type of impact, it is therefore important that this part has a high crashworthiness. Based on the experimental results of the 3-point bending test and the shear test, the current solution has been defined as a sandwich structure using 13 layers of carbon fiber, 20 [mm] of balsa wood and 13 layers of carbon fiber again. Knowing that the rule T3.4.3 declares that maximum weight content of parallel fibers, relative to the weight of all fibers in the laminate, is 50% [9], the orientation and quantity of woven fabric and unidirectional (UD) plies were therefore defined to maximize the performance of the laminate while minimizing the weight. Despite this optimization, the FBH is still the area of the monocoque with the most carbon fiber layers, which negatively impacts the weight of this part.

In recent years, Bcomp, a pioneering company in the field of natural fibers, has shown that flax fiber can play an important role in structural and safety-critical parts through partnerships with BMW [16], Porsche [17], and YCOM [18]. Based on these results and considering the role of the FBH, it was decided to investigate the possibility of using natural fibers in the design of its lay-up

to take advantage of the toughness and impact absorption benefits of this type of fiber, with the aim of reducing the weight and environment cost of the FBH. Although this work will focus on defining a lay-up for the FBH, it is clear that future conclusions could be applied to other parts of the monocoque. Chapter 2 will first present a brief state of the art on composite materials made from natural fibers, and then discuss the properties of these composites established through standardized tests. The design of natural and hybrid composite lay-ups will be detailed in Chapter 3, with the aim of optimizing their performance during the shear test.

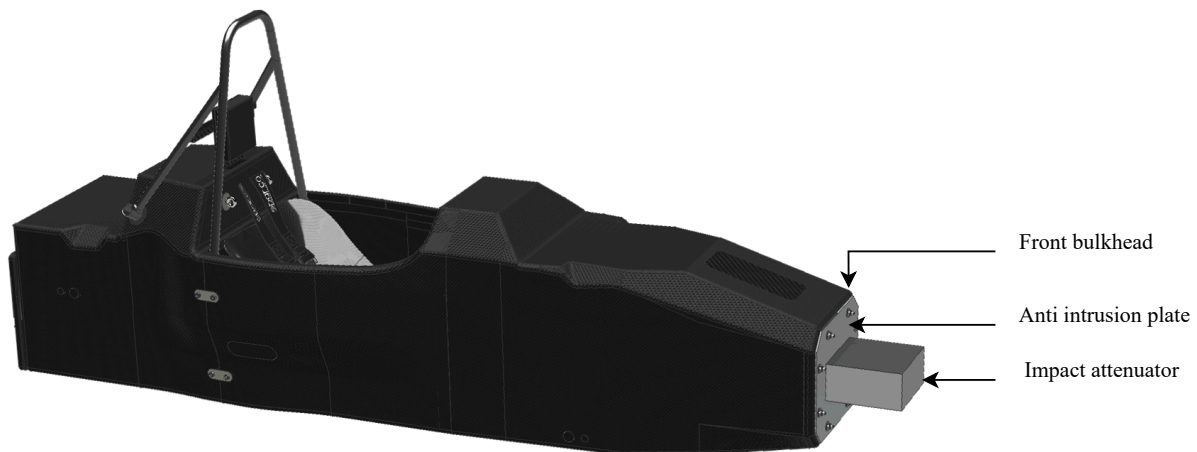


Figure 1.5: Model of the monocoque of Comet.

Construction of a numerical model of the perimeter shear test

For the areas of the monocoque that may be subjected to impacts, such as the FBH, the perimeter shear test is the most challenging. Therefore, this test will have the most significant influence on the lay-up design. According to the rule-book, *"the perimeter shear tests must be completed which measure the force required to push or pull a 25 mm diameter flat punch through a flat laminate sample. The sample must be at least 100 mm×100 mm. Core and skin thicknesses must be identical to those used in the actual primary structure and be manufactured using the same materials and processes. The test fixture must support the entire sample, except for a 32 mm hole aligned co-axially with the punch. The sample must not be clamped to the fixture."* [9]. In this way, it is possible to subject the sample to shear in all directions and measure the material's resistance to penetration, ensuring that the part is strong enough to ensure the anti-intrusion plate remains securely in place during an impact. Moreover, it permits to verify the attachment strength, which relates to strength of joints or mechanical fasteners used to attach different parts of a structure [13].

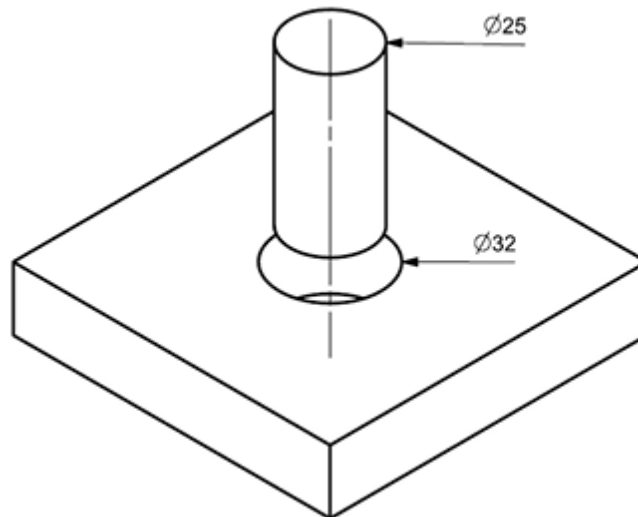


Figure 1.6: Isometric view of the perimeter shear test, units in [mm]. From [19].

The machine used to perform the tests is an Instron 5900 Series with a loading speed of 4 [mm/min] which corresponds to a quasi-static loading. The measured load and displacement will be exported in order to obtain force-displacement graphs. The peak force will correspond to the force value at failure, when the applicator will pass through the laminate. The test is considered successful when the value of this peak exceeds the minimum value specified by the regulations. This value differs for each area of the monocoque concerned by the test and is equal to 28 [kN] in the case of the FBH. As it can be observed on the Figure 1.7, as the load applicator will be pressed against the sample, the force will rapidly start to increase until reaching the first ply failure (FPF) where some fluctuations will appear. During this phase, damages will propagate in the sample until reaching the peak force that correspond to a puncture of the upper skin. After the sudden decrease in force, the load applicator will directly be in contact with the core and compress it, which corresponds to the plateau phase. Finally, the applicator will press the lower skin and the curve will evolve in the same way as the first one [20]. Due to the low toughness of carbon fiber and the contact between the load applicator and the sample, one can observe a brittle failure of the sample once the first ply failure has been reached, which makes this test the most difficult to pass for parts like the FBH.

Even though the sample size is relatively small, the large number of tests required for the lay-up design leads to significant material consumption and is very time-consuming. Although it is possible to easily model the three point bending test using finite elements thanks to ESAComp, the shear test, for its part, has never been modeled numerically due to its greater complexity. It was therefore decided to create a numerical model of the shear test in Ansys in order to accelerate the design process and reduce its costs while decreasing its environmental footprint. The implementation of these simulations would therefore establish a new composite testing strategy, where simulations could reduce the number of tests on sandwich-structured samples. The Chapter 4 will explain the modeling and calibration process of the test using finite elements. Based on the experimental results, it was concluded that the maximum force peaks are primarily due to the external skins rather than the core. It was therefore decided to model only one of the two external layers and without the core to avoid unnecessarily increasing the number of finite elements while simplifying the model. Thus, only the part of the sandwich structure that has a real impact on the shear test will be studied.

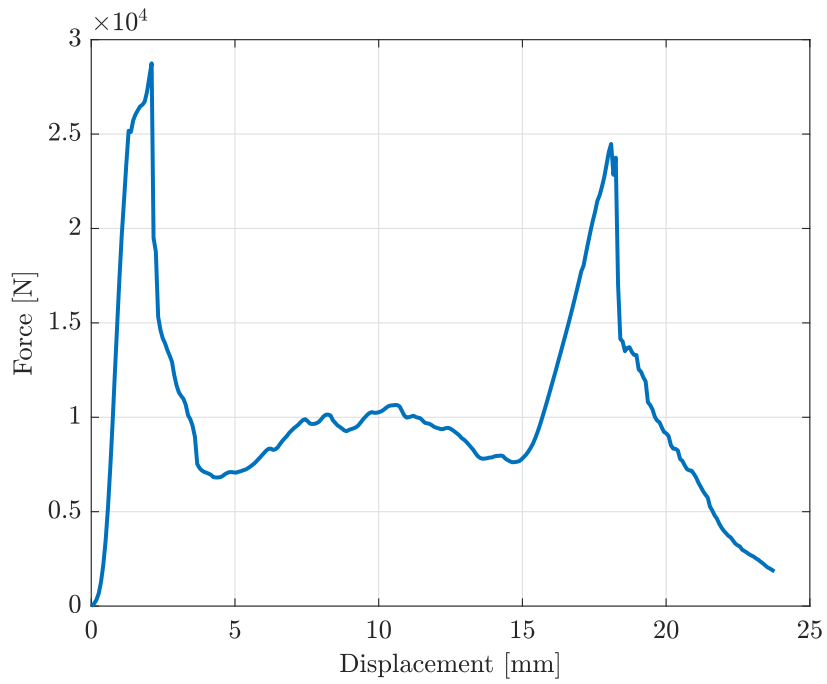


Figure 1.7: Results of the perimeter shear test on the FBH, showing the evolution of force with respect to displacement.

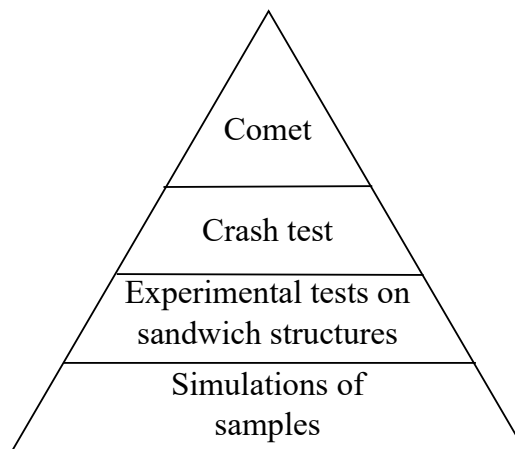


Figure 1.8: Test strategy for composite materials applied to the FBH.

CHAPTER 2

Materials study

This chapter aims to explore composite materials in their entirety. Initially, a review of the various types of fibers that can be used in composite manufacturing will be conducted to identify potential, more environmentally friendly alternatives to carbon fiber. The mechanics of composites will also be elaborated to understand the different failure criteria that can be applied. Finally, the properties of carbon-flax hybrid composites will be examined to determine the key factors influencing their design.

2.1 Material choice

The idea of replacing carbon fiber with more sustainable materials originated during the design of Apollo, last year's car. Based on the competition regulations, the aerodynamics department concluded that a composite using flax fiber could meet the requirements for the wings. Consequently, the rear wing and winglets were designed using flax fiber. Although innovative, this application of flax fiber serves as a reminder that this material is a serious alternative to synthetic fiber reinforced composites like carbon fiber or fiberglass. Indeed, from the manufacture of wind turbine blades to the design of satellite structures, flax fiber is used in various applications, including the automotive industry [8]. Since 2019, Porsche manufactures doors, lids, rear wing and many other parts of the 718 Cayman GT4 Clubsport MR with flax fiber. Although carbon fiber is the standard material for manufacturing such parts in motorsport, this innovative design choice enables Porsche to reduce cradle-to-gate CO₂ emissions of these components by up to 85%. Additionally, safety is enhanced as natural fiber parts do not splinter or produce sharp debris upon breaking, unlike carbon fiber parts, which pose a significant risk of punctures and injuries to marshals, drivers, and pit crews [17]. However, all these parts are non-structural parts, meaning that they do not have to support the weight of the vehicle and absorb the energy of the impact in case of crash. The first prototype of structural part was made by YCOM and Bcomp in 2020 when they developed the first front impact absorbing structure for motorsport. Crash tests demonstrate excellent results and the desired crash behavior, proving the concept and allowing to consider the utilization of natural fiber in motorsport for structural applications. However, it is important to note that while the safety requirements were satisfied and the CO₂ were decreased by 50 %, the final concept had a weight that was 40% higher compared to its carbon fiber counterpart [18]. This significant increase in weight might seem strange, given that the density of flax fiber is lower than that of carbon fiber. But, it can be explained by the fact that flax fiber has lower mechanical properties than carbon fiber [15, 21] and that it was experimentally observed by the team and researchers [22] that flax laminates tend to absorb much more resin than carbon during its manufacturing. These problems will be detailed in Chapter 3.



Figure 2.1: Front impact absorbing structure in flax fiber. From [18].

Innovation being one of the most important factors in the design of a Formula Student car, the incorporation of natural fibers into the chassis composition is of course part of the team's ambitions. Due to its functionality being close to that of the front impact absorbing structure developed by Bcomp and YCOM, it was then decided to initially investigate the use of more sustainable materials than carbon fiber for the design of the FBH. However, due to the addition of driverless functionalities, the weight of recent cars has significantly increased. An additional weight increase related to the chassis would therefore greatly affect the car's performance. Consequently, it was decided not to simply use flax fiber, but to find an alternative solution that would reduce the environmental impact of the chassis while maintaining an acceptable weight. To have a comprehensive understanding of the various materials that could be used, the first step of the study presented in this work was conducted using the material selection software Granta EduPack. Based on the requirements of monocoque design, three graphics were done to represent the specific stiffness, specific strength, and specific elongation at break of the materials with respect to their CO₂ footprint for primary production. It should be noted that only synthetic and natural fibers were considered, since it were the two most promising material families.

As it can be observed on the Figure 2.2, generally, synthetic fibers have a higher specific stiffness than natural fibers however their CO₂ footprint is in most case higher. The best result in terms of stiffness is obtained by the carbon fiber. Concerning the CO₂ footprint, basalt and banana fibers are the best, but it can be noticed that flax and ramie fibers provide an excellent balance between high specific stiffness and low CO₂ footprint. The Figure 2.3 shows synthetic fibers like zylon, aramid, basalt and glass S grade have a higher specific strength and a lower CO₂ footprint than carbon fiber. Although lower than that of the aforementioned fibers, the specific strength of kenaf fiber is the highest among natural fibers. Flax fiber is however more effective than ramie fiber. In general, natural fibers often have a lower specific strength than synthetic ones but remain advantageous in terms of CO₂ footprint. Finally, one can observe on the Figure 2.4 that in this case, natural fibers are often better than the synthetic ones, meaning higher performances in toughness. Polymeric fibers demonstrate superior specific elongation at break, while natural fibers like flax and ramie show results comparable to glass fiber. In each case, it can be observed that the mechanical properties of natural fibers are included in a wide range. Indeed, due to growing conditions and plant varieties, the reliability of the predictions of their mechanical performance is lower and the quality variability higher [21].

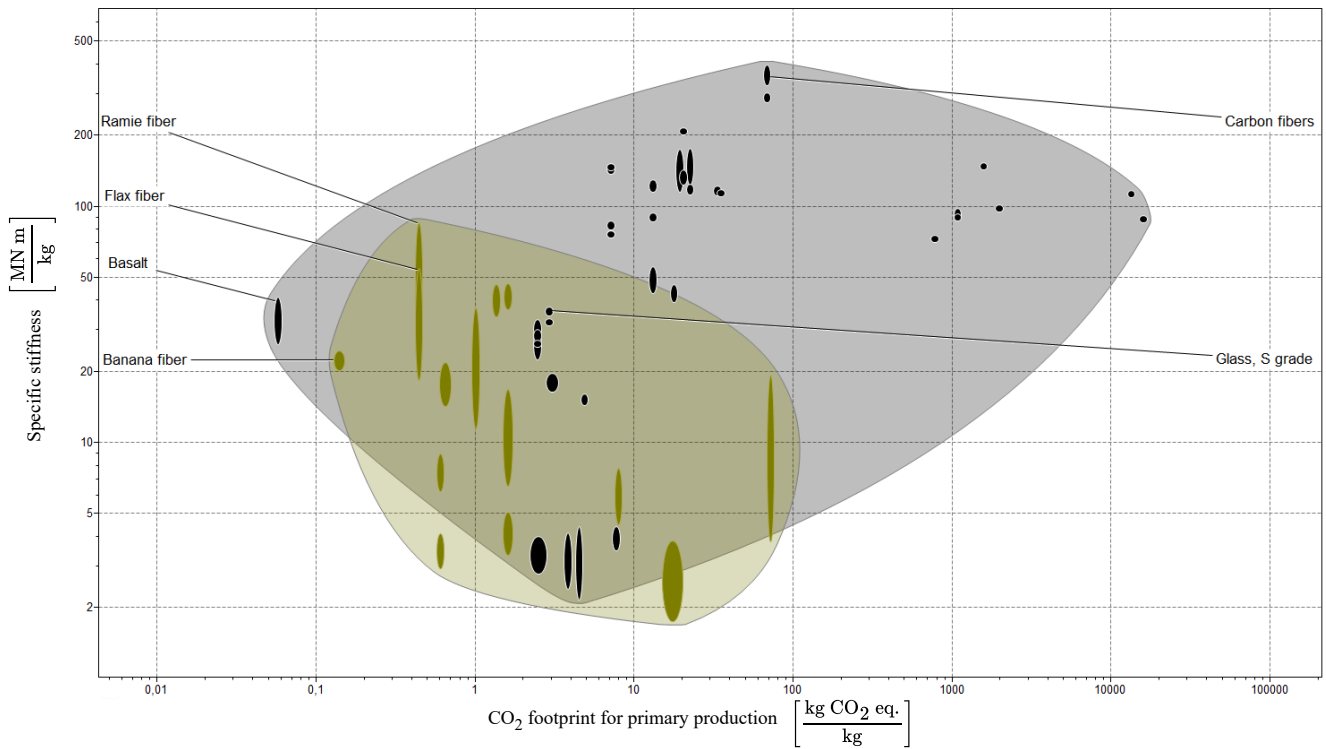


Figure 2.2: Material selection for fibers for maximizing the specific stiffness and minimizing the CO₂ footprint. Synthetic fibers are in black and natural fibers in beige.

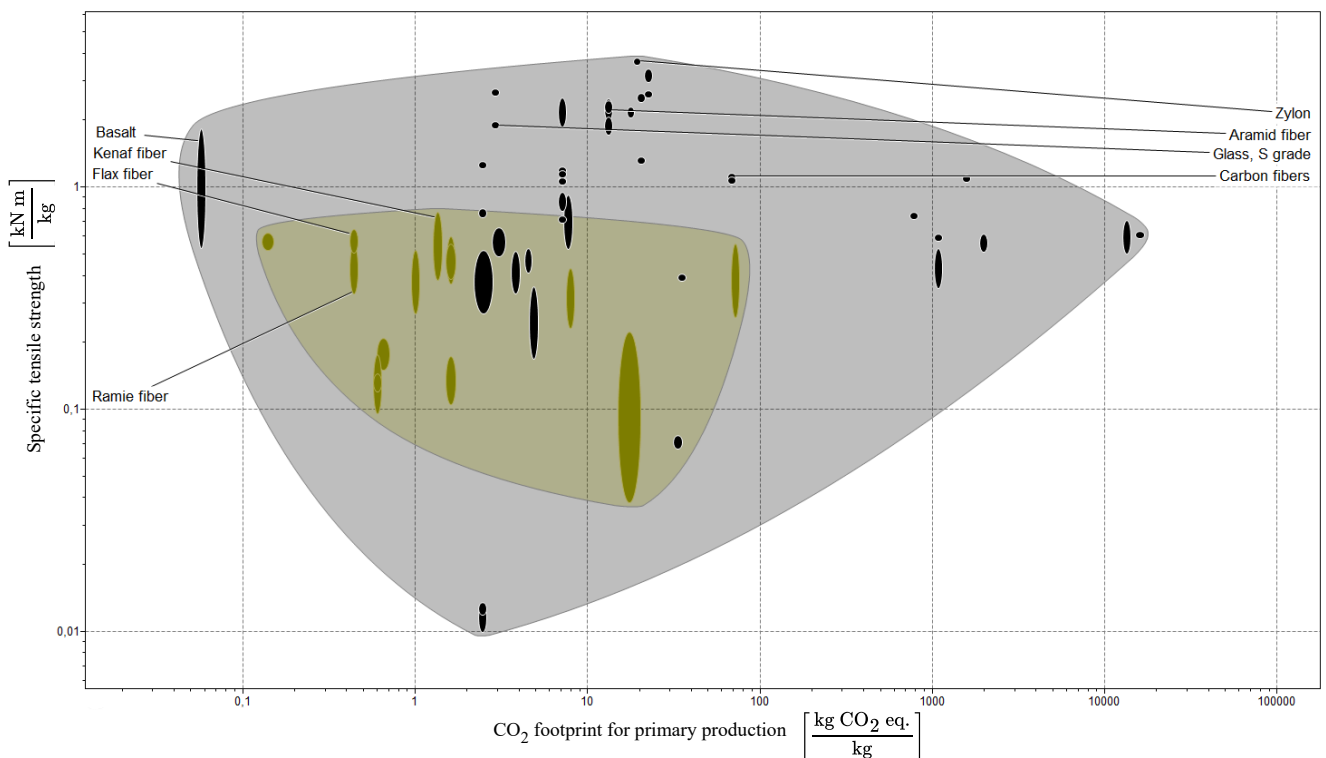


Figure 2.3: Material selection for fibers for maximizing the specific tensile strength and minimizing the CO₂ footprint. Synthetic fibers are in black and natural fibers in beige.

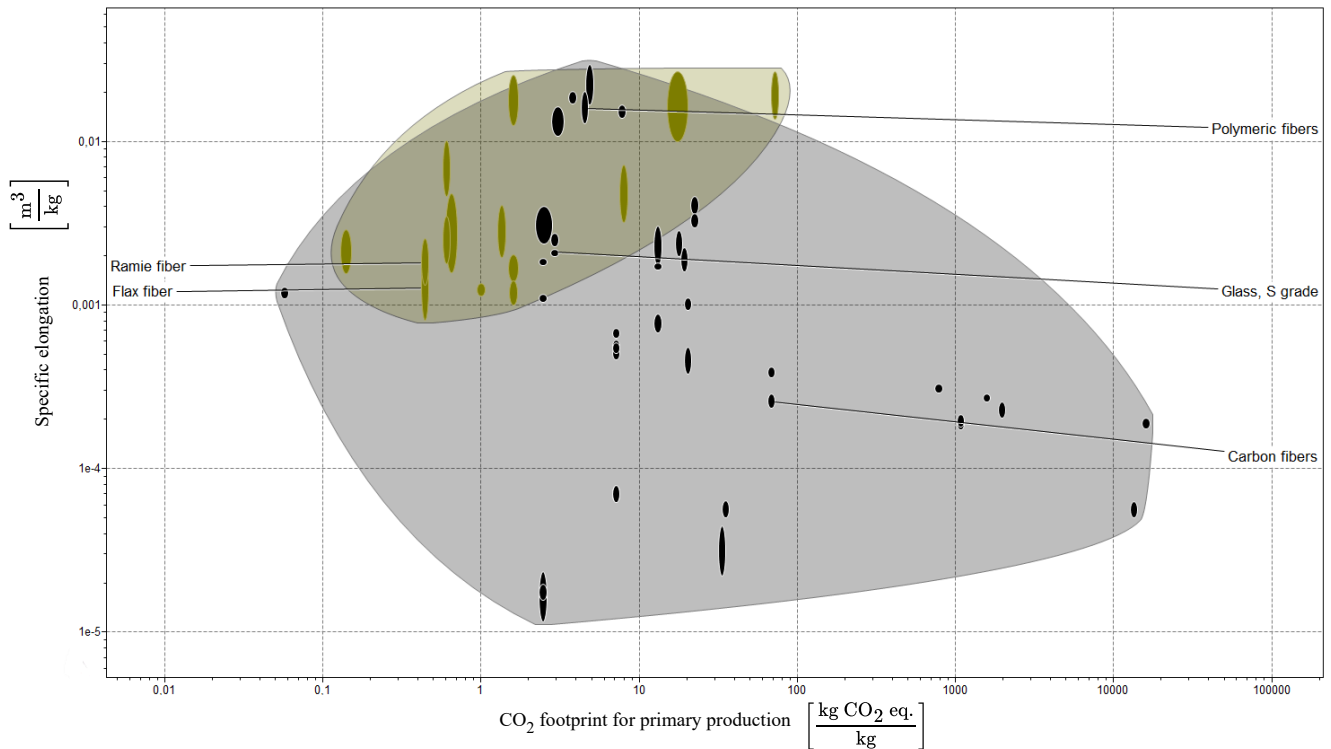


Figure 2.4: Material selection for fibers for maximizing the specific elongation and minimizing the CO₂ footprint. Synthetic fibers are in black and natural fibers in beige.

	Flax fiber	Ramie fiber	Glass fiber, S grade	Carbon fiber
Density [kg/m ³]	1470	1500	2500	1820
Young's Modulus [GPa]	27 - 80	44 - 128	86-93	370 - 390
Tensile strength [MPa]	750 - 940	500 - 820	4700 - 4800	2400 - 2410
Elongation [%]	1.2 - 3.2	2 - 3.8	5.2 - 5.3	0.7 - 1
Toughness [kJ/m ²]	0.0205 - 0.0903	1.12 - 5.23	0.003-0.0102	0.0028 - 0.0096

Table 2.1: Main mechanical properties of selected materials. The data are exported from Granta EduPack.

These graphs permit to understand the reason why carbon fiber is used in monocoque design and allows us to conclude that ramie fiber appears to be a more promising alternative to flax when compared to synthetic fibers. Indeed, ramie fiber has the highest specific stiffness among natural fibers, just ahead of flax, bringing it relatively closer to synthetic fibers like glass and carbon, which are typically the standard in the automotive industry [8]. Moreover, as it can be observed in the Table 2.1 which represents the most important properties of these fibers, ramie fiber has a better toughness than flax, which is a great advantage to design a high crashworthiness monocoque. However, the selection of this material presents two challenges:

1. **The ramie fiber has not yet reached sufficient industrial maturity:** According to RJP Modelage, a company specialized in the manufacturing of parts in natural fibers that was contacted, ramie fibers are currently too innovative for a utilization in the context of automotive applications. Moreover, no supplier of this type of fiber was found despite a long search.
2. **Ramie fiber's properties are insufficient to match the performance of carbon fiber:** While ramie fiber offers more advantageous mechanical properties compared to flax fiber, it is clear that it lacks the tensile strength and stiffness of carbon fiber. Consequently, constructing the FBH entirely from ramie fiber could result in the same weight issues encountered with the front impact absorbing structure developed by Bcomp and YCOM.

Therefore, it was decided to not utilize ramie fiber for the FBH lay-up, but instead to create a carbon-flax hybrid composite with enhanced mechanical performance. Recently, the use of this type of material has already been considered for the construction of cabin doors of ultralight helicopters. The goal was to reduce the environmental impact of the production of the helicopter structure by using flax fiber, allowing it to meet the aerospace requirements thanks to the hybridization [23]. As a general rule, hybridization of composites permits to combine the advantages of two different types of fibers [14]. In the case of designing the FBH, the goal is to address the brittle-like crash behavior under high strain loading of carbon fiber by enabling toughening through hybridization with flax. Simultaneously, carbon fiber would enhance the durability and mechanical properties of the composite. Theoretically, this approach would result in a component that is more eco-friendly, cost-effective, lighter, and exhibits gradual failure [14, 15]. This would ensure that the FBH remains functional even when overloaded [15]. The properties of this type of composite will be analyzed in detail in Section 2.4.

2.2 Structure and composition of composites

This section focuses on the micro and macroscopic analysis of the structure and composition of composite materials, with a particular emphasis on two types of fibers: carbon fiber and flax fiber. Due to its natural origin, flax has a different microscopic structure from carbon fiber, which gives it specific properties. Indeed, for the carbon fiber, the structure is composed of planes of carbon atoms. All these planes are stacked together thanks to van der Waals forces. Considering the fact that these bonds are weaker than covalent bonds, the carbon fiber is therefore an anisotropic material. However, this kind of structure permit it to have a quasi-linear elastic tensile behavior [21]. Flax is for its part collected from the stem of flax plant. The fiber itself is composed of cellulose, hemicellulose and lignin, thereby enabling it to have good physico-mechanical properties. Although cellulose is the strongest and stiff organic material, performances of natural composites are sometimes negatively impacted by the fact that properties of flax fibers are influenced by several factors, including geographical location, climate, weathering conditions, soil quality, plant species and variety, cultivation practices, and the maturity level of the plants. The sensitivity of flax fibers to moisture is the other major drawback, which does not block it from being the dominant natural fiber in the composite industry [8]. Finally, flax fibers show a non-linear elastic behavior under tensile loading [21].

Despite their differences in their microscopic structure, these two fibers can be industrially used in a similar manner to manufacture composites. Indeed, the manufacturing of composite parts can therefore be done using epoxy resin as matrix and trough process like hand lay-up, compression molding, vacuum infusion or using prepreg. Just like carbon, it is possible to find flax fiber under the following ply forms:

- **Unidirectional:** In this configuration, all the fibers are in the same direction. The fact that the fibers are not interwoven like in a woven fabric allows for optimal utilization of the fiber's properties, maximizing strength and stiffness. UD plies also achieve higher properties since they generally have a higher volume fraction of fiber [24].



Figure 2.5: Unidirectional ply. From [25].

- **Woven fabric:** Woven fibers consist of two sets of fibers interlaced at right angles. Woven fibers generally have lower strength and stiffness in any single direction compared to UD plies. However, they provide more balanced properties across multiple directions, offering better performance in complex loading conditions. Woven permit to obtain better impact resistance, damage, tolerance, and toughness than UD [26]. The two most common woven patterns are plain and twill 2x2 weaves [24].

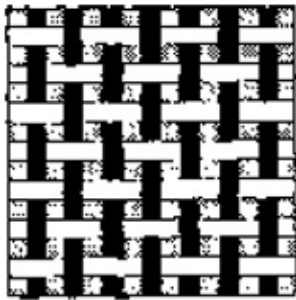


Figure 2.6: Plain weave ply. From [25].

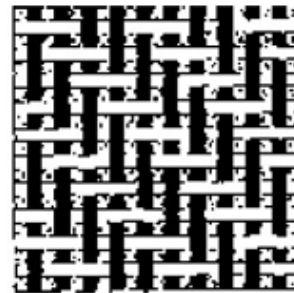


Figure 2.7: Twill 2x2 ply. From [25].

In structural applications, woven fabrics can be combined with unidirectional tapes to create mixed composites. These composites provide enhanced overall properties with woven fabrics boosting impact resistance, while UD tapes contribute to higher in-plane stiffness and strength [26]. Orientation of the fibers and the stack-up sequence of the plies are therefore the most important parameters to take into account when designing a lay-up. However, since it is the fibers that primarily bear the load, providing the composite its strength and stiffness, while the matrix transfers the load to the fibers, protects them from damages, and ensures their alignment and stability [5]. Knowing the volume fraction and the quality of the fibers can vary following the selected product, the choice of fiber type and its quality are therefore significant factors.

2.3 Mechanics of composite

The analysis and prediction of composite material properties are fundamental aspects of composite engineering. Although nowadays, these predictions are often determined by finite element simulations and experimental tests, it remains important to understand the theory describing the mechanics of composites called classical lamination theory and explained in [25]. All laminates and plies stiffness equations are expressed in a matrix form that can be used in software to construct a numerical model of the composite.

2.3.1 Classical lamination theory

Due to their nature, composite laminates possess properties that depend on the constituents that composed each ply. Based on micromechanics, it is possible to accurately estimate the main properties of unidirectional plies by using a key formula called law of mixture:

$$E_x = E_M V_M + E_F V_F = E_M(1 - V_F) + E_F V_F \quad (2.1)$$

$$E_y = E_M \left(\frac{1}{(1 - V_F) + \frac{E_M}{E_F} V_F} \right) \quad (2.2)$$

with E_x the elastic modulus of the composite in the longitudinal direction, E_y the elastic modulus of the composite in the transverse direction, E_M the elastic modulus of the matrix, E_F the elastic modulus of the fibers, V_M the volume fraction of the matrix and V_F the volume fraction of the fibers. This rule is based on the assumption that fibers and matrix have the same longitudinal deformation, and can also be extended to the Poisson ratio.

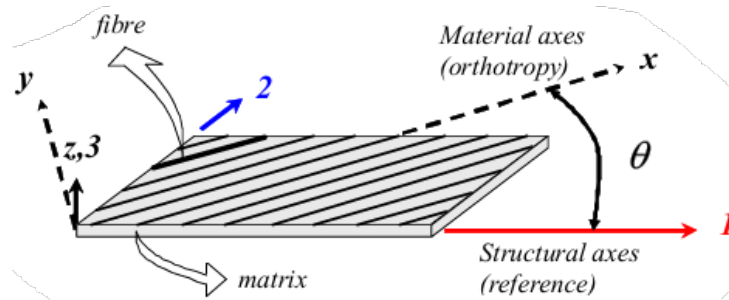


Figure 2.8: Unidirectional ply with its axis systems. From [25].

Considering the orthotropy of the material, stresses $\{\sigma_x \sigma_y \sigma_{xy}\}$, and strains $\{\epsilon_x \epsilon_y \gamma_{xy}\}$ of each ply can be computed in the orthotropy axes (x, y, z), which are related to the fiber direction thanks to the following equations:

$$\begin{Bmatrix} \sigma_x \\ \sigma_y \\ \sigma_{xy} \end{Bmatrix} = \begin{bmatrix} mE_x & mv_{yx}E_x & 0 \\ mv_{xy}E_y & mE_y & 0 \\ 0 & 0 & G_{xy} \end{bmatrix} \begin{Bmatrix} \epsilon_x \\ \epsilon_y \\ \gamma_{xy} \end{Bmatrix} = \begin{bmatrix} Q_{xx} & Q_{xy} & 0 \\ Q_{yx} & Q_{yy} & 0 \\ 0 & 0 & Q_{ss} \end{bmatrix} \begin{Bmatrix} \epsilon_x \\ \epsilon_y \\ \gamma_{xy} \end{Bmatrix} \quad (2.3)$$

with

$$m = \frac{1}{1 - \nu_{xy}\nu_{yx}} \quad \frac{\nu_x}{\nu_y} = \frac{E_x}{E_y} \quad Q_{xy} = Q_{yx} \quad (2.4)$$

and denoting G_{xy} the in-plane shear modulus, $Q_{ij}(\theta_k)$ the stiffness coefficients that depend on θ_k the angle between the orthotropy axes and the structural axis, ν_{xy} and ν_{yx} the longitudinal Poisson's coefficients. Note that this theory is also valid for woven by considering that E_x is equal to E_y . By doing a transformation of coordinates, stresses $\{\sigma_1 \ \sigma_2 \ \sigma_6\}$, and strains $\{\varepsilon_1 \ \varepsilon_2 \ \varepsilon_6\}$ of each ply can be retrieved in the structural axis (1, 2, 3) employing the following equations:

$$\begin{Bmatrix} \sigma_1 \\ \sigma_2 \\ \sigma_6 \end{Bmatrix} = \begin{bmatrix} Q_{11} & Q_{12} & Q_{16} \\ Q_{12} & Q_{22} & Q_{26} \\ Q_{16} & Q_{26} & Q_{66} \end{bmatrix} \begin{Bmatrix} \varepsilon_1 \\ \varepsilon_2 \\ \varepsilon_6 \end{Bmatrix} \quad (2.5)$$

$$\mathbf{Q}_{(1,2,3)} = \begin{Bmatrix} Q_{11} \\ Q_{22} \\ Q_{12} \\ Q_{66} \\ Q_{16} \\ Q_{26} \end{Bmatrix}_{(1,2,3)} = \begin{bmatrix} c^4 & s^4 & 2c^2s^2 & 4c^2s^2 \\ s^4 & c^4 & 2c^2s^2 & 4c^2s^2 \\ c^2s^2 & c^2s^2 & c^4 + s^4 & -4c^2s^2 \\ c^2s^2 & c^2s^2 & -2c^2s^2 & (c^2 - s^2)^2 \\ c^3s & -cs^3 & cs^3 - c^3s & 2(cs^3 - c^3s) \\ cs^3 & -c^3s & (c^3s - cs^3) & 2(c^3s - cs^3) \end{bmatrix} \begin{Bmatrix} Q_{xx} \\ Q_{yy} \\ Q_{xy} \\ Q_{ss} \end{Bmatrix}_{(x,y,z)} \quad (2.6)$$

where $c = \cos(\theta_k)$ and $s = \sin(\theta_k)$. With the properties of each ply now determined, an analytical model of the entire laminate can be established thanks to the classical lamination theory. Using the kinematics laws for a Kirchhoff plate, the total strain of the laminate can be expressed as:

$$\boldsymbol{\varepsilon} = \boldsymbol{\varepsilon}^0 + z\boldsymbol{\kappa} \quad (2.7)$$

by denoting $\boldsymbol{\varepsilon}$ the resulting strain, the curvature $\boldsymbol{\kappa}$ related to out-of-plane strains and $\boldsymbol{\varepsilon}^0$ the membrane strains due to in-plane deformation. However, this approach requires several assumptions:

- The plate must be initially flat and with a constant thickness.
- The ratio of the thickness to width should be inferior to 0.2.
- The ratio of the transversal displacement to thickness should be inferior to 0.2.
- A segment initially normal to the mid-plane remains straight and normal to the mid-plane in the deformed state.
- The stresses in the normal direction are negligible.
- Thermomechanical terms are neglected.

Even if stresses vary linearly in each ply of the laminate, their evolutions are discontinuous at the ply boundaries and so across the laminate. Stress resultant are defined to represent the applied loads by multiplying the applied stress or stress couple by the thickness:

$$\begin{Bmatrix} N_1 \\ N_2 \\ N_6 \end{Bmatrix} = \int_{-h/2}^{h/2} \begin{Bmatrix} \sigma_1 \\ \sigma_2 \\ \sigma_6 \end{Bmatrix} dz \quad (2.8)$$

$$\begin{Bmatrix} M_1 \\ M_2 \\ M_6 \end{Bmatrix} = \int_{-h/2}^{h/2} \begin{Bmatrix} \sigma_1 \\ \sigma_2 \\ \sigma_6 \end{Bmatrix} z dz \quad (2.9)$$

with h the height of the plate, $\{N_1 \ N_2 \ N_6\}$ the in-plane resultants and $\{M_1 \ M_2 \ M_6\}$ the bending resultants. Starting from the equation 2.7, the behavior of the laminate in structural axes can be modeled using:

$$\begin{Bmatrix} \mathbf{N} \\ \mathbf{M} \end{Bmatrix} = \begin{bmatrix} \mathbf{A} & \mathbf{B} \\ \mathbf{B} & \mathbf{D} \end{bmatrix} \begin{Bmatrix} \boldsymbol{\epsilon}^0 \\ \boldsymbol{\kappa} \end{Bmatrix} \quad (2.10)$$

$$\Leftrightarrow \begin{Bmatrix} N_1 \\ N_2 \\ N_6 \\ M_1 \\ M_2 \\ M_6 \end{Bmatrix} = \begin{bmatrix} A_{11} & A_{12} & A_{16} & B_{11} & B_{12} & B_{16} \\ A_{12} & A_{22} & A_{26} & B_{12} & B_{22} & B_{26} \\ A_{16} & A_{26} & A_{66} & B_{16} & B_{26} & B_{66} \\ B_{11} & B_{12} & B_{16} & D_{11} & D_{12} & D_{16} \\ B_{12} & B_{22} & B_{26} & D_{12} & D_{22} & D_{26} \\ B_{16} & B_{26} & B_{66} & D_{16} & D_{26} & D_{66} \end{bmatrix} \begin{Bmatrix} \epsilon_1^0 \\ \epsilon_2^0 \\ \epsilon_6^0 \\ \kappa_1 \\ \kappa_2 \\ \kappa_6 \end{Bmatrix} \quad (2.11)$$

Components of the matrices \mathbf{A} , \mathbf{B} and \mathbf{D} can be retrieved with the following equations:

$$A_{ij} = \sum_{k=1}^n [Q_{ij}(\theta_k)] t_k \quad (2.12)$$

$$B_{ij} = \sum_{k=1}^n [Q_{ij}(\theta_k)] t_k z_k \quad (2.13)$$

$$D_{ij} = \sum_{k=1}^n [Q_{ij}(\theta_k)] \left(t_k z_k^2 + \frac{t_k^3}{12} \right) \quad (2.14)$$

As it can be seen in Figure 2.9, t_k is the thickness of the ply k and z_k its vertical position. \mathbf{B} is called the membrane-bending coupling matrix and demonstrate that a laminate can warp under a purely in-plane load. Pure bending moments can also induce a stretching of the laminate. Fortunately, the design of symmetric lay-up permits to avoid this kind of undesirable coupling effect. By doing that, every ply located on one side of the laminate midplane, there exists a corresponding ply on the opposite side of the midplane, situated at an equivalent distance, composed of the same material, with identical thickness and orientation. It permits therefore to obtain a matrix \mathbf{B} where all elements are equal to 0.

Similarly, the non-zero A_{16} and A_{26} terms of \mathbf{A} lead to a coupling between extensional stresses and shear strains. Moreover, bending and twisting are coupled due to non-zero D_{16} and D_{26} terms of \mathbf{D} . Using a balanced homogenous lay-up where there are a ply at $-\theta$ for each ply at θ or if all plies are oriented at 0° and 90° then A_{16} and A_{26} are equal to 0 [25, 27]. Note that laminates with a symmetric lay-up of orthogonally balanced woven fabrics will not exhibit the coupling effects between shear or extension.

Based on these conclusions and standard practices, the following design rules can be summarized:

- **Add fabric ply to inner and outer layers:** Fabric ply like plain weave permits a better impact damage absorption, which is useful in the case of a sample required to pass the shear test.

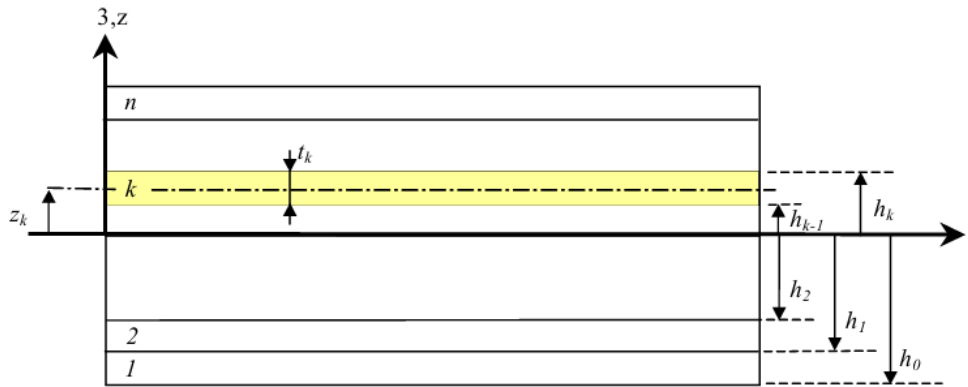


Figure 2.9: Stacking of plies. From [25].

- **Add $+45^\circ$ and -45° plies with at least one pair on laminate extremes:** By orienting plies at $\pm 45^\circ$, the damage tolerance of the laminate is increased as well as the buckling.
- **Design a laminate with at least one ply in each of the directions 0° , 90° and $\pm 45^\circ$:** Layers oriented at 0° permit to maximize the resistance to longitudinal loads while those at 90° maximize the resistance to transverse load. The layers oriented at $\pm 45^\circ$ must be added in pairs and must be in contact with each other to minimize the interlaminar shear. These layers permit maximize the resistance to shear load in traction and in compression as illustrated in Figure 2.10.

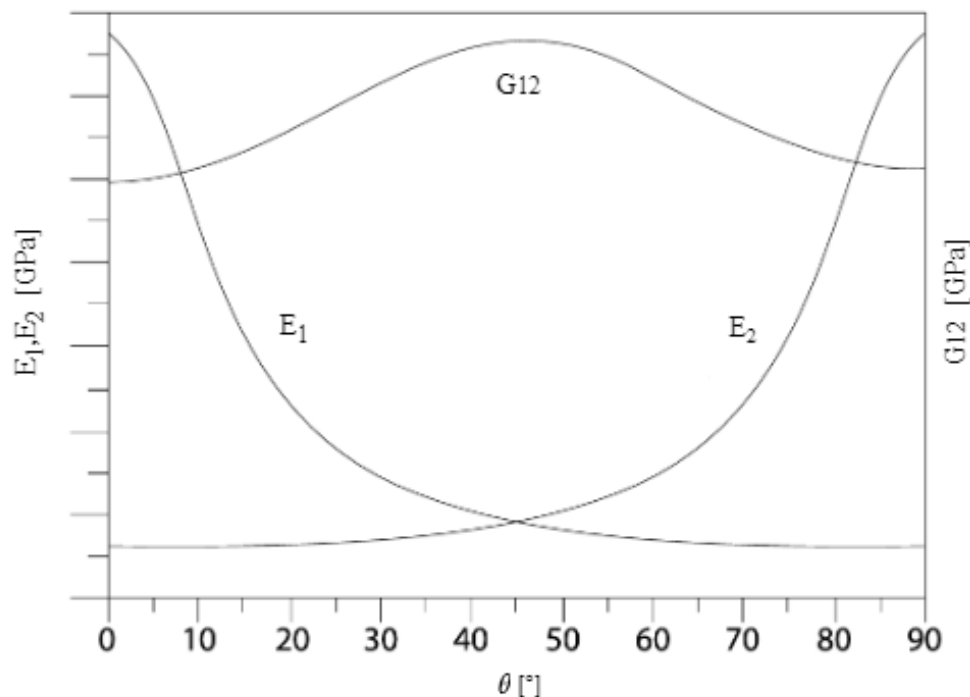


Figure 2.10: Ply modulus as a function of the ply angle. Adapted from [27].

These rules will be taken into consideration during the design of the various lay-ups that follow in this work.

2.3.2 Failure criteria and damage mechanisms

The failure of composite materials is a more complex phenomenon than that which occurs in conventional isotropic materials. In reality, the mechanisms leading to the failure of composites are not yet fully understood, contributing to the difficulty in developing effective models to predict damage and the material's response when subjected to excessive loads [28]. According to [29], two primary processes permit to absorb energy during a loading. The first process involves material deformation, while the second involves the creation of new surfaces, such as cracks. The failure of composite materials can be categorized according to various damage mechanisms, which depend on the type and location of the load applied to the laminate. These primary mechanisms are:

- **Delamination:** It is the separation of the various layers stacked at different orientation that compose the composite material due to high stress concentration in the interface. Delamination cracks absorb a large quantity of energy when they propagate. Delamination frequently occurs in specimens subjected to bending, due to the predominant out-of-plane shear stresses [29, 30].
- **Fiber failure:** This mechanism occurs when the laminate is subjected to excessively high compression or tension along the fiber direction. It becomes critical when there are not enough fibers remaining to support the load, after many individual fibers in the ply have failed. This mechanism releases large amounts of energy, leading to catastrophic failure [29, 30, 31].
- **Matrix breaking:** Due to cracks and voids located between fibers of a single ply, this damage mode can take place when the laminate is subjected to important loads in tension in a direction perpendicular to fibers [32].
- **Fiber-matrix debonding:** For unidirectional tapes, debonding can occur depending on the manufacturing process. This mechanism is complex to analyze [32].
- **Fiber buckling:** If compression occurs in the direction of the fiber, fiber buckling can occur, promoting other types of damages like matrix debonding. Therefore, this structural phenomenon not lead directly to the failure of the composite, but it is still undesirable [32].

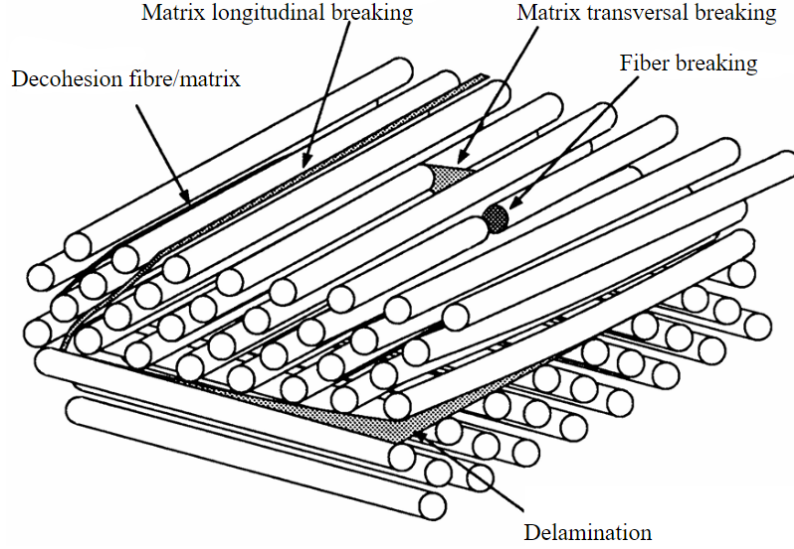


Figure 2.11: Failure modes in composites. Adapted from [25].

Although these failure mechanisms exhibit different physical behaviors, they do not occur randomly and require the material to reach a failure point. That is, until certain critical conditions are met, the integrity of the composite will be maintained. These conditions are defined by failure criteria, which take into account various factors such as maximum stress, ultimate strain, and specific loading modes. However, it is important to remind that it is not because one ply fails that the entire laminate fails. These criteria permit to identify the first ply failure that is the first step of the failure. The most commonly used failure criteria for composites include the maximum stress criterion, the maximum strain criterion, and more advanced criteria such as Tsai-Hill and Tsai-Wu.

Maximum stress theory This criterion is relatively simple, since it only verifies that the stress is within the ranges defined by the different strengths of the material. It is expressed as:

$$\text{Failure of fibers} \begin{cases} X_c < \sigma_x < X_t \\ Y_c < \sigma_y < Y_t \end{cases} \quad (2.15)$$

$$\text{Failure of matrix} \begin{cases} Z_c < \sigma_z < Z_t \\ -S < \sigma_S < S \\ -R < \sigma_R < R \\ -Q < \sigma_Q < Q \end{cases} \quad (2.16)$$

where X_t, Y_t, Z_t are the ply tensile strengths, X_c, Y_c, Z_c are the ply compressive strengths and S, R, Q the ply shear strengths. This criterion has the disadvantage of not representing the coupling between the stress and, in addition, not being very accurate [25, 26, 31].

Maximum strain theory This theory is similar to that of the maximum stress, since in this case, the strain is defined from the stress limitations :

$$\text{Failure of fibers} \begin{cases} X_{\epsilon c} < \epsilon_x < X_{\epsilon t} \\ Y_{\epsilon c} < \epsilon_y < Y_{\epsilon t} \end{cases} \quad (2.17)$$

$$\text{Failure of matrix} \begin{cases} Z_{\epsilon c} < \epsilon_z < Z_{\epsilon t} \\ -S_{\epsilon} < \epsilon_S < S_{\epsilon} \\ -R_{\epsilon} < \epsilon_R < R_{\epsilon} \\ -Q_{\epsilon} < \epsilon_Q < Q_{\epsilon} \end{cases} \quad (2.18)$$

where $X_{\epsilon c}$, $X_{\epsilon t}$, $Y_{\epsilon c}$, $Y_{\epsilon t}$, $Z_{\epsilon c}$, $Z_{\epsilon t}$, S_{ϵ} , R_{ϵ} and Q_{ϵ} are the allowable strains derived from the strengths and elastic modulus of the ply. Although there is coupling in this criterion, similar to the maximum stress theory, it is not actually considered very reliable [25].

Tsai-Hill failure criterion Tsai-Hill is an extension of Von Mises to the anisotropic case. It has the advantage of accounting for the interactions between stresses in different directions, thus incorporating coupling. The Tsai-Hill criterion equation must be below 1 to avoid a failure and is expressed as:

$$\begin{aligned} & \frac{\sigma_x^2}{X^2} + \frac{\sigma_y^2}{Y^2} + \frac{\sigma_z^2}{Z^2} + \frac{\sigma_Q^2}{Q^2} + \frac{\sigma_R^2}{R^2} + \frac{\sigma_S^2}{S^2} - \sigma_x \sigma_y \left(\frac{1}{X^2} + \frac{1}{Y^2} - \frac{1}{Z^2} \right) \\ & - \sigma_x \sigma_z \left(\frac{1}{X^2} - \frac{1}{Y^2} + \frac{1}{Z^2} \right) - \sigma_y \sigma_z \left(-\frac{1}{X^2} + \frac{1}{Y^2} + \frac{1}{Z^2} \right) < 1 \end{aligned} \quad (2.19)$$

with

$$X = \begin{cases} X_T & \text{if } \sigma_x \geq 0 \\ X_C & \text{if } \sigma_x < 0 \end{cases} \quad Y = \begin{cases} Y_T & \text{if } \sigma_y \geq 0 \\ Y_C & \text{if } \sigma_y < 0 \end{cases} \quad Z = \begin{cases} Z_T & \text{if } \sigma_z \geq 0 \\ Z_C & \text{if } \sigma_z < 0 \end{cases} \quad (2.20)$$

It is therefore possible to use this criterion in traction and in compression. However, it does not permit to model effectively materials that have different strengths in tension and compression. Moreover, it also does not allow for determining whether the failure is due to fiber breaking or matrix cracking. This criterion is ultimately more reliable than the previous ones and shows good agreement with tests, but it is still not optimal [25, 31].

Tsai-Wu failure criterion This last criterion aims to address the main flaw of the Tsai-Hill criterion by considering the different behavior a material can exhibit under tensile and compressive loading. This criterion also takes into account interactions between the stresses and assumes that failure will not occur as long as the Tsai-Wu function is less than 1. It can thus be expressed in the following form:

$$\begin{aligned} & F_1 \sigma_x + F_2 \sigma_y + F_3 \sigma_z + F_{11} \sigma_x^2 + F_{22} \sigma_y^2 + F_{33} \sigma_z^2 + F_{44} \sigma_Q^2 \\ & + F_{55} \sigma_R^2 + F_{66} \sigma_S^2 + 2F_{12} \sigma_x \sigma_y + 2F_{13} \sigma_x \sigma_z + 2F_{23} \sigma_y \sigma_z < 1 \end{aligned} \quad (2.21)$$

considering

$$\begin{aligned} F_1 &= \left(\frac{1}{X_T} + \frac{1}{X_C} \right) & F_2 &= \left(\frac{1}{Y_T} + \frac{1}{Y_C} \right) & F_3 &= \left(\frac{1}{Z_T} + \frac{1}{Z_C} \right) \\ F_{11} &= -\frac{1}{X_T X_C} & F_{22} &= -\frac{1}{Y_T Y_C} & F_{33} &= -\frac{1}{Z_T Z_C} \\ F_{44} &= \frac{1}{Q^2} & F_{55} &= \frac{1}{R^2} & F_{66} &= \frac{1}{S^2} \end{aligned} \quad (2.22)$$

As for Tsai-Hill, this criterion does not permit to determine if the failure is due to fiber breaking or matrix cracking. However, it remains more reliable than the Tsai-Hill criterion and yields results

that closely match experimental tests. Other criteria, such as Hashin, also allow for the prediction of delamination in the material, providing a better representation of potential damage that may occur [25, 31, 32].

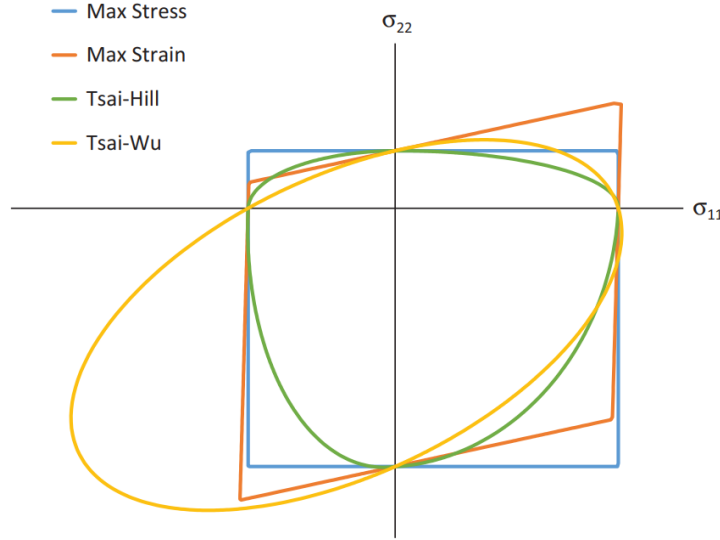


Figure 2.12: Comparison of the different failure envelopes defined by the failure criteria. From [31].

Each criterion helps predicting the composite's behavior under different loading conditions and contributes to a better understanding and anticipation of potential failure points. Therefore, the rigorous application of these criteria is essential to ensure the reliability and safety of composite structures in demanding service environments. However, it is not optimal to base the design of a lay-up on the FPF, since it will lead to a too conservative design. It is therefore necessary to have a better understanding of the progressive failure of the laminate through damages modeling.

2.3.3 Material damages modeling

To set up a predictive simulation tool, the definition of reliable material models able to represent the degradation of the ply is crucial. Most advanced models include delamination but in the context of this work, only intra-laminar damages modeling will be used in Ansys. This kind of model is based on continuum damage mechanics that defines damage variable affecting the ply's stiffness are associated with different failure modes, representing fiber breaking, matrix cracking, and debonding between fibers and matrix. To calibrate the numerical simulation based on that, many numerical parameters must be identified from experimental test at the sample level [33]. Due to small defects from the manufacturing process, test results exhibit some variability, even when conducted on sample from the same plate. Thus, it is essential to account for such dispersions in material properties and their influence on the composite's mechanical response. From the principle of the continuum damage mechanics, these parameters can be defined as [34]:

$$d_f = \begin{cases} d_{ft} & \text{if the fiber is in tension} \\ d_{fc} & \text{if the fiber is in compression} \end{cases} \quad (2.23)$$

$$d_m = \begin{cases} d_{mt} & \text{if the matrix is in tension} \\ d_{mc} & \text{if the matrix is in compression} \end{cases} \quad (2.24)$$

$$d_s = 1 - (1 - d_{ft})(1 - d_{fc})(1 - d_{mt})(1 - d_{mc}) \quad (2.25)$$

with d_f the damage variable for fiber, d_m the variable for matrix and d_s the variable for shear damages. Their values vary between 0 and 1 which means that when it is zero, the material is intact, and when it is 1, the material has completely lost its stiffness. The fiber damage variables for damage modes in tension and compression are d_{ft} and d_{fc} while d_{mt} and d_{mc} are the matrix damage variables for damage mode in tension and compression. These parameters are obtained from the strain energy and permit to define the damaged elasticity matrix:

$$\mathbf{D}_d = \begin{bmatrix} \frac{C_{11}}{(1-d_f)} & C_{12} & C_{13} & 0 & 0 & 0 \\ C_{21} & \frac{C_{22}}{(1-d_m)} & C_{23} & 0 & 0 & 0 \\ C_{31} & C_{32} & \frac{C_{33}}{(1-d_m)} & 0 & 0 & 0 \\ 0 & 0 & 0 & \frac{C_{44}}{(1-d_s)} & 0 & 0 \\ 0 & 0 & 0 & 0 & \frac{C_{55}}{(1-d_s)} & 0 \\ 0 & 0 & 0 & 0 & 0 & \frac{C_{66}}{(1-d_s)} \end{bmatrix}^{-1} \quad (2.26)$$

where \mathbf{C} is the compliance matrix of the undamaged material. In this way, the constitutive relationship for a damaged composite is given by:

$$\boldsymbol{\sigma} = \mathbf{D}_d \boldsymbol{\epsilon} \quad (2.27)$$

This type of model is natively implemented in Ansys, allowing for finite element numerical simulations that account for material failure and resulting damage. Two damage evolution methods are available. The first one is the material property degradation method where the stiffness of the material is directly reduced from the damage variables d_{ft} , d_{fc} , d_{mt} and d_{mc} defined in the properties of the material. The continuum damage mechanics method is as more advanced model where the variables increase gradually as a function of the energy amounts dissipated by the various damage modes. It requires the definition of damping coefficients and energy dissipation parameters that are much more complex to determine when creating a material model from scratch [34].

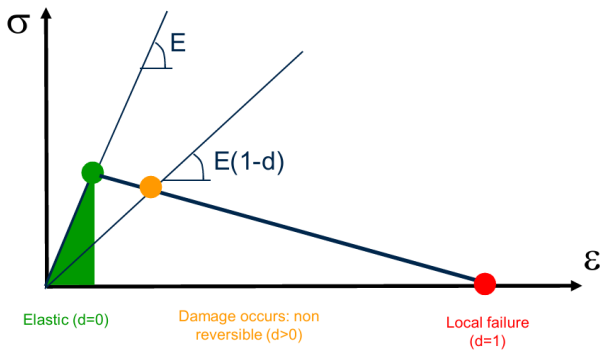


Figure 2.13: Representation of the effects of damage on a ply. From [25].

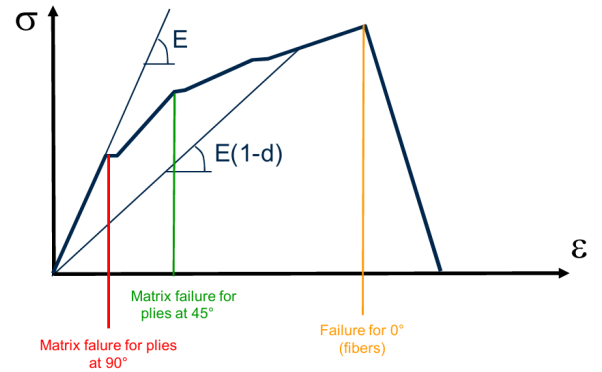


Figure 2.14: Representation of the effects of damage on a laminate. From [25].

2.4 Analysis of carbon-flax hybrid composites

This section aims to identify the key mechanical properties of carbon-flax hybrid composites through a review of relevant articles. By utilizing standardized tests, these properties will enable a better

understanding of the behavior of hybrid materials, providing initial insights for designing an optimized lay-up to maximize performance in a perimeter shear test. The latter is specifically designed for validating composites within the scrutineering process of Formula Student competitions. As a result, there are currently no articles or research available that document the properties of hybrid fiber-reinforced polymers (HFRP) when subjected to the perimeter shear test. However, due to its similarity to low-velocity impact tests, relevant insights can be drawn from these tests in order to determine the parameters that increase indentation resistance and applied them to the shear test. In general, the effectiveness of a composite in achieving positive hybrid effects depends on the hybridization mode and the volume ratio of the different fibers. These parameters will be examined in the following articles and throughout the remainder of this work.

2.4.1 Tensile properties

In 2023, Anni Wang et al. [15] studied the effect of carbon fiber volume fraction, carbon fiber monolayer thickness and hybrid mode on hybrid composites subjected to tensile test. HFRP samples were prepared by wet winding with unidirectional fibers, and it was observed that for sandwich hybrid mode Flax-Carbon-Flax noted $[F/C/F]$ increasing the carbon fiber volume fraction leads to an increase of the tensile modulus and of the tensile strength. In this way, a volume fraction of 60.94% permits to obtain a modulus 219.26% higher and a strength 241.09% higher compared with that of flax fiber-reinforced polymers (FFRP). When the carbon fiber volume fraction was 5.8%, 9.42% and 31.88%, the tensile failure strain of the sample was respectively 32.01%, 27.65% and 13.52% higher than that of the CFRP. However, when the fraction was 60.94%, hybridization led to a negative hybrid effect. Concerning the effects of the hybrid mode, results showed that the tensile modulus was not influenced by it, but it had impact on the strength. Indeed, samples with flax fiber as external layers and carbon as core led to positive hybrid effects. Moreover, minimizing the interfaces permit to have less crack by interface delamination and delayed the failure. Positive effect on the failure strain was observed with an alternated stack-up sequence $[F/C/F/F/C/F]$. Finally, an optimized sample was made with a carbon fiber volume fraction of 26.4%. Its strength was 129.3% higher than a FFRP and its toughness was increased by 32% compared with that of the CFRP. Therefore, by reducing the thickness of the carbon fiber layers and alternating their sequence with flax layers, the flax fibers are dispersed in the lay-up and help to distribute the stress concentration caused by carbon fiber fractures, resulting in optimal performance.

A study on the effects of hybridization and hybrid fiber dispersion on the mechanical properties of woven flax-carbon epoxy at low carbon fiber volume was made by Umeyr Kureemun et al. [35] enabled the observation that the primary mode of failure in hybrid composites is a brittle failure of carbon plies due to their lower failure strain. Cracks are initiated and led to a sequential failure of the flax fibers at the interfaces.

2.4.2 Bending properties

Jeff Flynn et al. [21] designed hybridized carbon-flax composites for tailored performances in 2016. The stack up sequence was in each case $[C_1/F_x/C_y/F_x/C_1]$ but they studied the influence of the volume fraction of carbon and flax fibers by varying the amount of layers x and y in the inner layers. Indeed, all the additional carbon fiber plies were added in the center of the sequence since the addition of carbon fibers in the external layers would lead to increase of the flexural strength and interchange with the influence of the fiber volume fraction. Results showed that an increase of the flax fiber

volume content led to a decrease of the flexural modulus and of the ultimate flexural strength. This result can also be explained by the fact that, due to the variation in fiber volume fractions, the authors consequently made significant changes to the total number of layers in the samples. However, it was noticed that a configuration with only five plies stacked alternately $[C_1/F_1/C_1/F_1/C_1]$ and a flax fiber volume fraction of 19% had the highest flexural modulus and a flexural strength close to that of samples with eight times more carbon plies, showing that the fiber stacking sequence plays a large role in flexural property performance.

Another study made by H.N Dhakal et al. [36] confirms that although their lower flexural strength, carbon-flax hybrid laminates permit to obtain better toughness properties by showing higher elongation compared to CFRP. To optimize bending properties, unidirectional plies also seemed to be the best choice.

2.4.3 Impact properties

In 2023, Anni Wang et al. [14] made another research on the effects of volume ratio and hybrid mode on low-velocity impact properties of unidirectional carbon-flax hybrid composites. Previous study had already showed that HFRP permit to obtain superior impact resistance than CFRP, the study therefore focused on the factors that can maximize this resistance. Concerning the effect of the volume ratio, it was observed that the higher the carbon fiber content, the lower is the local impact loading threshold since CFRPs are highly brittle during an impact loading. Consequently, a high carbon fiber content led to a lower deformation at the maximum impact force reaction force. Thanks to the higher deformability of flax fibers, it is therefore possible to increase the elastic energy absorption by reducing the carbon fiber content. However, the energy absorption capacity depends on the thickness of the sample. The specific energy absorption *SEA* was therefore defined as:

$$SEA = \frac{E_a}{m_s} \quad (2.28)$$

with E_a the energy absorption and m_s the mass or thickness of the sample. It was observed that an increase of the carbon fiber content led to an increase of the *SEA*. The study of the effects of hybrid mode on impact properties initially allowed to conclude that the $[C/F/C]$ configuration permit to reach a higher peak force than the $[F/C/F]$ due to the higher strength of carbon fibers. For 15 [J] impact tests, $[C/F/C]$ hybrid mode permits to have a greater *SEA* than that of the $[F/C/F]$ while for 5 [J] impact tests, it is the contrary. It is explained by the fact that for the low energy impact, the damage is confined to the surface layer while for the higher energy impact, the carbon fiber layers become brittle and these are the flax layers that deform and absorb energy. The subsequent failure mechanism is the following: Firstly, the matrix cracks on the top layer due to high shear stress. Then, there is a transverse bending cracking of the bottom layer followed by a delamination. Finally, the fibers break under the tension stress and a slight buckling and it leads to the penetration of the sample.

Finally, a last study conducted by Anni Wang et al. [37] on carbon-flax hybrid composites made with woven fabrics concluded that a $[C/F/F/F/C]$ configuration is able to reach a higher *SEA* than a $[F/C/F/C/F]$ configuration for a 25 [J] impact energy test. These results are shown in Figure 2.15. This latter also demonstrated a *SEA* nearly equal to that of a configuration consisting of 5 layers of carbon. The difference in results between the two hybrid modes was explained by the greater number of interfaces in the alternated hybrid configuration, leading to higher shear stress and thereby facilitating delamination.

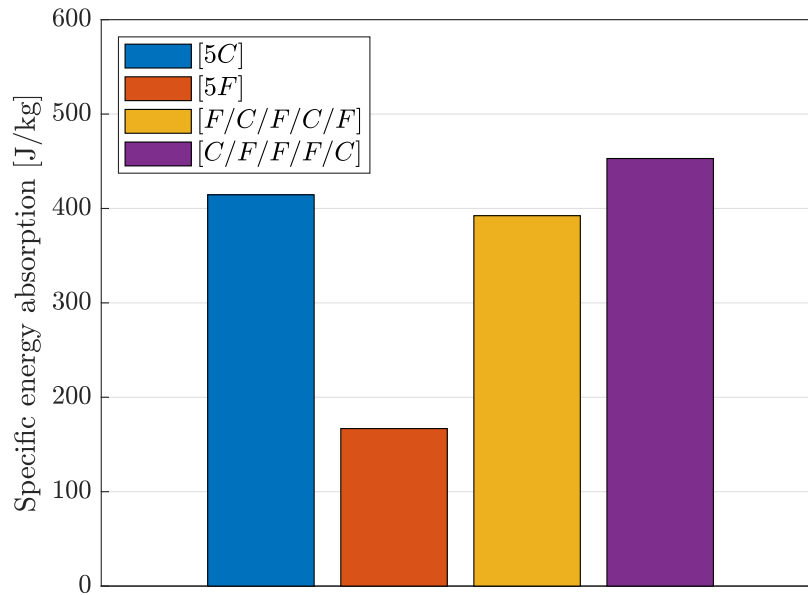


Figure 2.15: Specific energy absorption energy for an impact test of 25 [J]. Adapted from [37].

2.5 Conclusion

The previously mentioned properties suggest that the use of a carbon-flax hybrid fiber reinforced polymer is a serious option to consider for the design of the FBH. As expected, the tensile and flexural properties of hybrid materials are slightly lower compared to carbon fiber. However, due to its superior impact resistance, its suitability for use in a monocoque structure is further reinforced. It is clear that the response of a hybrid material to a shear test will differ from that of a low-velocity impact test. However, the insights gained can serve as a valuable starting point for designing the hybrid samples that will be examined in the next chapter.

Considering the design rules explained in this chapter, it was decided that only woven fabric plies will be used in the subsequent study on hybrid laminates to simplify the analysis. Although this decision might seem arbitrary, it is based on the superior impact resistance, damage tolerance, and toughness of woven fabrics.

CHAPTER 3

Design and analysis of hybrid composites

In this chapter, carbon-flax hybrid composites will be examined from several experimental perspectives. To achieve reliable values, each sample discussed in this work has been produced in triplicate. Since the front bulkhead is part of the monocoque, the study must focus on solutions that are compatible with the chassis manufacturing process. Ideally, the hybrid composites should be made from compatible prepregs. However, it was not possible to obtain flax fiber prepregs from our supplier, as they are still a relatively rare product. Consequently, dry fibers will be used and infused with epoxy resin. It is important to note that all samples mentioned in this thesis were manufactured by the author with the assistance of members of Formula Electric Belgium.

3.1 Manufacturing process

The samples for the shear test have a simple and compact geometry, which does not pose any manufacturing challenges. However, due to the large number of different configurations that can be tested, many samples must be produced for each testing campaign. It is therefore essential to use manufacturing procedures that allow for the production of a maximum number of samples while ensuring optimal quality. Two kinds of fibers can be used:

- **Pre-impregnated fibers:** As the name suggests, this type of fiber is supplied as a semi-finished product with the resin already impregnated into the fibers. The major advantage of these fibers is that the amount of resin is perfectly controlled, ensuring consistent quality and better mechanical properties. Moreover, this helps prevent the formation of air bubbles during manufacturing while greatly simplifying the process. However, this type of material has an expiration date and comes with a high cost.
- **Dry fibers:** These fibers need to be manually impregnated during the manufacturing process. Consequently, the infusion process requires strict control to avoid defects such as resin pockets, air bubbles, or poorly impregnated areas. As a result, manufacturing composite parts using this type of fiber is much more time-consuming and can lead to samples with mechanical properties inferior to those made with prepreg.

Depending on the type of material chosen, the manufacturing process will be determined to ensure that the samples achieve optimal quality.

3.1.1 Prepreg compression molding

The first manufacturing process used was a variation of prepreg compression molding. The goal here is to take advantage of the fact that the samples are rectangular and completely flat, allowing two aluminium plates to serve as a mold to apply pressure to the fibers during curing. The manufacturing process is the following:

1. After cleaning the aluminium plates, a release agent is applied to facilitate the demolding. Three layers of this polytetrafluoroethylene-based product are required.
2. The prepreg fibers are laid on the first plate according to the desired lay-up configuration.
3. The second plate is applied to the samples, and clamps are used to compress the plate against the samples. The samples are spaced at regular intervals to ensure the most uniform pressure possible.
4. The plates are placed in an industrial oven and heated to the required curing temperature. Once the curing cycle is complete, the plates are gradually cooled while maintaining pressure. The controlled cooling prevents thermal stresses and ensures the dimensional stability of the part [25].

Although this method eliminates the need for a vacuum bag, making it simpler, it does not seem optimal for sample fabrication. Indeed, due to uneven pressure and temperature distribution, a significant number of voids can be observed within these laminates. One of the produced samples even appears not to be properly cured, as it exhibits numerous imperfections that are shown in Figure 3.1. Therefore, another method will be adopted for the fabrication of the experimental samples.

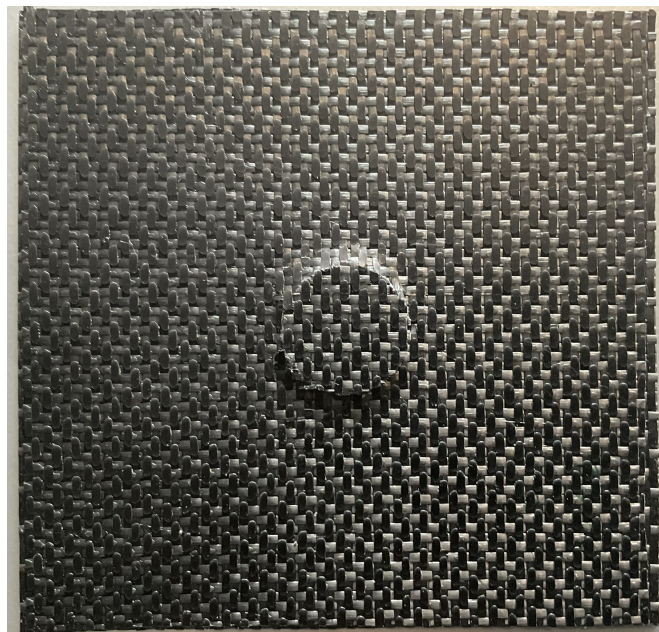


Figure 3.1: Sample that was not fully cured.

3.1.2 Prepreg autoclave curing

Similar to prepreg compression molding, this process involves using an aluminum plate where the fibers are laid out after a release agent has been applied. However, in this case, the samples are covered with a release film and a breather. The breather allows better air circulation during curing, while the release film facilitates separation of the samples during demolding. Next, the plate is placed under vacuum with the aid of a vacuum bag, which isolates the samples from the outside. This setup enables the application of uniform vacuum pressure during the autoclave cycle. The autoclave is an oven that applies both heat and pressure according to the material-specific cure cycle. This ensures optimal curing, resulting in composites with high mechanical performance. Additionally, this process is relatively fast. Depending on the number of layers to be cut, it is possible for the samples to be manufactured from start to finish in 2 days. This process is therefore the most optimal for prepreg fibers.

3.1.3 Vacuum-assisted resin infusion

This manufacturing process was used for the hybrid samples. Since Formula Electric Belgium had no prior experience with this process, inspiration was drawn from the methods used for manufacturing flax fiber winglets. Two types of flax fibers were used: the first with an areal weight of 150 [g] per square meter, and the second with an areal weight of 350 [g] per square meter. The process is as follows:

1. After cleaning an aluminium plate, a release agent is applied, like for the prepreg compression molding process.
2. The fibers are laid on the plate according to the desired lay-up configuration. Since it is dry fibers, an adhesive spray is used to fix the different layers.
3. Samples are covered with a peel ply and a mesh grid in order to facilitate the flow and absorption of the resin. The entire setup is sealed from the outside by an airtight vacuum bag. The setup is illustrated in Figures 3.2 and 3.3.
4. Tubes are placed along two opposite sides of the plate to allow the epoxy resin to infiltrate the setup. The epoxy resin and hardener are carefully mixed in a mass ratio of 70:30 and then placed in a vacuum chamber to remove air bubbles. One end of the flow tube is immersed in the resin, while the other end is connected to the vacuum pump. Once the vacuum pump is turned on, the resin is drawn into the fiber cloth. After the resin has fully infiltrated the fibers, seal both ends of the diversion tubes with clamps and turn off the vacuum pump.
5. After maintaining the setup under vacuum for 24 hours to allow the curing process to take place, the samples are then placed in an oven at 120 [°C] for 2 hours for post-curing.

Although this process offers significantly better quality than a hand lay-up, it does not provide the same control over the epoxy mass fraction as with prepreg materials. As a result, the quality is certainly acceptable, but nevertheless lower compared to the prepreg method. Additionally, vacuum-assisted resin infusion is much more time-consuming. Indeed, producing our samples using this method required a minimum of four days for each batch.

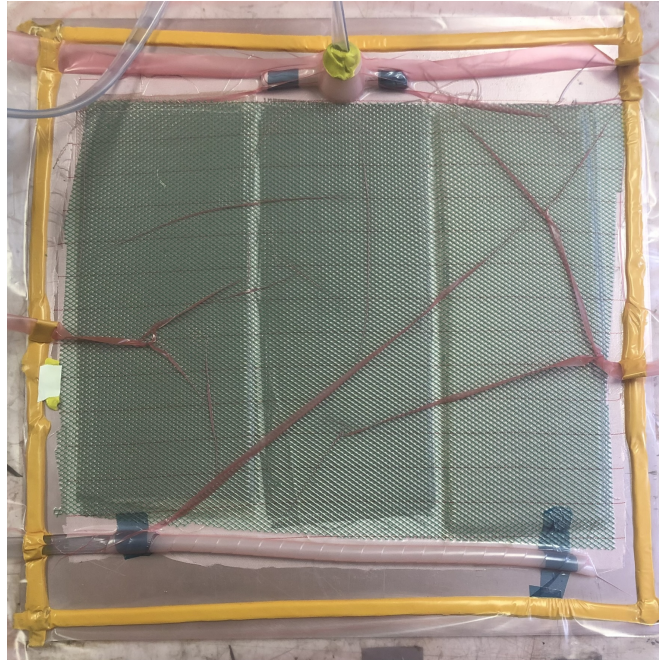


Figure 3.2: Vacuum-assisted resin infusion setup.

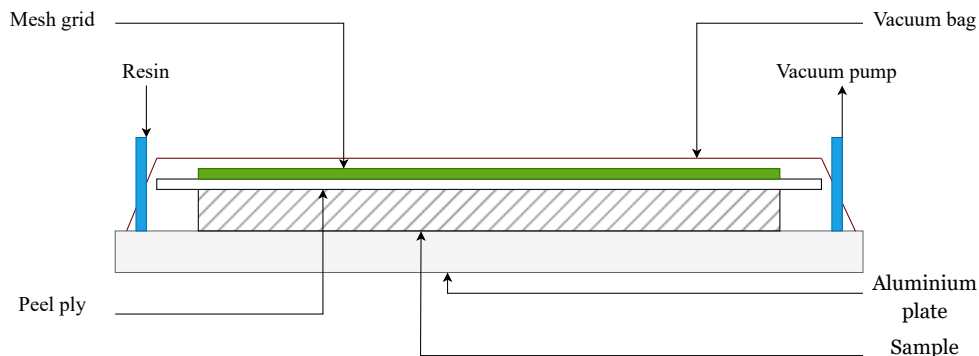


Figure 3.3: Illustration of the vacuum-assisted resin infusion setup.

3.2 Analysis of hybridization

In the previous chapter, the stack-up sequence and the volume ratio have been identified as the most influential parameters on the impact resistance properties as well as on the tensile and bending properties. However, since there are no studies regarding hybrid composites subjected to shear tests, it is important to verify whether the conclusions observed in these standardized tests can also apply to the perimeter shear test. Therefore, inspired by the stack-up sequences developed in [14, 15, 35, 37], samples 1 and 2 were designed to be tested and studied. The purpose of these samples is to determine whether it is preferable to have a hybrid mode where the flax fibers are placed in the outer layers, or if it is better to have the carbon fibers on the outer layers, or whether an alternating stack-up sequence yields the best results. Samples 1 have a higher content in flax fiber while for the

samples 2, it is the contrary. They were all produced using vacuum-assisted resin infusion. Their characteristics are presented in Tables 3.1 and 3.2, while their stack-up sequences can be visualized in Figure 3.4. Except for samples 6, all the samples studied in this chapter have a lay-up where all layers are oriented at 0 [°]. It should also be noted that all the data presented are derived from or based on experimental measurements.

	Stack-up sequence	Thickness [mm]
Samples 1a	[F/F/C/C/F/F]	2.85
Samples 1b	[F/C/F/F/C/F]	2.86
Samples 1c	[C/F/F/F/F/C]	2.78
Samples 2a	[F/C/C/C/C/F]	2.01
Samples 2b	[C/F/C/C/F/C]	2.03
Samples 2c	[C/C/F/F/C/C]	2.05

Table 3.1: Stack-up sequence and thickness of the samples 1 and 2 produced.

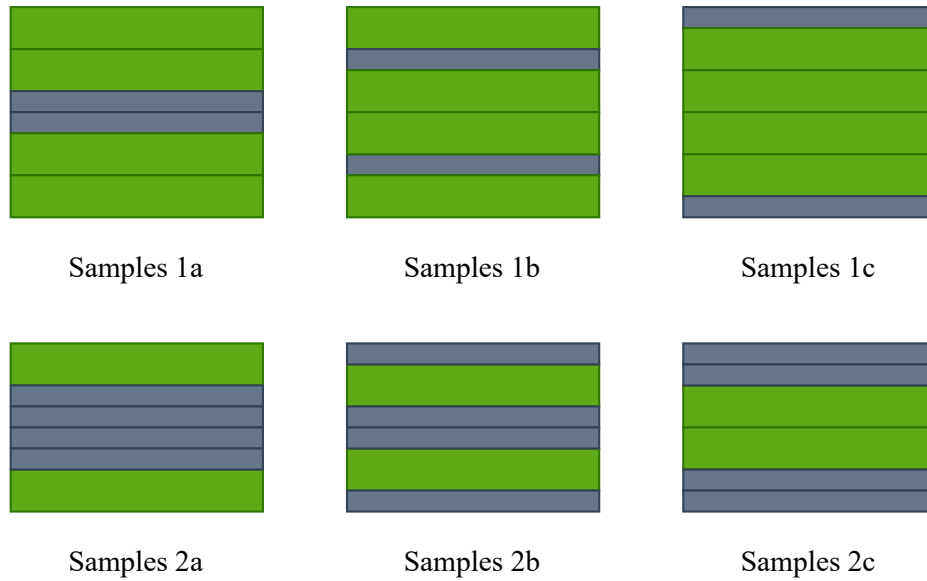


Figure 3.4: Illustration of the stack-up sequences of samples 1 and 2.

Samples	1a	1b	1c	2a	2b	2c
Areal weight (dry) [kg/m²]	1.89	1.89	1.89	1.68	1.68	1.68
Areal weight (cured) [kg/m²]	3.22	3.25	3.20	2.49	2.58	2.46
Weight of the sample [g]	32.21	32.59	32.08	24.93	25.87	24.65
Flax fiber mass fraction (dry) [%]	74.07	74.07	74.07	41.66	41.66	41.66
Epoxy mass fraction [%]	41.33	42.01	41.09	32.75	35.07	31.86

Table 3.2: Mass properties of the samples 1 and 2 produced.

These tables allow for some initial observations. Indeed, although the areal weight of the dry flax fiber is higher than that of carbon fiber, the samples 1 have an areal weight that is much bigger than the weight of the samples 2. This difference is explained by the difference in terms of epoxy mass fraction. Samples designed with 74% mass fraction of dry flax fiber have a percentage higher than 41% in epoxy mass fraction while for samples 2, this percentage is between 31.86 and 35.07%. This effect can also be observed in Table 3.1, where the samples 1 are almost 1 [mm] thicker than the samples 2. Moreover, it can be noticed that when carbon fibers are in the outer layers, the epoxy mass fraction seems to be higher. Therefore, it appears that the greater the amount of flax fiber in a hybrid composite, the higher the epoxy mass fraction will be, and consequently, the total weight as well.

Samples 3 and 4 are intended to compare the raw performance of flax fiber and carbon fiber samples subjected to the perimeter shear test. However, they also allow for observation of the resin absorption phenomenon and provide a basis for confirming the formulated hypotheses. As it can be seen in Tables 3.3 and 3.4, samples 3 are 2.7 times thicker than samples 4a for the same number of layers. Moreover, the latter are 2.26 times lighter than the samples 3. Even with twice as many layers and therefore a higher mass of dry fibers, after infusion and curing, samples 3 are 15% heavier than samples 4b. This major disadvantage for flax fiber is related to its high resin absorption during the composite manufacturing process. Consequently, the epoxy mass fraction in this case rises to 48.02%, which is quite significant. This issue has also been identified in other studies [22, 23], leading to lower mechanical performance than theoretically expected, as well as an increase in the composite's overall weight. It is therefore crucial for the development of carbon-flax hybrid composites to achieve better control over epoxy resin absorption. The ideal solution would be to develop and use flax fibers in a pre-impregnated form, with a fiber volume content comparable to that of carbon fibers. Since these materials are not yet available for our study, optimizing performance remains heavily dependent on the ratio of carbon fiber to flax fiber in the composite. The ideal hybrid composite will be one that maximizes the toughness benefits of flax fiber without significantly increasing the overall weight. Based on this observation and the test results of samples 1 and 2, samples 5 were designed to test different optimized stack-up sequences, bringing them closer to a configuration that could be used for the FBH. Their characteristics are shown in Table 3.5 and 3.6 while the stack-up sequences are illustrated in Figure 3.5. It can also be observed that when flax fibers are placed in the outer layers, the epoxy mass fraction increases.

	Stack-up sequence	Thickness [mm]
Samples 3	[4F]	2.3
Samples 4a	[4C]	0.85
Samples 4b	[8C]	1.58

Table 3.3: Stack-up sequence and thickness of the samples 3 and 4 produced.

Samples	3	4a	4b
Areal weight (dry) [kg/m²]	1.4	0.98	1.96
Areal weight (cured) [kg/m²]	2.69	1.19	2.26
Weight of the sample [g]	26.93	11.91	22.67
Flax fiber mass fraction (dry) [%]	100	0	0
Epoxy mass fraction [%]	48.02	17.73	13.54

Table 3.4: Mass properties of the samples 3 and 4 produced.

	Stack-up sequence	Thickness [mm]
Samples 5a	[C/C/F/F/C/C/F/F/C/C]	3.55
Samples 5b	[F/C/C/F/C/C/F/C/C/F]	3.62
Samples 5c	[C/C/F/C/F/F/C/F/C/C]	3.56
Samples 5d	[C/C/C/F/F/F/F/C/C/C]	3.55
Samples 5e	[F/F/C/C/C/C/C/C/F/F]	3.58

Table 3.5: Stack-up sequence and thickness of the samples 5 produced.

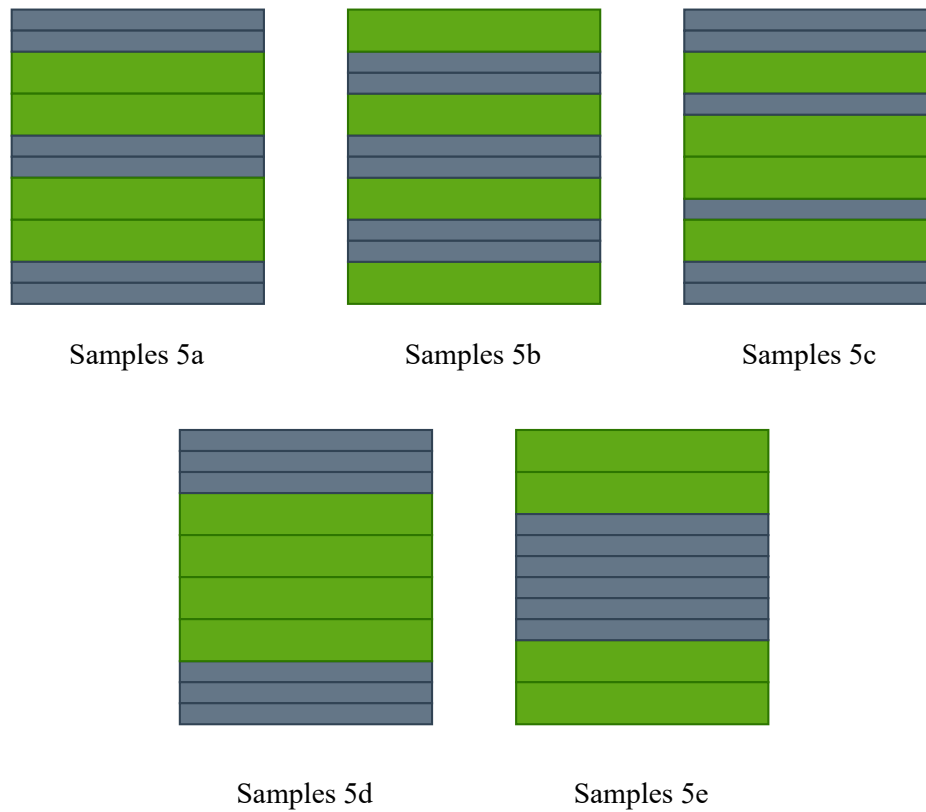


Figure 3.5: Illustration of the stack-up sequences of samples 5.

Samples	5a	5b	5c	5d	5e
Areal weight (dry) [kg/m²]	2.87	2.87	2.87	2.87	2.87
Areal weight (cured) [kg/m²]	4.31	4.41	4.39	4.36	4.48
Weight of the sample [g]	43.15	44.16	43.95	43.61	44.84
Flax fiber mass fraction (dry) [%]	48.78	48.78	48.78	48.78	48.78
Epoxy mass fraction [%]	33.49	35.02	34.71	35.99	37.91

Table 3.6: Mass properties of the samples 5 produced.

These last samples are designed to study the influence of 45 [°] flax fiber plies in a composite lay-up subjected to the perimeter shear test. Consequently, the two outer layers of samples 6b are oriented at 45 [°], while those of sample 6a are kept at 0 [°]. Additionally, these outer layers use the Flax 150g to study the effect of a lower fiber weight on the results of the perimeter shear test. Tables 3.7 and 3.8 indicate the properties of the fabricated samples. Now that all the different samples have been defined, and their manufacturing characteristics established, one can proceed to subject them to shear testing to study the impact of these characteristics on the results. Note that all the

curves presented hereafter have been normalized with respect to their displacement. During the experimental testing procedure, the displacement of the load applicator is manually reset to zero just before it comes into contact with the sample being tested. This results in a relative displacement measurement by the machine, allowing the displacement curves to be calibrated so they all start at the same point, enabling rigorous comparison.

	Stack-up sequence	Thickness [mm]
Samples 6a	[4F]	1.87
Samples 6b	[4F]	1.86

Table 3.7: Stack-up sequence and thickness of the samples 6 produced.

Samples	6a	6b
Areal weight (dry) [kg/m²]	1	1
Areal weight (cured) [kg/m²]	2.17	2.09
Weight of the sample [g]	21.74	20.94
Flax fiber mass fraction (dry) [%]	100	100
Epoxy mass fraction [%]	54.01	52.25

Table 3.8: Mass properties of the samples 6 produced.

3.2.1 Influence of fibers orientation and of material selection.

This section aims to study the influence of the materials themselves on a sample subjected to the perimeter shear test. Figure 3.6 shows that the samples 3 permit to reach a higher peak force than samples 4a, composed entirely of carbon fibers, whose results are illustrated in Figure 3.7. This graph confirms the visual observations made during the experiments. Indeed, shortly after the flax fiber sample begins loading, stress whitening can be observed around the area in contact with the load applicator. Deformation is primarily localized in this region, and despite these effects, the force continues to increase until the complete failure of the composite, which occurs when the cylinder begins to perforate the sample. For sample 4a, the observed phenomena differ. Firstly, deformation is less localized, and the sample begin to buckle relatively quickly. No damage is visible up to the peak force. Beyond this point, the force increases more slowly, and cracking sounds can be heard. Failure occurs shortly afterward, leading to a sharp decrease in force. It appears that the failure mechanism is similar to the one described in Section 2.4.3 for the penetration of an impact hammer into a composite. Although the flax fiber appears to perform slightly better, it's important to note that sample 3 is significantly heavier than sample 4a, which is a major drawback when considering the use of a lay-up composed solely of flax fiber for the monocoque. This is why using flax fiber in hybrid composites with an optimized stack-up sequence appears more promising.

Concerning the effect of the orientation of the flax fiber layers, it can be noticed in Figures 3.8 and 3.9 that the samples 6b with 45[°] plies at laminate extremes are able to reach a higher peak force than the samples 6a. Therefore, it is possible now to confirm that, just as with carbon fiber,

orienting flax plies at 45° in the outer layers increases the damage tolerance of the laminate. It is important to note that the peak forces obtained are lower than those of Sample 3, indicating that a reduction in the fiber weight leads to a decrease in performance.

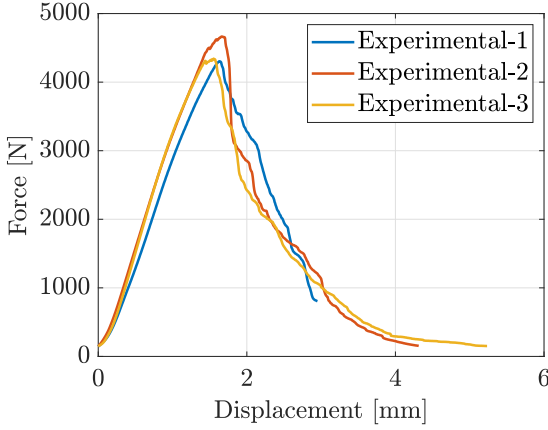


Figure 3.6: Force-displacement curves of experimental data for samples 3. The displacements are normalized.

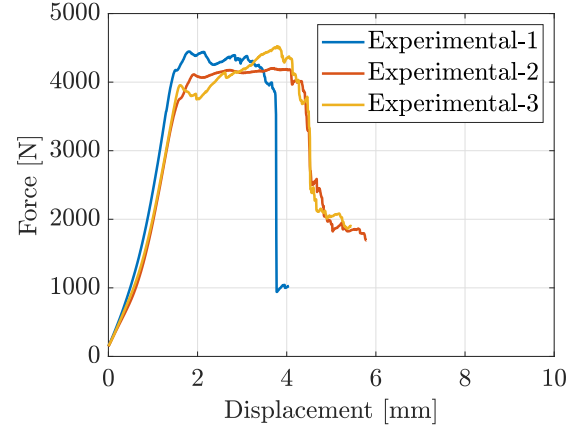


Figure 3.7: Force-displacement curves of experimental data for samples 4a. The displacements are normalized.

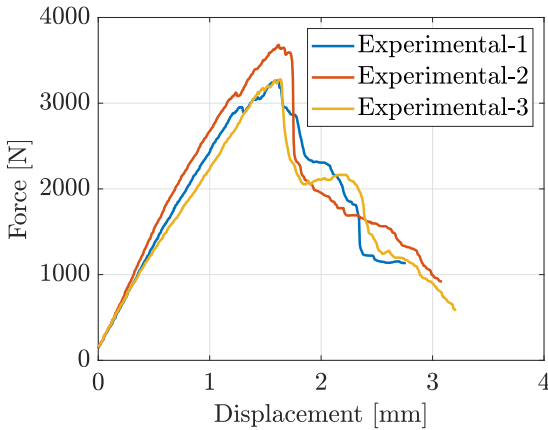


Figure 3.8: Force-displacement curves of experimental data for samples 6a. The displacements are normalized.

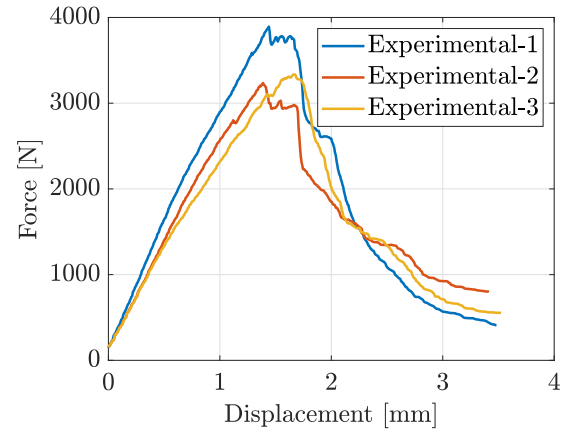


Figure 3.9: Force-displacement curves of experimental data for samples 6b. The displacements are normalized.

3.2.2 Influence of the stack-up sequence and flax fiber mass fraction.

In this section, different samples will be studied to determine the stack-up sequences and flax fiber mass fractions that maximize the performance of a hybrid composite subjected to the shear test. Based on rules requirements [9], the goal is to achieve a sample with the highest possible peak force. To compare the various results presented in Figures 3.10 to 3.15, several factors are defined like the maximum peak force F_{max} among the three replicates of each sample, the average of the three peak forces for each sample, the standard deviation between these peak forces, and finally, the energy

absorbed by the sample until it reaches F_{max} . This energy is computed using the following expression:

$$E_a = \int F dl \quad (3.1)$$

All the results are presented in Table 3.9 and will help to determine which type of stack-up sequence could serve as a basis for the development of more advanced hybrid samples.

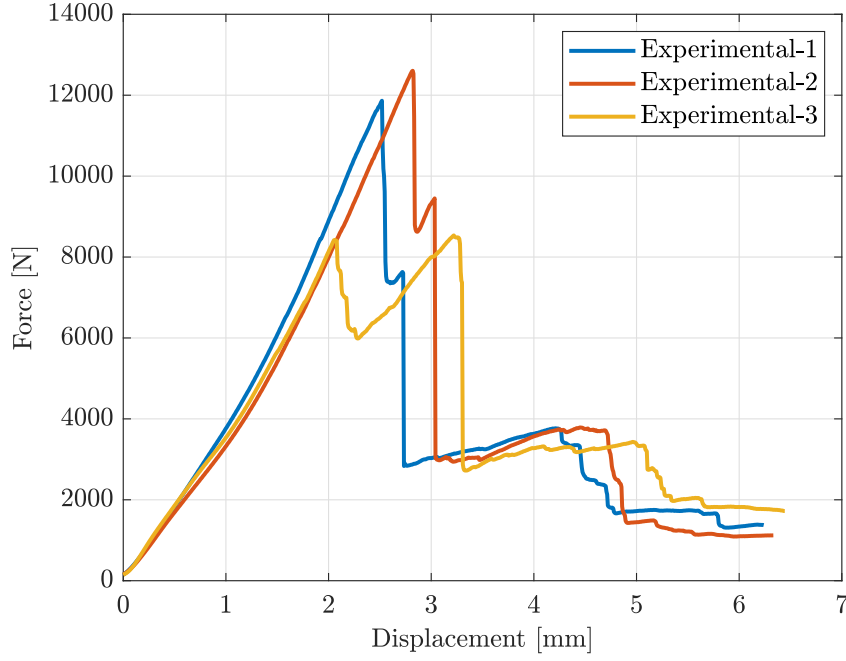


Figure 3.10: Force-displacement curves of experimental data for samples 1a. The displacements are normalized.

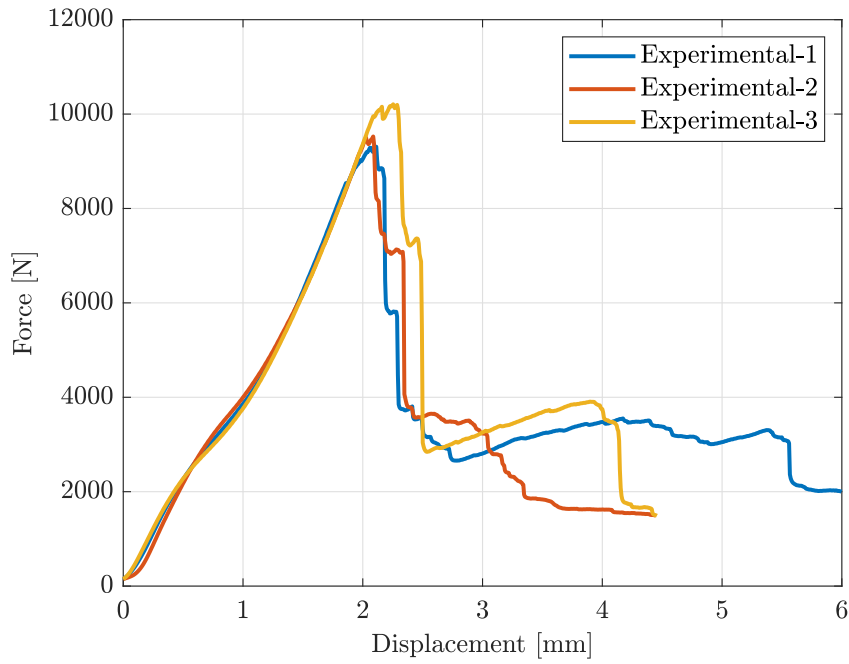


Figure 3.11: Force-displacement curves of experimental data for samples 1b. The displacements are normalized.

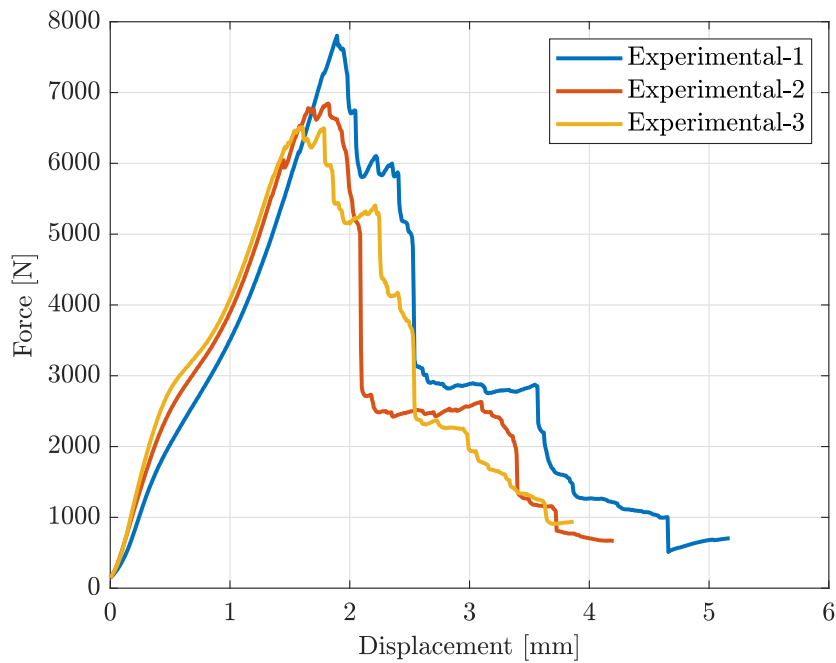


Figure 3.12: Force-displacement curves of experimental data for samples 1c. The displacements are normalized.

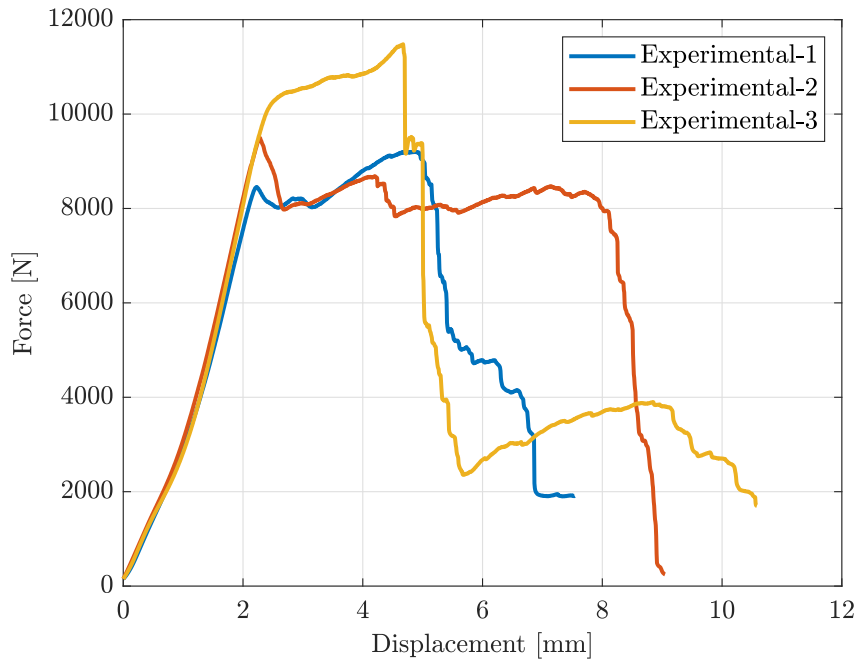


Figure 3.13: Force-displacement curves of experimental data for samples 2a. The displacements are normalized.

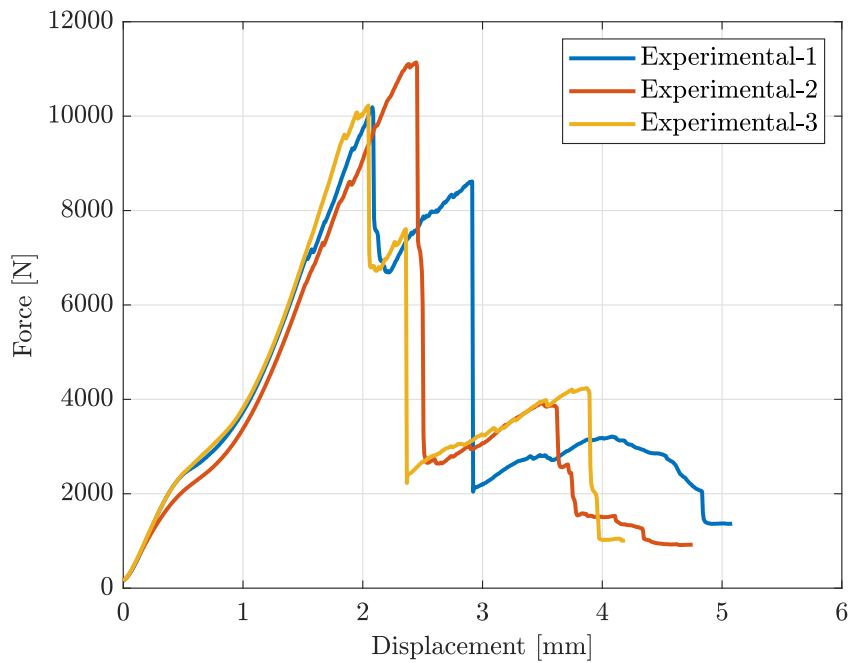


Figure 3.14: Force-displacement curves of experimental data for samples 2b. The displacements are normalized.

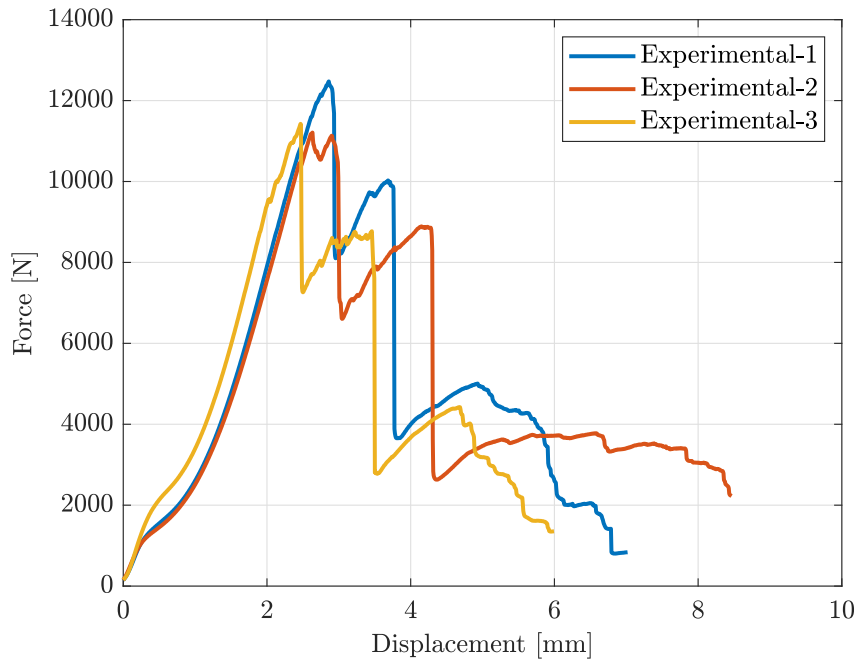


Figure 3.15: Force-displacement curves of experimental data for samples 2c. The displacements are normalized.

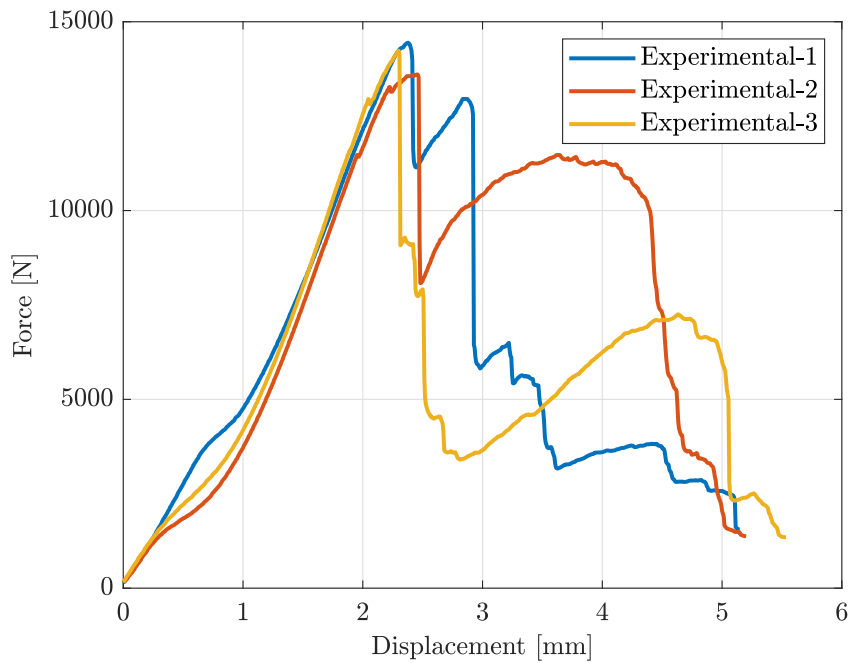


Figure 3.16: Force-displacement curves of experimental data for samples 4b. The displacements are normalized.

Samples	1a	1b	1c	2a	2b	2c
F_{max} [N]	12600	10210	7804	11480	11140	12470
Average peak force [N]	11000	9680	7053	10060	10517	11703
Standard deviation peak force [N]	2167	468	670	1237	538	676
Energy absorbed at F_{max} [J]	15.61	10.91	6.84	34.81	12.73	15.42

Table 3.9: Mass properties of the samples 1 and 2 produced.

Based on the collected data, several major observations can be made. Firstly, it can be observed that the highest F_{max} is reached by one of the samples 1a, followed by the samples 2c and 2a. For the samples 1, it appears that placing flax fibers in the outer layers of the laminate has a positive effect on the peak force achieved. For instance, sample 1a consistently reaches significantly higher peak forces on average compared to sample 1c. Additionally, the displacements at failure are greater for samples 1a and 1b. Since the material quantities are identical for these three samples, the differences in results can only be attributed to variations in the stack-up sequence. Concerning samples 2, the highest F_{max} is achieved for sample 2c, which has carbon fiber in the outer layer, which seems to contradict the observations made for sample 1. It can be also observed that the samples 2b, that have an alternate stacking sequence with a majority of carbon fiber layers, is able to obtain better results than the sample 1b. However, similar to samples 1, it seems that placing flax fibers at the outer layers of the stack-up sequence results in a rupture occurring at a greater displacement. As shown in Figure 3.14, the samples start to be perforated at distances greater than 4 [mm]. It was also observed experimentally that buckling was particularly significant and that delamination appeared in the sample. These damages can be visualized in Figure 3.17. Another observation suggests that the performances of the samples are better when the carbon fiber layers are grouped in pairs, thereby reducing the number of interfaces. In general, Table 3.9 also shows that the samples 2 consistently have higher average peak forces compared to the samples 1, as well as greater energy and a lower standard deviation. Therefore, although one of the samples 1 has the highest peak force, one can conclude that having a majority of carbon fiber layers results in better overall performance. By comparing these results with samples 3 and 4a, it is noticeable that adding respectively just 2 layers of carbon fiber and 2 layers of flax fiber in the center of their stack-up sequences results in peak forces that are three times greater. This demonstrates a positive effect of hybridization by combining the toughness of flax fiber, which provides like a damping, with the strength of carbon fiber. However, it is important to remain critical of these promising results. Although the number of fibers is lower than in samples 4b, these samples still have a weight comparable to samples 1 and 2, while achieving peak forces exceeding 13500 [N] as shown in Figure 3.16.

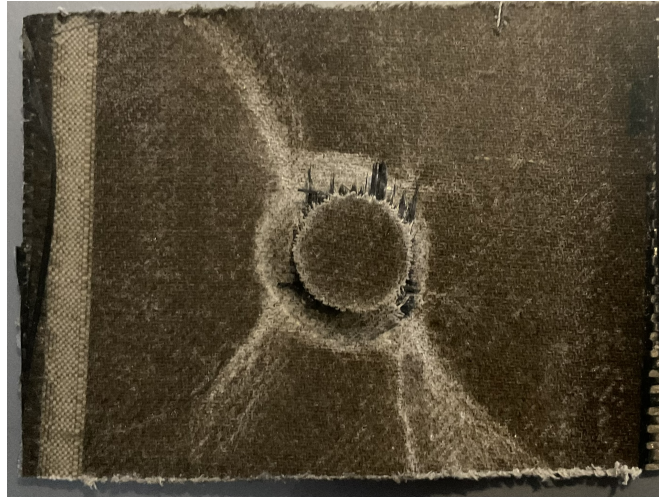


Figure 3.17: Bottom view of the sample 2a.

3.2.3 Advanced hybrid stack-up sequences

With the behavior of hybrid composite samples under the perimeter shear test now studied through simple stack-up sequences, we can use these findings to design advanced stack-up sequences aimed at configurations that could be directly applied to FBH. The idea behind the stack-up sequences of samples 5 is to have a majority of carbon fiber layers and to test different hybridization possibilities, while also aiming to maximize the placement of carbon fiber layers in pairs. The different results are shown in Figure 3.18 to 3.22 and resumed in the Table 3.10.

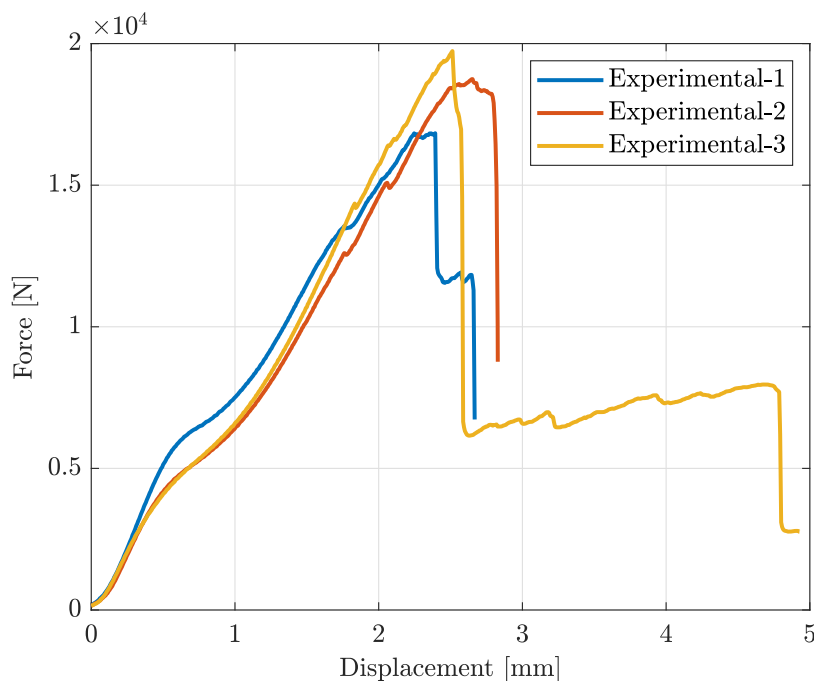


Figure 3.18: Force-displacement curves of experimental data for samples 5a. The displacements are normalized.

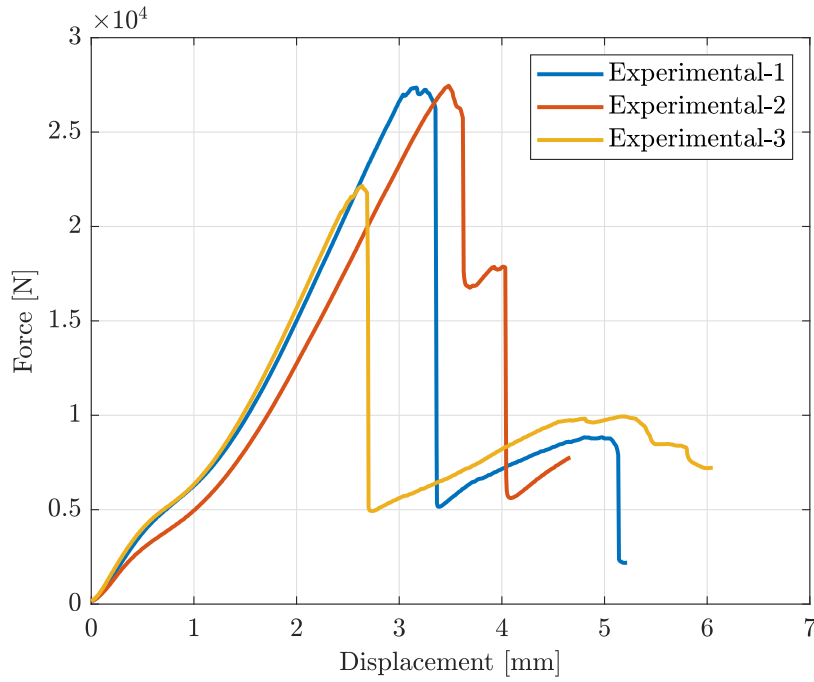


Figure 3.19: Force-displacement curves of experimental data for samples 5b. The displacements are normalized.

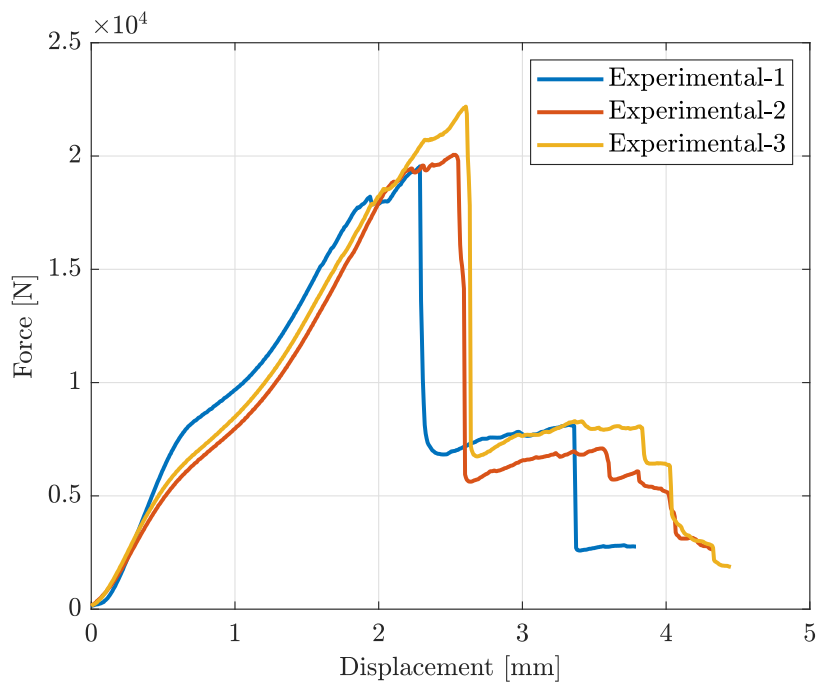


Figure 3.20: Force-displacement curves of experimental data for samples 5c. The displacements are normalized.

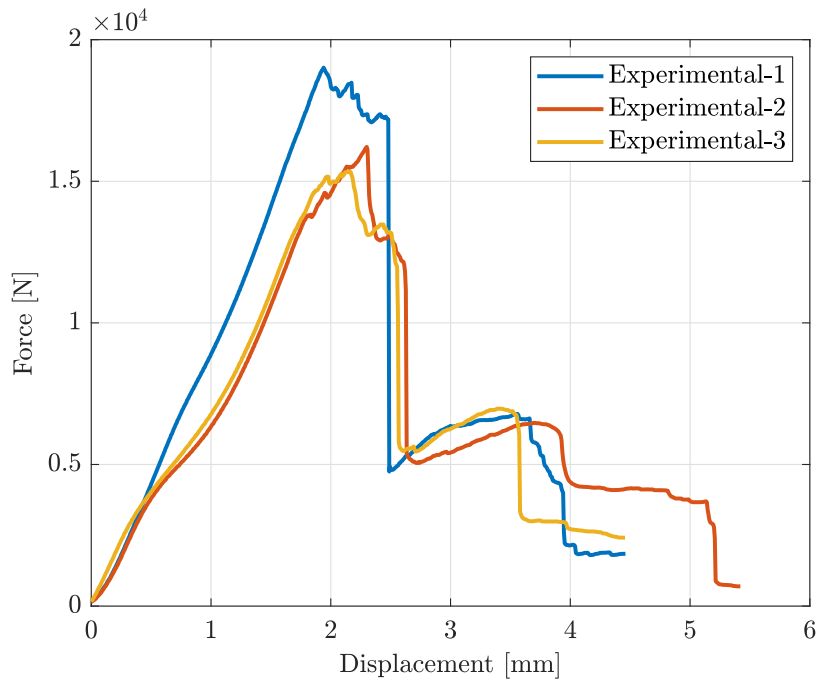


Figure 3.21: Force-displacement curves of experimental data for samples 5d. The displacements are normalized.

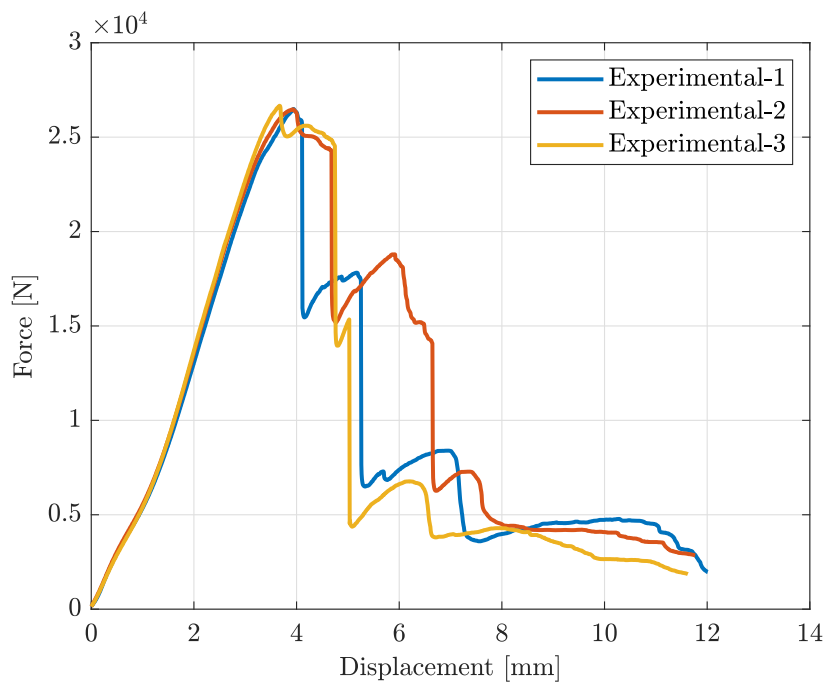


Figure 3.22: Force-displacement curves of experimental data for samples 5e. The displacements are normalized.

Samples	5a	5b	5c	5d	5e
F_{max} [N]	19730	27454	22130	19010	26660
Average peak force [N]	18438	25655	20594	16853	26541
Standard deviation peak force [N]	1474	3035	1398	1921	103
Energy absorbed at F_{max} [J]	23.7	41.32	30.06	17.34	47.17

Table 3.10: Mass properties of the samples 5 produced.

When examining the results, the first major observation is that samples 5b nearly reaches the minimum force of 28000 [N] required by the regulations for the FBH [9]. The differences in the results among the samples are quite pronounced, as all sample reach significantly lower peak forces, except sample 5e. The performance of sample 5b appears very promising, as this configuration achieves a maximum force 2.17 times higher than that of samples 1 and 2, while only having a weight that is 1.36 times higher. Although samples 5e have a higher average peak force and absorbed energy, the fact that sample 5b exceeds 27000 [N] in two different tests allows us to conclude that it is the best configuration. These results can be explained by several factors. Firstly, the outer layers are made of flax fiber. As a result, when the load applicator comes into contact with the sample, the flax fiber allows for better stress distribution around the contact area due to its greater elongation [38]. This helps to avoid stress concentrations that can lead to matrix cracks on the top layer, which is often the case with carbon fiber. Moreover, as it can be seen in Figure 3.5, the flax and carbon fibers appear to be evenly distributed throughout the thickness of the sample. Based on the failure mechanism for hybrid composites developed in [15], since the carbon fiber layers are surrounded by flax fibers, when the carbon fiber layers reach the failure strain, they fracture and release energy. This energy is absorbed by the adjacent flax fibers, thereby reducing the propagation of the failure. For sample 5e, this phenomenon is less pronounced since the flax and carbon fibers are not alternated. However, as shown in Figure 3.23, the sample experiences delamination. This type of damage helps to explain why the force-displacement curve, illustrated in Figure 3.22, shows a rebound even after the sample has failed.

Given the performance of sample 5b, it seems reasonable to hypothesize that by adding a layer of carbon fiber to the center of the stack-up sequence of sample 5b, a hybrid composite named ‘Sample 5f’ could potentially exceed the 28000 [N] threshold. Based on various measurements, the areal weight of this hybrid composite could be approximated at 4.7 [kg] per square meter, which is 22% lighter than the areal weight of the current composite skin used in the FBH sandwich structure. In addition to this mass advantage, sample 5f would also be more environmentally friendly. According to [22], the global warming potential of carbon fiber is 14.96 times higher than that of flax fiber. Therefore, neglecting the impact of the epoxy resin used, it is estimated that per square meter of material, sample 5f would have a global warming potential 43.21% lower than that of the FBH, which is composed solely of carbon fibers. However, it is important to remember that these are only estimates. The purpose of this example is to demonstrate that the hybrid samples designed in this chapter are serious candidates for future FBH lay-ups. Several crucial steps still need to be addressed. Most of the samples tested in this study are composed of woven fibers oriented at 0 [°]. However, according to rule T3.4.3 of the regulations [9], this type of lay-up is not permitted for designing parts of the monocoque. Therefore, while the conclusions of this study are valuable, further optimization is necessary to determine the ideal amount and orientation of both woven and unidirectional fibers. This optimization should also consider the stack-up sequence and the flax fiber mass fraction to achieve a hybrid configuration that maximizes composite performance. Additionally, it is essential

to ensure that a representative sample of the lay-up undergoes a three-point bending test. The hybrid lay-up must be able to pass this test, which is generally straightforward for lay-ups designed for the FBH.

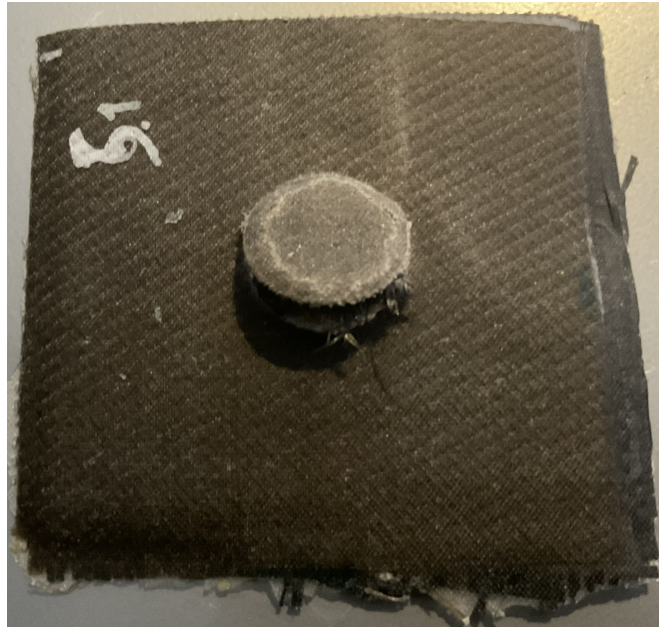


Figure 3.23: Bottom view of the sample 5e.

3.3 Conclusion

Although the study of hybrid composites presented in this chapter focuses on the perimeter shear test, several general conclusions can still be drawn. The vacuum-assisted resin infusion process appears to be an effective manufacturing method for producing high-quality hybrid composites from dry fibers. However, it was observed that flax fibers tend to absorb a significant amount of resin, leading to an increase in the mass of the composites and a reduction in their mechanical properties. Therefore, future development of hybrid composites should include the creation of pre-impregnated flax fibers that can achieve the same level of epoxy mass fraction as carbon fiber prepreps.

Thanks to the experimental tests conducted on hybrid samples, it was initially concluded that the hybridization of carbon fiber with flax fiber seems to have a positive effect on the results. The study revealed that the stacking sequence and flax fiber mass ratio are the parameters that most significantly influence the performance of hybrid composites. Various promising patterns were identified to create advanced hybrid composite configurations. For instance, samples 5b, which have an alternating stack-up sequence, are capable of reaching a maximum force of 27454 [N] when subjected to the shear test. This type of stack-up sequence takes full advantage of the toughness and impact absorption benefits of flax fiber, thus avoiding the brittle-like crash behavior typically observed in carbon fiber composites. Based on this observation, it can be hypothesized that a sample using this stack-up sequence with an additional layer of carbon fiber could exceed the minimum force required by the regulations. The resulting composite would therefore be more sustainable and 22% lighter.

However, before these hybrid composites can be practically implemented, several parameters still need to be optimized. Notably, the number of variables to consider in these hybrid configurations is greater than in purely carbon fiber setups, which necessitates significantly more testing. Incorporating simulations into the optimization process would be a major step forward in composite testing strategies, allowing for considerable time savings.

CHAPTER 4

Numerical model of the perimeter shear test

In this chapter, Ansys Workbench will be used to create a numerical model of the perimeter shear test. The goal of the simulations is to generate a force-displacement curve that allows for the identification of first ply failure, similar to what can be achieved through experimental tests. Each simulation will be calibrated based on tests conducted on samples to ensure that the numerical results are physically valid. However, it should be acknowledged that this type of simulation is not trivial and involves modeling non-linearities that increases the complexity of the model. Specifically frictional contacts, large deformations, and damage modeling will be addressed, which will significantly increase the computational cost of the simulations. Given that the computer used is equipped only with an *Intel(R) Core(TM) i7-8565U CPU @ 1.80GHz*, the time required for simulations will quickly become a limiting factor, especially since the aim of using numerical simulations in composite design is to expedite the procedures.

4.1 Modeling and parameterization

The finite element modeling of the perimeter shear test is a crucial step in this study. The objective is to accurately replicate the experimental test conditions in a numerical environment with the highest precision. In the laboratory, the composite sample is placed on a rectangular parallelepiped in steel attached to the test machine. The sample must not be clamped to this support, but must be centered with it. The load applicator is a steel cylinder which must be placed in contact with the surface of the sample before starting the test. Therefore, from a physical perspective, the boundary conditions involve frictional contact between the support and the sample, as well as between the sample and the cylinder.

Initially, the plan was to simulate the test by modeling only the sample plate and applying a force to its upper surface in one step, similar to that applied by the load applicator. The magnitude of this force would have been determined based on the minimum value required to pass the test, as specified in the regulations, and related to the area of the tested monocoque. However, since this type of modeling does not accurately represent the interactions between the sample, the support, and the load applicator, it was decided to model the entire system instead with a multiple step loading. As explained in the Chapter 1, the shear test is designed to evaluate samples in the form of a sandwich structure. However, finite element modeling of core materials, such as aluminum honeycomb, is a complex topic in itself [39, 40]. Therefore, the model presented here will just focus on the laminate layers located on the external surfaces of this sandwich structure. In this way, the number of finite element can be decreased, leading to simpler and faster simulations. Moreover,

since the simulation will be calibrated with experimental tests, this approach eliminates the need to fabricate full sandwich structure samples, requiring only the skin layers, thereby saving both materials and time in the manufacturing process.

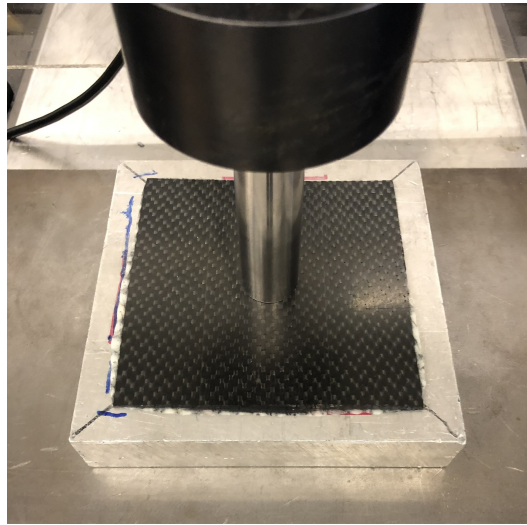


Figure 4.1: Sample under experimental conditions for the perimeter shear test.

4.1.1 Geometry

The geometric model of the shear test is divided into two sub-assemblies, defined independently and then assembled after their respective meshing. The first sub-assembly consists of the composite material sample to be tested, while the second includes the support and the load applicator. The sample is modeled in SpaceClaim and is essentially a 100 [mm] by 100 [mm] square, as specified by the regulations. This square is afterward inflated in Ansys Mechanical Composite PrepPost (ACP) according to the desired lay-up. Consequently, its thickness will vary depending on the number of layers and the characteristics of the plies used. The support and load applicator are modeled together in DesignModeler within the same file. This allows for adjustments to the sample thickness by directly raising the applicator as needed. Based on the dimensions specified by the regulations, the support is a rectangular parallelepiped with sides of 110 [mm] and a height of 5 [mm]. It is perforated in the center with a circular hole of 32 [mm] in diameter. The load applicator, on the other hand, is a cylinder with a diameter of 25 [mm] and a height of 5 [mm]. In both cases, the height was chosen arbitrarily to ensure an accurate representation while minimizing the number of finite elements in these components. In reality, the support has a height of 80 [mm] and the cylinder 100 [mm] to ensure that, when tested, they can fully penetrate the sandwich structure, which can exceed 50 [mm] in thickness. For the simulations, the thickness of the tested skins allows for reducing the height of these elements without being physically constrained by them. Additionally, the load imposed on these steel components is considered negligible, so there are no structural issues associated with their reduced thickness. The edges that grid the support are intended to facilitate the creation of an optimized mesh. These aspects will be explored in greater detail in the Section 4.1.2.

The description of the perimeter shear test permit to easily understand that geometry and loading are symmetrical. To reduce the number of finite elements and therefore the computation time, the analysis could be restricted to only one half of the model. However, due to the coupling effects

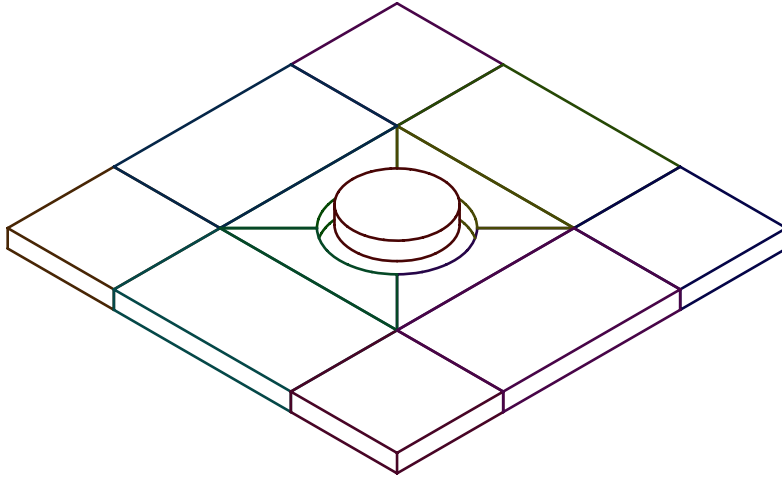


Figure 4.2: 3D geometric model of the perimeter shear test.

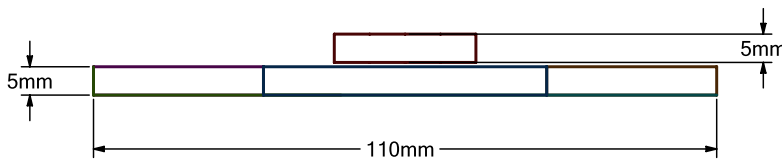


Figure 4.3: Side view of the geometric model.

explained in Section 2.3.1, the deformation of the sample may not be symmetrical. Given that these simulations could also be applied to samples with non-symmetrical and non-homogeneous lay-ups, it was decided that, initially, the entire geometry would be modeled and studied.

4.1.2 Mesh

Just like the geometry, the meshing will be divided into two parts. The first concerns the sample mesh, while the second relates to the support and the load applicator. During loading, the sample will be in contact with the applicator through its lower surface, which is shaped like a disk. Consequently, the upper face of the sample has been cut out to define this contact area between the sample and the cylinder. As a result of this choice, the circular edge in the center of the square sample tends to promote the formation of tetrahedral elements. A similar observation can be done for the support, which has a 32 mm diameter hole in its center. However, for simple geometries, such as in this case, the use of hexahedral elements is recommended because they provide more reliable results [41, 42]. It was therefore decided to draw inspiration from meshing models used for holed plates [43, 44, 45], using only hexahedral elements.

For the laminate sample, a multi-zone quad/tri method is first applied across the entire plate to achieve a mapped mesh. Next, by using the zone divisions made during modeling and illustrated in Figures 4.4 to 4.8, a face sizing is applied to the central and intermediate area to define the size of the elements. Since these zones are in contact with the load applicator and the supports, their elements must be the smallest on the plate to ensure the most accurate representation of stress and contact-related effects. Additionally, to obtain a mesh consisting only of hexahedral elements, the method requires that

the element size gradually increases from the central area to the plate sides. Therefore, during the meshing, Ansys will automatically slightly decrease the size of the mesh for the intermediate zone to create a smooth transition between the refined mesh in the center and the larger elements in the outer zone. This approach allows for varying the element size based on their location, while ensuring that only hexahedral elements are used. The central zone will contain some slightly deformed elements, and the intermediate zone may have parallelograms, but the overall quality of the final mesh will be maintained. Due to the phenomena being represented in the simulation, the physics preference was set to 'Nonlinear Mechanical' to achieve a smoother and gradually changing mesh. After element size, the order of the elements is one of the most important factors affecting the accuracy of the results. Indeed, first-order elements are also called linear elements since they have only nodes in the corner of each element and calculate displacement linearly between these nodes. Second-order elements or quadratic elements permit to compute displacement quadratically since they have also nodes between the corners. Thus, the results are more accurate, but the computation cost is increased [41, 42]. In this case, this parameter was set to 'Program controlled'. In this way, Ansys will automatically select suitable locations for second-order elements and place first-order elements in other areas. This approach permit a balance between high accuracy and low computational cost. Note that for composites, the meshing is first performed in Ansys Mechanical to obtain shell elements. It is only when the lay-up is defined in ACP that these elements are converted into solid elements. This way, the number of elements through the thickness of the sample depends on the number of plies in the lay-up.

The support and load applicator are meshed in the same way. After applying the multi-zone method, three zones are defined. The central zone will have the most refined mesh, as this area will be primarily in contact with the sample during loading. However, as it can be seen on the Figure 4.10, the outer zones are extensions of the central zone. The areas in the corners of the support do not require a high number of elements due to their minimal interaction with the sample. Inversely, for the cylinder, the number of elements will be relatively large because, although it only transmits the load to the sample, its interactions via contact with the sample are still significant. As for the composite sample, the physics preference was set to 'Nonlinear Mechanical' and the order of elements to 'Program controlled'. However, in this case, solid elements are obtained directly. The number of elements through the thickness of the support was deliberately set to one in order to reduce the number of nodes. Since the support is fixed and not part of the study, it does not require a refined mesh in the direction of its height. Details regarding the element size and mesh quality will be provided in the Section 4.2.3 dedicated to the mesh convergence analysis.

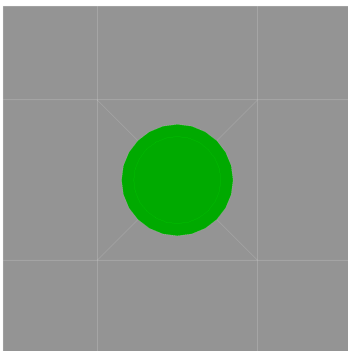


Figure 4.4: Central zone of the sample.

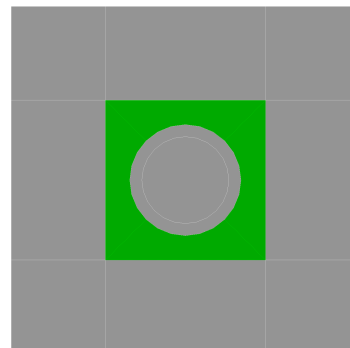


Figure 4.5: Intermediate zone of the sample.

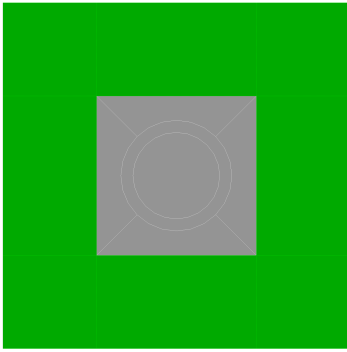


Figure 4.6: Outer zone of the sample.

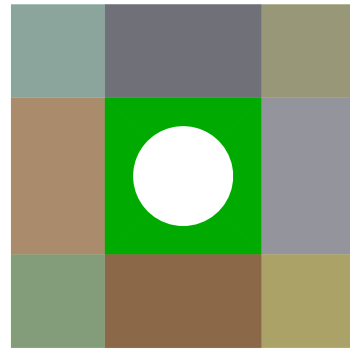


Figure 4.7: Central zone of the support.

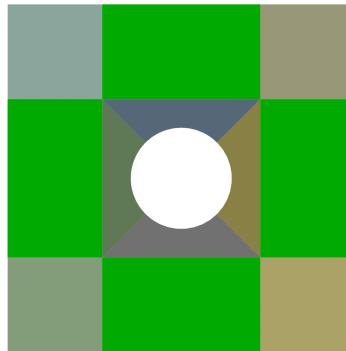


Figure 4.8: Outer zone of the support.

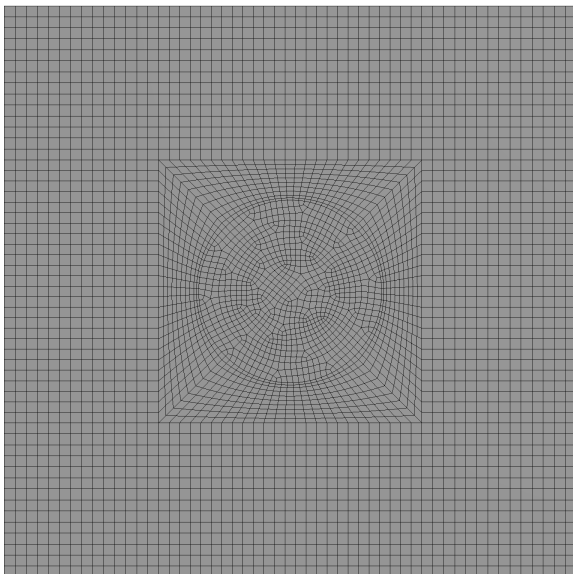


Figure 4.9: Mesh of the plate.

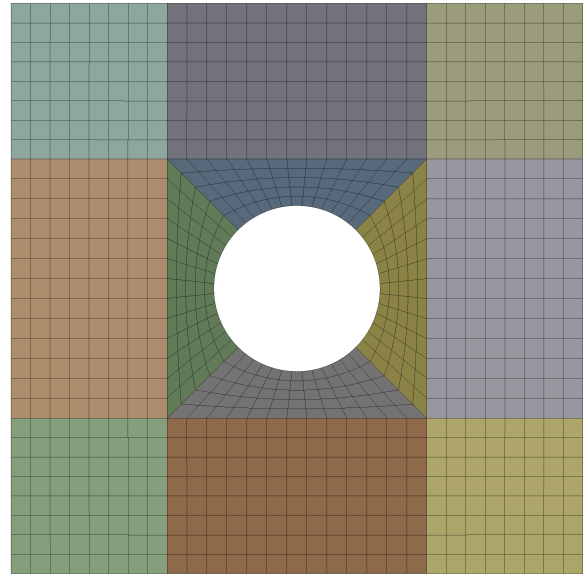


Figure 4.10: Mesh of the support.

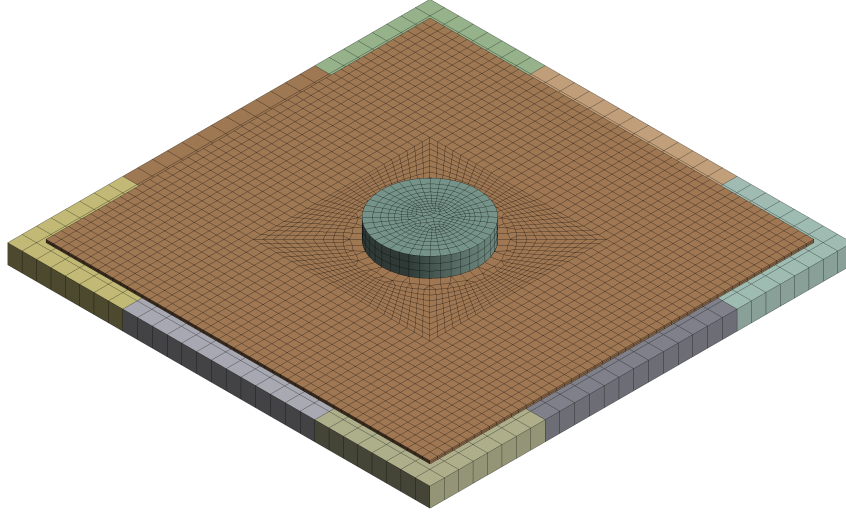


Figure 4.11: Isometric view of the meshed assembly.

4.1.3 Contact definition

As explained at the beginning of this chapter, during the experimental testing procedure, the sample interacts with the support solely through frictional contact, as it is simply placed on top of it. When the lower surface of the load applicator and the upper surface of the sample begin to touch each other, this interaction is also governed by frictional contact. However, although frictional contacts are the most accurate, they are intrinsically nonlinear and involve therefore multiple calculation that make simulations computationally very expensive. This also tends to increase the likelihood of non-convergence in the simulations [46]. Therefore, in the first part of the analysis, as developed in the Section 4.2.1, simplifying assumptions based on observations will be tested to make the simulations computationally less expensive by considering that the sample is bonded to the support along a circular area at the upper surface of the hole in the support. This type of contact is illustrated in Figure 4.12 and means that the two bonded edges cannot separate or slide relative to each other.

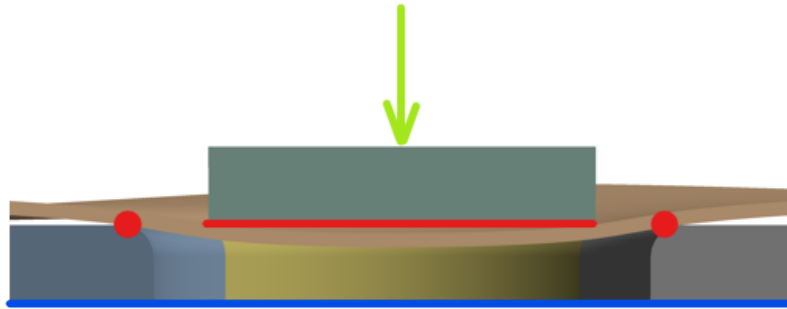


Figure 4.12: Boundary conditions and contacts.

Concerning frictional contacts, the two surfaces concerned can separate in the normal direction and slide with a resistance μ in the tangential direction using the governing equation:

$$F_t = \mu F_n \quad (4.1)$$

where F_t is the tangential force and F_n the normal force. For CFRP, the value of the friction coefficient μ is equal to 0.11 [47], while for FFRP, it is equal to 0.155 [48]. In Ansys, the first step in the frictional contact definition is the setting of the contact and target face. For asymmetric behavior, the contact side must be assigned to the surface with a finer mesh to avoid the interpenetration of the physical bodies. Indeed, a fine mesh means a high number of detection points and, according to the contact algorithm, contacts detection points cannot penetrate into a target surface thus allowing for an accurate representation of the phenomenon [49]. Advanced settings for defining frictional contacts will be discussed in the Section 4.2.1.

4.1.4 Boundary conditions and number of solution steps

During the perimeter shear test, the load applicator imposes a displacement on the test plate. Consequently, the machine must apply a force to counter the reaction force of the plate resisting this displacement. This force can be measured and plotted on a force-displacement graph, which allows for determining the force corresponding to the complete failure of the sample. Initially, Formula Electric Belgium set the initial objective of this work as simply modeling the shear test to determine whether a sample could withstand an imposed force in a single-step solution. However, this approach has two problems:

1. **Limitations in failure detection:** One-step simulation only determines whether a sample fails or not, but it does not provide the exact forces at which failure begins. Therefore, it is difficult to draw conclusions from the simulations and adjust the design of the lay-up.
2. **Inaccuracies in deformation representation:** It has been observed that a solution with only one load step cannot accurately represent the deformation of the sample, especially the buckling phenomena that may occur under certain conditions. Moreover, for problems with complex convergence, they can be achieved by increasing the number of load steps [50].

The solution to these issues is to implement a multistep approach using remote displacement as the loading type. Although the decision to use remote displacement rather than remote force may seem also arbitrary, the goal is actually to represent the loading as it is applied in reality by the machine. This remote displacement is applied on the upper surface of the cylinder and consists of a negative displacement in the z direction, while all other displacement and rotation are respectively set to 0 [mm] and 0 [°]. Therefore, extracting the reaction force from this surface will allow us to plot the force-displacement curve. The behavior is set to 'Deformable' and the value of this displacement can be modified following the tested sample and can be decomposed as a linear displacement based on the number of steps and substeps defined. These settings can be adjusted based on the desired accuracy or to facilitate convergence. This is precisely the purpose of substeps, which allow for additional increments between the last converged step and the unconverged one. It is possible to define a minimum and maximum number of substeps following the complexity of the convergence. However, it is important to note that a large number of steps and substeps will significantly increase the computational cost. This parameter will be study in detail in the Section 4.2.2. Finally, the base of the support was fixed to restrict all its degrees of freedom.

4.1.5 Solver parameters

Quasi-Static solution

In the experimental procedure for the perimeter shear test, the loading rate of the machine is set at 4 [mm/min]. This very low speed allows the problem to be considered static at a given moment and thus enables the activation of the quasi-static solver control. This option permits to improve convergence in situations where inertial effects are negligible, and was therefore used in all the simulations of this work [51].

Large deflection

During the experimental tests conducted in this chapter, the samples had a very low thickness, ranging from 0.7 [mm] to 2 [mm]. It was observed that, for all configurations, the deformation of certain parts of the tested plate could reach values between 3 and 5 [cm]. Given the high degree of deformation, it is justifiable to use the Ansys solver option that considers large deformations. The utilization of large deflection (LD) in Ansys allows the solver to account for changes in stiffness due to the deformation of the parts being simulated. When large deflection is enabled, Ansys adjusts the stiffness matrix dynamically as the structure deforms, providing a more accurate representation of the structural behavior under significant loads. On the contrary, without enabling large deflection, the analysis is constrained to using linear equations, which assume that the stiffness of the structure remains constant regardless of how much it deflects. This approach does not accommodate the changes in stiffness resulting from large deformations, potentially leading to inaccurate results. However, enabling large deflection introduces additional computational expense. This is because the analysis becomes nonlinear, requiring multiple iterations through the solver using the Newton-Raphson method to converge on a solution. Unlike linear problems, which only require a single pass through the solver [52].

4.2 Simulation parameters calibration

The purpose of this section is to calibrate the various simulation parameters previously explained. To achieve this, three composite laminates named 'Samples 7' were fabricated and tested to compare the experimental and numerical results. This comparison focuses not only on the force-displacement graph but also on the behavior of the sample under the applied displacement. These composite samples were manufactured using the variant of the prepreg compression molding explained in the Section 3.1.1 and HexPly M26 woven prepreg as raw material for the plies. The properties of these sample can be retrieved in the Tables 4.1 and 4.2. Although the lay-up of these samples is basic and significantly different from those used in monocoque structures, the objective here is to have a simple configuration that allows for rapid testing of the model and the various parameters discussed in the previous section, in order to closely approximate the experimental results. Thus, the conclusions from this calibration will allow the parameters to be used for any sample, regardless of its lay-up and the material used. It was observed that depending on the chosen types of contact, the stress distribution in the plate varied and could potentially lead to stress concentrations. Therefore, it was decided to begin with the study of contact before addressing mesh convergence and the number of steps. For this reason, these parameters will be arbitrarily set with an overly cautious approach during the contact calibration to ensure they do not distort the study. The remote displacement was set to a maximal value of 1 [mm]. This value is arbitrarily set to exceed the thickness of the sample

and closely match the FPF conditions observed experimentally around 1 [mm], providing a reference point.

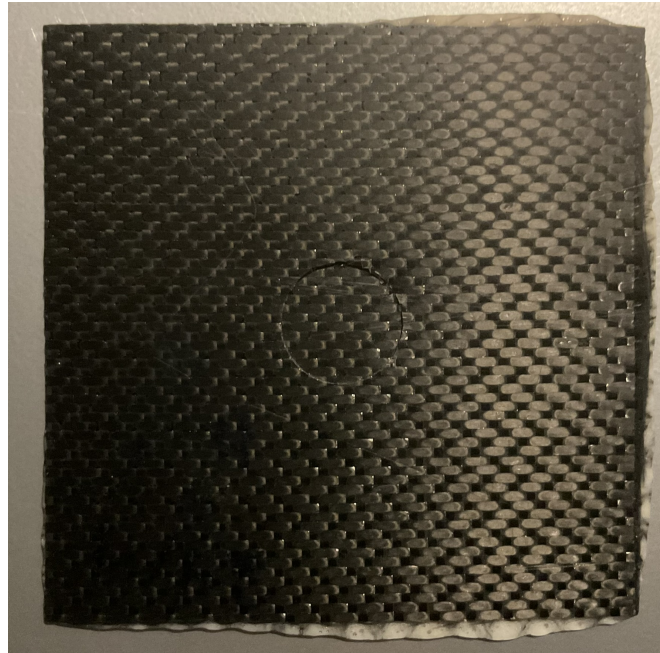


Figure 4.13: Sample 7.

	HexPly M26
Density [kg/m^3]	1549
E_x [GPa]	63.5
E_y [GPa]	63.5
E_z [GPa]	10
X_t [MPa]	790
Y_t [MPa]	790
Z_t [MPa]	80
X_c [MPa]	-700
Y_c [MPa]	-700
Z_c [MPa]	-200
Ply type	Twill 2x2

Table 4.1: Main mechanical properties of the selected material. The data are exported from ESAComp.

	Lay-up	Thickness [mm]
Samples 7	[0F/0F]	0.764

Table 4.2: Lay-up and thickness of the samples 7 produced and used for simulations.

4.2.1 Contact calibration

The purpose of this calibration is to determine which type of contact provides the most representative results for the perimeter shear test. This step is crucial, as the model consists of three bodies interacting through contacts. These contacts will have a significant influence on the calculated stresses and deformations, as well as on the selection of numerical parameters used. The ideal configuration detailed in Table 4.4 was used and the number of step was fixed to 40 in order to enhance the accuracy of the results and ensure convergence while avoiding excessive computational cost. It is important to note that the end of the curves corresponds to the end of the imposed displacement, not to the failure of the material, which is not accounted for in this case. As a result, material failure could potentially occur either before or after the imposed displacement is reached.

When observing the behavior of a composite sample subjected to the perimeter shear test, the initial assumption one might make is to neglect the effects of friction and consider the plate as simply bonded to the support and the load applicator at the points of contact. These contacts were defined as shown in the Figures 4.14, 4.15 and 4.16 and simulated without considering large deflection. As expected, the computation time was only 4 [min] and 54 [s] and the force-displacement curve obtained from this first simulation is shown in Figure 4.20. As it can be seen, this result is far from the experimental ones due to its linearity and very steep slope. Indeed, the bonded contacts do not allow any relative displacement between the surfaces and thus, in a way, increases the rigidity of the plate with respect to the imposed displacement while concentrating the stresses in the contact areas. As a result, the force values obtained are excessive and do not accurately represent reality. It is therefore clear that the assumption of bonded contact is invalid and that accurately representing the sliding phenomena between the plate, the load applicator, and the support is crucial for the accuracy of the results.

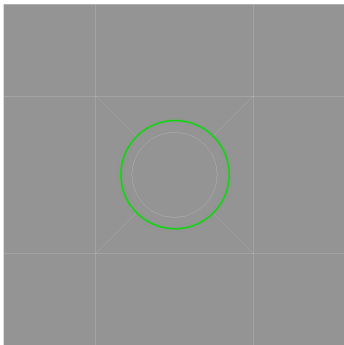


Figure 4.14: Bonded edge for contact between the sample and the support.

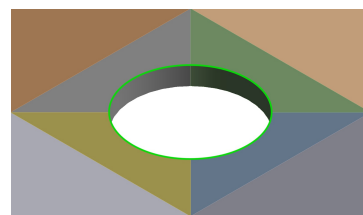


Figure 4.15: Bonded edge for contact between the support and the sample.

Indeed, experimental observations showed that during the loading, the center of the plate literally slips into the central hole of the support due to the movement induced by the load applicator. A new simulation was configured, maintaining the same contact area as in the previous case for the cylinder, but this time incorporating friction on the entire top surface of the plate. However, it quickly became evident that using frictional contacts would be more challenging than anticipated, as the simulation failed to converge right from the first load step. To address this issue, the advanced contact settings were adjusted according to the recommendations of [53, 54, 55]. In this way, the formulation was

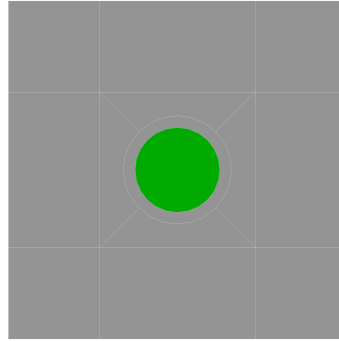


Figure 4.16: Surface defined for bonded and frictional contact between the sample and the load applicator.

set to 'Normal Lagrange', the detection method to 'Nodal-Normal To Target', the normal stiffness was reduced by 20% and the Newton-Raphson option to 'Unsymmetric' but the simulation still failed to converge right from the first displacement step. Even with the smallest possible mesh, the problem persisted. Therefore, it was concluded that this divergence was not due to the nonlinearities themselves, but to the definition of the contact areas. To prove that, a new simulation was set by keeping the contact between the two edges of the support and the plate as bonded while the contact between the composite sample plate and the load applicator was set to frictional. This time, the simulation converged without any issues, allowing the results to be compared with the experimental curves on the Figure 4.20. One can notice that the maximal force and therefore the slope are much more realistic than for the first case, demonstrating that the inclusion of friction has a positive impact on the results. However, this curve is still linear while the experimental are non-linear. To resolve this issue, the solver can be configured to account for large deflections, though this comes at the cost of increased computational cost. The obtained curve is shown on the Figure 4.20 and has now the same non-linear shape than the experimental curves. However, the maximal force has once again become significantly higher. Although more realistic, this latest simulation confirms that imposing friction on all contacts yields the most accurate results and that the issue primarily lies with the contact between the support and the plate.

When approaching the solution of a problem using finite element analysis, one of the first and most crucial steps, though often understated, is the simplification of the model. In this study, several simplifications have already been mentioned, though deemed irrelevant, such as modeling only half of the structure or neglecting frictional contacts between various components. However, one final, much more subtle simplification has not yet been addressed: minor geometrical corrections, such as removing small fillets and rounds [56]. According to the strict geometric description outlined in the regulations, neither fillets nor rounded edges are part of the support or the load applicator. However, upon close examination of the parts used in the laboratory, a slight rounding is noticeable around the central hole of the support. This rounding, caused by the machining process and the wear of the piece, has not been previously mentioned due to its very small radius. Nevertheless, due to the convergence issues related to friction, this rounding will now be modeled to reduce the frictional contact surface between the elements while promoting the sliding of the plate into the hole. The radius was measured using calipers and estimated to be between 1.8 and 2 [mm], but it will be rounded to 2 [mm] to simplify the modeling, as shown in Figure 4.17. Consequently, two new frictional contact surfaces are defined as illustrated in the Figures 4.18 and 4.19 and permit now the simulation to converge

without any issues. The Figure 4.20 shows that the obtained curve exhibits nonlinear behavior with a maximum force relatively close to the experimental curves. Therefore, this configuration, which uses frictional contacts and accounts for large deflections, appears to best match the experimental results, although some discrepancies still need to be addressed. From the perspective of the sample's deformation, it is evident in Figures 4.22 and 4.23 that the result closely resembles the experimental observations, whereas simulations with bonded contact conditions show exaggerated deformation that does not seem to model the correct deformation mode of the plate. In the first case, the plate deforms almost uniformly, with maximum values observed at the external edges. However, the second figure illustrates a buckling effect, with a maximum deformation occurring at the midpoint of the plate's external edge. This difference is attributed to the fact that in the second case, the solver considers large deflection effects. Finally, the computation time for this simulation is 28 [min] and 49 [s], which is more than five times longer than the simulation where friction is neglected. It is therefore clear that the inclusion of contact non-linearities and large deflection significantly increases the computational cost.

Although the curve obtained in the latest simulation is satisfactory, it is still essential to question the potential causes that might explain the variances with the experimental samples:

1. **Incompletely cured matrix:** As explained in Section 3.1.1, the samples 7 experienced incomplete curing due to uneven pressure and temperature distribution. Consequently, a significant number of voids can be observed within these laminates. These defects degrade the mechanical properties of the composite materials and are not accounted for in the simulations [57, 58, 59]. Therefore, it is possible that the differences in slope and maximum force can be attributed to these phenomena. It is also worth noting that the fiber used in this experiment is expired carbon fiber prepreg, which may further amplify the occurrence of the aforementioned defects [60].
2. **Numerical inaccuracies:** According to [61], solid elements used by ACP have a limitation since they tend to be too stiff in bending, particularly when the elements are thin. This can result in significant errors in displacement calculations, with inaccuracies that may be off by an order of magnitude due to a phenomenon known as locking. Using a higher number of quadratic elements can help reduce this error.

Consequently, the manufacturing process of the samples will be modified for the production of future specimens to prevent results from being affected by manufacturing defects, and the increase in the number of quadratic finite elements will be considered if necessary. Thus, it will be possible to enhance the correlation between the simulations and the experimental tests, allowing for a more detailed analysis of the sample behavior in the Section 4.3.

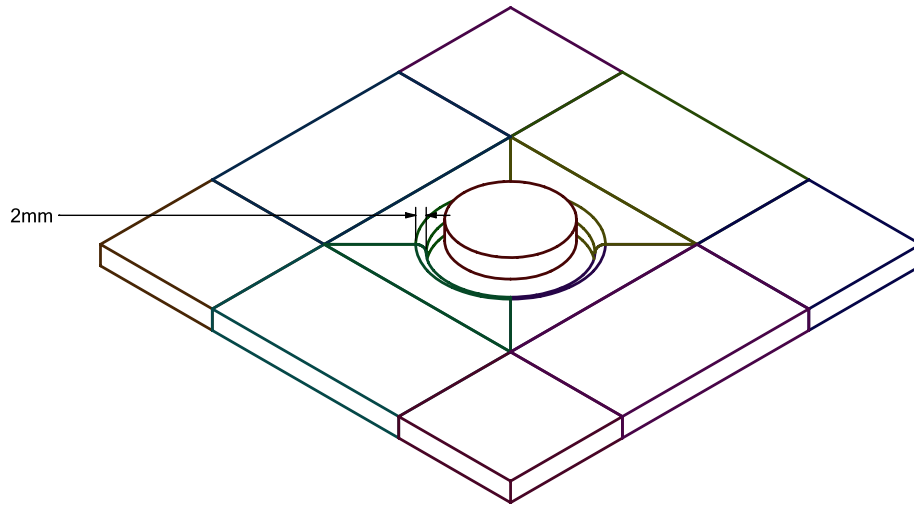


Figure 4.17: Isometric view of the new geometry.

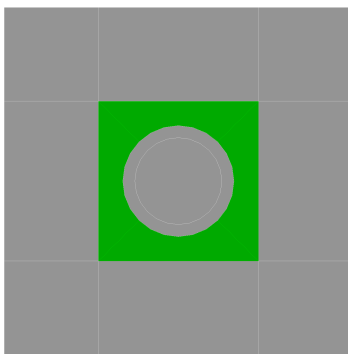


Figure 4.18: Surface defined for frictional contact between the sample and the support.

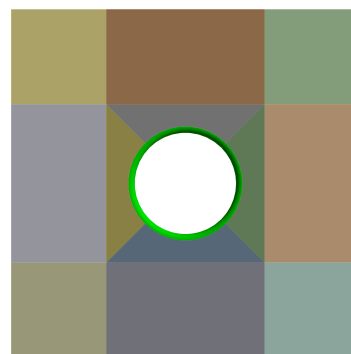


Figure 4.19: Surface defined for frictional contact between the support and the sample.

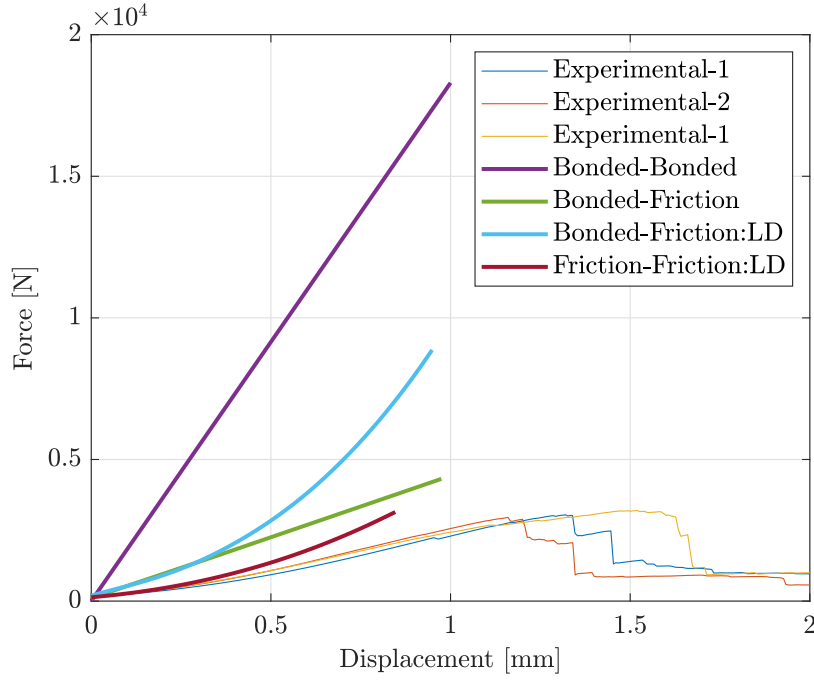


Figure 4.20: Force-displacement curves for different types of simulations compared with experimental curves for samples 7. Displacement are normalized.

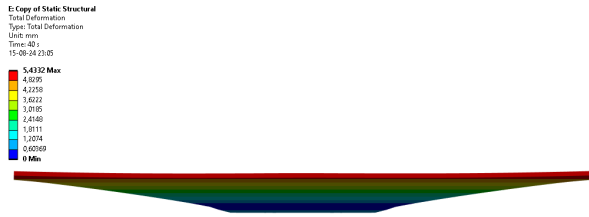


Figure 4.21: Displacement for Bonded-Bonded contacts without considering large deflection.

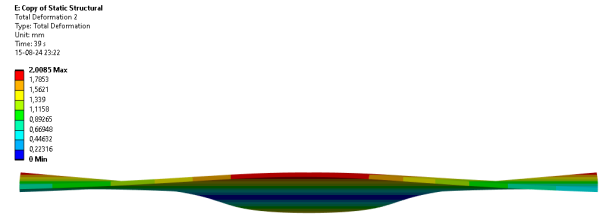


Figure 4.22: Displacement for Friction-Friction contacts, considering large deflections.

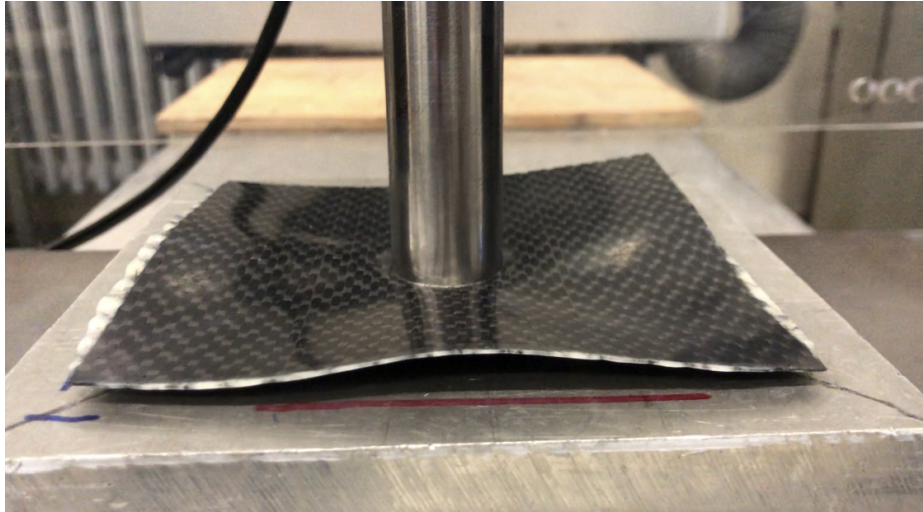


Figure 4.23: Buckling phenomenon observed during an experimental test of samples 7.

4.2.2 Analysis of the number of solution steps

Initially, the number of solution steps for contact calibration was set to 40 to facilitate solution convergence while providing a sufficient amount of data for the force-displacement curve. However, this number may have been overestimated for sample 7. As shown in Table 2, by reducing the number of steps by 11, the relative error in displacement is only 1.48%, and the stress error is 0.34%, with a total simulation time that is 7.21 times shorter. This suggests that the number of solution steps could be significantly reduced without compromising the accuracy of the results. However, since the primary objective of the simulations modeled in this chapter is to determine the FPF based on non-linear force-displacement curves, it is essential that the number of steps is not too low to ensure a clear representation of the experiment and to determine precisely determine the force at which the FPF occurs. Moreover, as explained in Section 4.1.4, a buckling phenomenon occurs at the end of the loading, requiring a maximum number of calculation points to achieve a reliable representation. In summary, the number of solution steps should be adjusted according to the sample being tested to ensure solution convergence and accurate results representation while avoiding excessively high computational costs.

	5 solution steps	55 solution steps
Maximum Von Mises stress [MPa]	679.73	677.43
Maximum displacement [mm]	2.0545	2.0853
Computation time [s]	357	2577

Table 4.3: Comparison of the results obtained by varying the number of solution steps in a simulation with frictional contacts. All other simulation parameters are identical to those presented in Section 4.2.1. Von Mises stresses are used as an equivalent stress for comparison.

	Central area [mm]	Intermediate area [mm]	Outer area [mm]	Number of elements [-]
Finest mesh	0.5	2	2	18944
Ideal mesh	1	2	2	8060
Roughest mesh	6	24	24	466

Table 4.4: Representation of various mesh configurations used in the convergence study.

4.2.3 Mesh convergence analysis

With the contact calibration now complete, the next step is to verify the validity of the results through a mesh convergence analysis, which is a critical phase in finite element studies. The principle behind this analysis is to progressively increase the number of finite elements in the mesh until the results become independent of further mesh refinement. This ensures that the simulation accurately represents the physical behavior of the system, free from numerical errors introduced by insufficient mesh density. Using the advanced meshing technique described in Section 4.1.2, several configurations were defined to progressively reduce the element size in each zone, thereby increasing the total number of elements within the plate. The geometry of the support has been modified since Section 4.1.2, necessitating the definition of a new zone corresponding to the fillet. During the contact calibration, it was observed that the element size of the support and load applicator had a negligible impact on the results but a significant effect on convergence. Specifically, the higher the number of elements in the fillet area, the easier the convergence. Consequently, for both the mesh convergence analysis and the remainder of the simulations, the element size for the support will be set to 1 [mm] in the fillet zone and 4 [mm] in the intermediate and outer zones. The cylinder, on the other hand, will be meshed with 2 [mm] elements.

Figure 4.26 illustrates the variation in maximum displacement as the number of elements is increased. As observed, after initially diverging, the displacement begins to converge once the mesh reaches 6366 elements. However, Figure 4.27 shows that even with a drastic increase in the number of elements, the stress values do not exhibit convergence. Drawing inspiration from a similar situation observed in [62], it was decided to analyze the variation of stress along the median of the plate. This path, illustrated in Figure 4.29, shows the values of Von Mises stress on the upper surface of the bottom ply, with the aim of examining the stress in areas that are distant from potential direct disturbances caused by the various contact points. As can be observed, this maximum value still occurs near the contact point between the plate and the support. As it can be noticed in Figure 4.28, starting from 1390 elements, the stress appears to converge at all points except for those located at 37.5 and 62.5 [mm]. These distances correspond precisely to the contact points between the sample and the outer edge of the cylinder used as load applicator. Thus, one can easily establish a cause-and-effect relationship between the lack of mesh convergence for stress values and the contact occurring between the two components. The most obvious solution to solve this issue is to further reduce the element size in this contact zone. However, even with a size of 0.25 [mm], the same phenomenon persisted. It is therefore challenging to determine whether this divergence is purely numerical and could be resolved with extremely small elements, or if it is inherently tied to the complexity of the model itself and the resulting nonlinearities, suggesting that a complete resolution may be practically unattainable. The computational power of the computer used in this work does not allow for simulations with very large finite element meshes, as this would result in calculation times exceeding four hours per

simulation, which would not be practical for the research conducted in this study, nor for application in the testing strategy of Formula Electric Belgium. Another solution could be to define a custom contact or material model in Ansys to resolve this divergence, but this option seems overly ambitious for a master's thesis, given the complexity and time constraints involved. Given that, apart from this point of divergence, the stress values appear consistent, the displacement converges, and the force-displacement curve aligns well with the experimental data, it has been decided to use the optimal mesh configuration presented in Table 4.4 for the remainder of this work. This approach ensures results with acceptable reliability while keeping the computational time within a reasonable range.

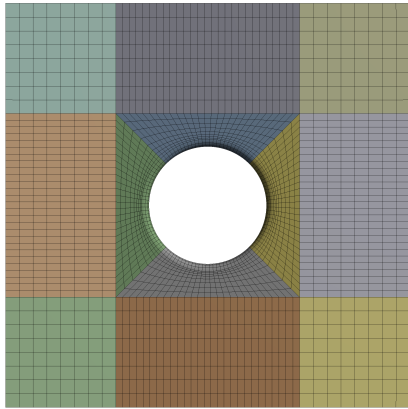


Figure 4.24: New mesh of the support.

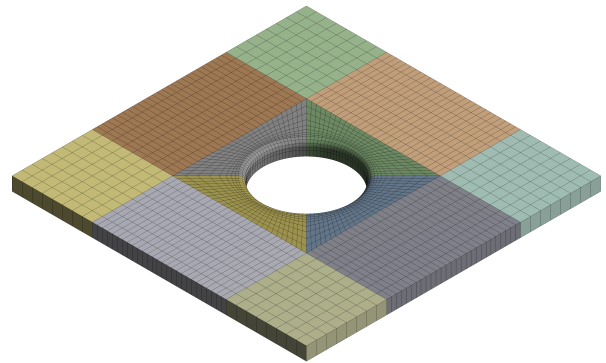


Figure 4.25: Isometric view of the new mesh.

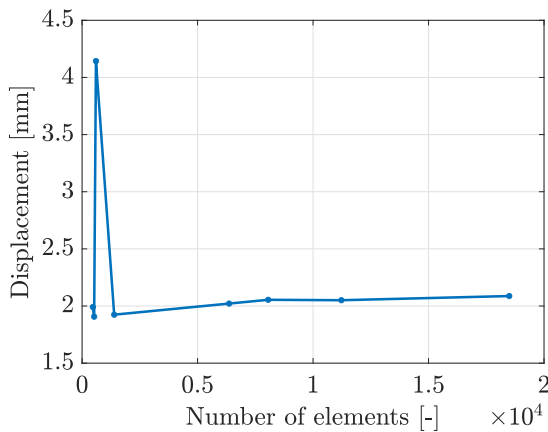


Figure 4.26: Maximum displacement as a function of the number of elements.

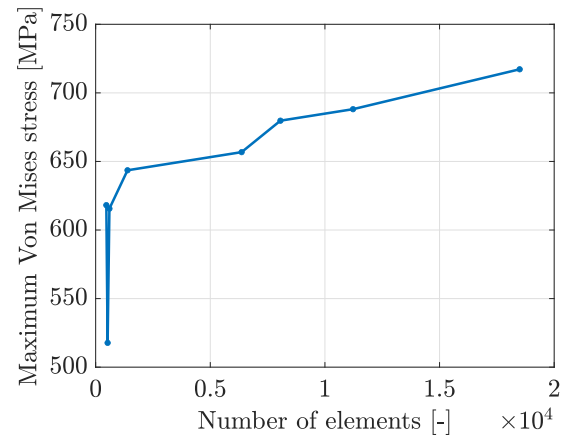


Figure 4.27: Maximum Von Mises stress as a function of the number of elements.

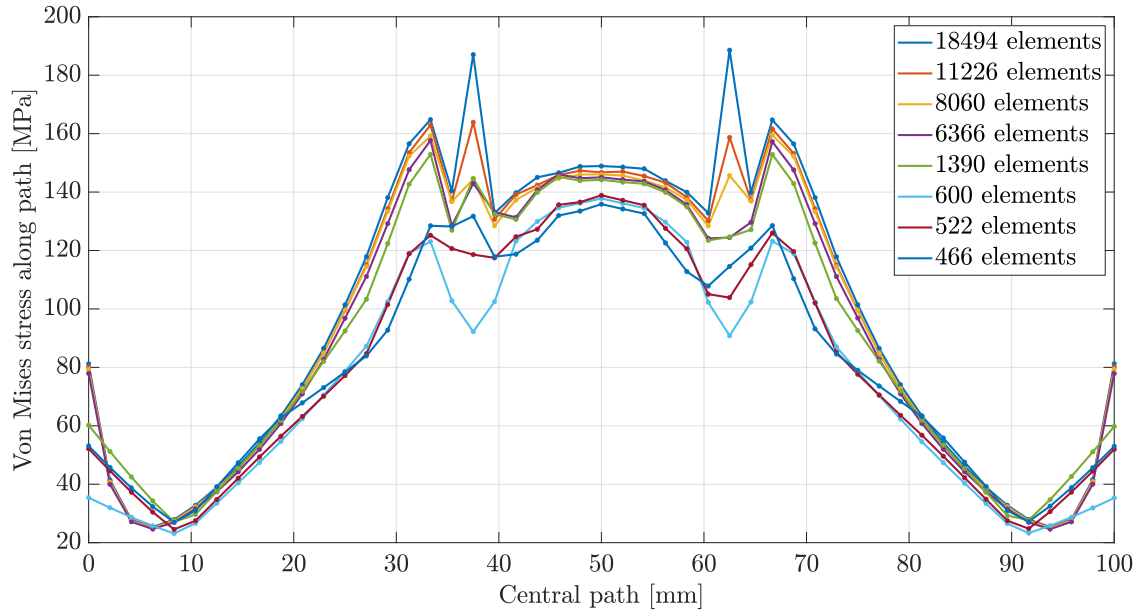


Figure 4.28: Variation of the Von Mises stress along the path.

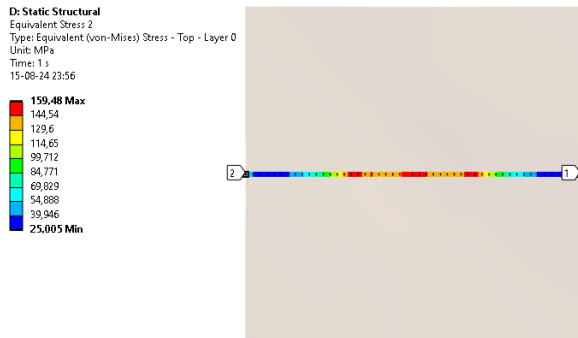


Figure 4.29: Path corresponding to the median of the plate.

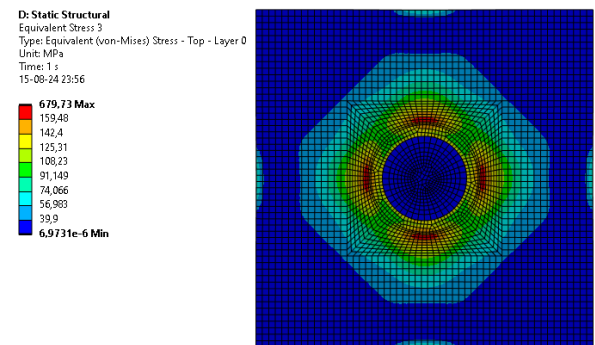


Figure 4.30: Von Mises stress in the ply from which the path was extracted.

4.3 Damage parameters calibration

Thanks to the previous sections of this chapter, it is now possible to simulate the perimeter shear test on composite material samples and generate a curve representing the evolution of the applied force as a function of displacement. However, this curve only illustrates the behavior of the plate during loading and does not indicate when failure occurs. Initially, the goal set by Formula Electric Belgium was to use the developed simulations to determine the FPF using the failure criteria implemented in ACP. This objective is based on experimental observations that have shown a correlation: the lower the force corresponding to the first ply failure, the smaller the peak force observed at the final failure of the sample. However, as explained in the Section 2.3.3, it is possible to model damages for composites using failure criteria and damages parameters. This approach would make the failure directly observable on the force-displacement curve, just like in the experimental test, and would

result in a more realistic material model. Hence, the aim of this section is to calibrate the damage model for composites in Ansys to determine if the conclusions drawn from the simulation results are consistent with the experimental findings. To achieve this, twelve samples divided into four different configurations, with three identical samples for each configuration, named 'Samples 8a', 'Samples 8b', 'Samples 8c' and 'Samples 8d' were fabricated and tested to compare the experimental and numerical results. These samples were produced using vacuum bagging and an autoclave as explained in the Section 3.1.2 to avoid manufacturing defects. For the woven plies, HexPly 8852 prepreg was used, while for the unidirectional plies, it was HexPly 813 prepreg. With these different configurations, various lay-up sequences will be tested to determine whether the conclusions drawn from the simulations are consistent with those from the experiments. This will help assess whether the numerical model of the shear test can replace certain experimental steps in the monocoque design procedure. The Table 4.6 shows the different lay-up designed for the calibration. They are based on the design rules established in the Section 2.3.1 and are designed to study the influence of 45 [°] plies in a composite lay-up subjected to the perimeter shear test. In this way, it can be observed that the quantity and placement of plies at this orientation vary depending on the configuration. The samples 8d aim to determine the effect of replacing woven layers with UD layers.

	HexPly 8852	HexPly 813
Density [kg/m ³]	1570	1610
E_x [GPa]	64	134
E_y [GPa]	64	10
E_z [GPa]	10	10
X_t [MPa]	911.95*	2622*
Y_t [MPa]	911.95*	81
Z_t [MPa]	80	81
X_c [MPa]	-1015.5*	-1760.7*
Y_c [MPa]	-1015.5*	-200
Z_c [MPa]	-200	-200
Ply type	Plain weave	Unidirectional

Table 4.5: Main mechanical properties of selected materials. The data are exported from ESAComp and Hexcel datasheets [63]. The data with * correspond to values corrected from experiments.

4.3.1 Calibration process

When simulating damage in Ansys, the first step is to determine the criterion that will initiate the damage. In the standard composite material model available, various failure criteria are offered, but in our case, only the maximum stress criterion is relevant. Therefore, it will be used to initiate the failure of both the fibers and the matrix under tension, compression and shear. Next, the damage evolution law and the resulting damage variables must be determined. Due to its complexity, the 'Continuum damage mechanics' method will not be used. Instead, the 'Material property degradation method' is preferred. However, the various values for the damage variables presented in Table 4.7 are

	Lay-up	Thickness [mm]
Samples 8a	[0F/45F/0F/0F/45F/0F]	1.17
Samples 8b	[0F/45F/45F/45F/45F/0F]	1.17
Samples 8c	[45F/45F/0F/0F/45F/45F]	1.17
Samples 8d	[0F/+45/-45/-45/+45/0F]	0.91

Table 4.6: Lay-up and thickness of the samples 8 produced and used for simulations.

	HexPly 8852	HexPly 813
d_{ft} [-]	0.8	0.5
d_{fc} [-]	0.8	0.55
d_{mt} [-]	0.8	0.6
d_{mc} [-]	0.8	0.65

Table 4.7: Damage variables for woven and unidirectional CFRP plies.

not straightforward to obtain. Despite a thorough review of the scientific literature, only values for unidirectional plies were found. Therefore, the damage variables for woven plies are based on the recommendations of [64] in order to significantly represent the effect of damages by a loss of 80% of the stiffness of the damaged finite element. Although it is not ideal, these values are still considered reliable for the initial estimation of damage in composite modeling. The material damages modeling also has an impact on the computational cost of the simulations, as the material properties are now considered nonlinear and therefore require multiple solution iterations. Moreover, it has been rapidly observed during the first simulation attempts that when the damage variable values exceed 0.75, the simulation solution begins to fail to converge as soon as the material starts to fracture. When damages are taken into account, the solver automatically sets the minimum number of substeps to 3 to facilitate the convergence. Following this setting, and based on the findings from Section 4.2.2, the number of solution steps was preventively set to 20. This results in a total of 60 steps, since each solution step is divided into 3 substeps. In the case of sample 8d which is partially composed of UD plies, this approach allows for simulating a significant portion of the fracture before the solution starts to diverge. However, for the other samples, the solution continues to diverge as soon as the FPF is exceeded. Even by increasing the number of substeps in the final solution step to 30, no convergence was achieved. Consequently, for the first three samples, it was decided that the applied displacement would stop at the last converged solution step, which is the step following the FPF. While this approach ensures that the simulations converge in all cases, it also means that they will not allow for determining the peak force reached just before the complete failure of the sample. The force value corresponding to the FPF will thus serve as an initial estimate to assess the sample's resistance in the shear test. This allows for comparing different potential lay-up designs through simulations.

Figure 4.31 illustrates the discussion of the previous paragraph. The result presented is a simulation of sample 8c, and it is immediately noticeable that the obtained curves closely follows the experimental curves, which is a particularly encouraging outcome. However, the FPF of the 'Numerical-1' curve occurs at a significantly lower force value compared to the experimental results. The FPF is intrinsically linked to the material strength values listed in Table 4.5, and it can be adjusted by

calibrating these values based on experimental results. The goal is to use various samples made from the same material, each with a different lay-up, to ensure that the newly calibrated values result in a valid FPF for each configuration. This approach may seem biased, but it has been used by [62], and as [64] points out, it is crucial to understand that the values listed in composite material datasheets do not always reflect real-world conditions. As discussed in previous sections, the properties of composite materials are highly dependent on their manufacturing process. Therefore, even if two different applications use the same material, their properties may not precisely match the nominal values provided in the datasheet. Following this calibration, it was found that increasing the tensile and compressive strength values by 15% resulted in the numerical FPF occurring within the range of the experimental FPF for each case. The 'Numerical-2' curve shows thus that its FPF is similar to the experimental results in terms of both displacement and force. For woven fibers, this adjustment should be applied in both the x and y directions, while for UD fibers, only the strength values in the x direction need to be modified as seen in Table 4.5.

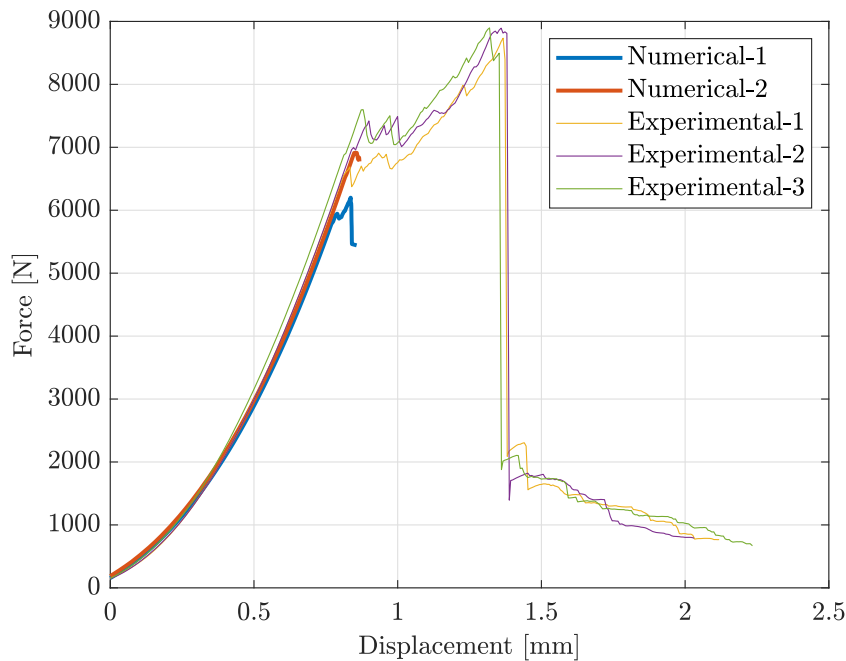


Figure 4.31: Force-displacement curves for different types of simulations compared with experimental curves for samples 8c. Displacement are normalized.

It is evident that modeling failure in composites is a complex issue that requires extensive research and experimentation to achieve a high level of reliability [33]. However, in recent years, significant research has been conducted in the field of modeling failure in composites subjected to impacts. Material models such as MAT54/55 can produce highly reliable results that represent near-complete failure of the composite [30, 65, 66]. Nonetheless, this type of model is compatible only with LS-DYNA, a software for high-speed dynamic simulations, which would not be suitable for our study of the perimeter shear test.

4.3.2 Analysis of the results

Now that the damage representations align with the experimental results, one can proceed to analyze the various curves and data in detail. Figures 4.32, 4.33, 4.34 and 4.35 show comparisons between the force-displacement curves obtained from experimental measures and the numerical results. It can be clearly observed that in each case, the numerical curve follows almost perfectly the experimental ones. It also appears that the highest peak force is achieved with samples 8c, demonstrating that the shear test resistance of a sample can be improved by placing fiber layers oriented at 45° on the outermost layers of the lay-up. Samples 8a seem to perform better than samples 8b. Additionally, samples 8d show the lowest resistance, indicating that reducing the number of woven plies in the lay-up decreases the peak force. The hypothesis formulated by Formula Electric Belgium regarding the relationship between the FPF and the peak force seems to hold true experimentally. Indeed, in the majority of cases, it can be observed that the higher the force at which the FPF occurs, the higher the peak force at the final rupture. However, a major drawback is that the numerical FPFs shown in Figures 4.32, 4.33 and 4.34 do not appear to have a high degree of accuracy. Specifically, when looking at Figure 4.34, the experimental first ply failure occurs on average around 7000 [N], while in the other figures, it is much lower. Additionally, the numerical FPF for samples 8c are lower than that of samples 8a and 8b. This indicates that for nearly similar lay-ups, the numerical model does not allow for reliable conclusions about the tested samples. But, when comparing the first three samples with the last one, it is clear that the simulation also shows that sample 8d is the least resistant to the shear test. Thus, the use of simulations in the composite testing strategy should be limited to comparing lay-ups with a minimum level of difference between them, which still represents progress over the current strategy.

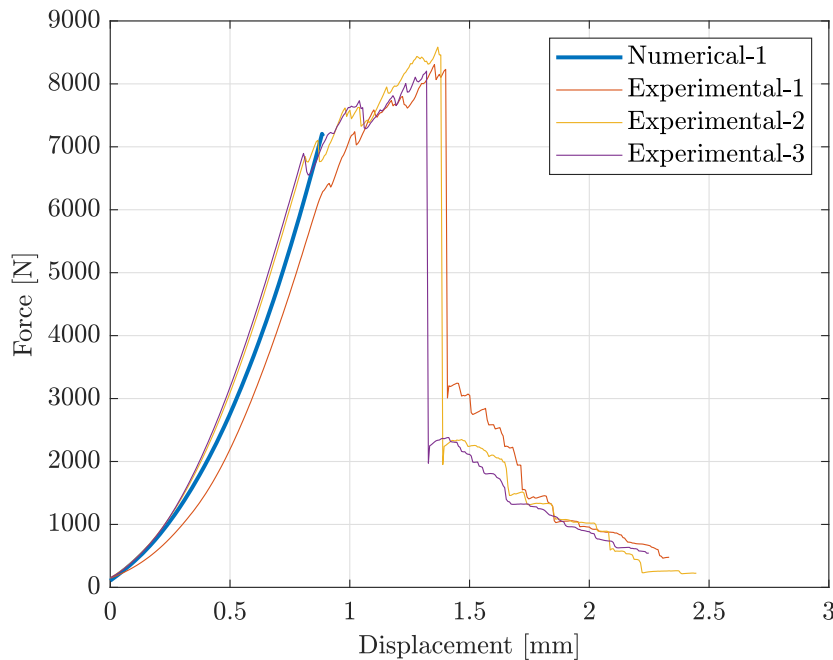


Figure 4.32: Force-displacement curves for different types of simulations compared with experimental curves for samples 8a. Displacement are normalized.

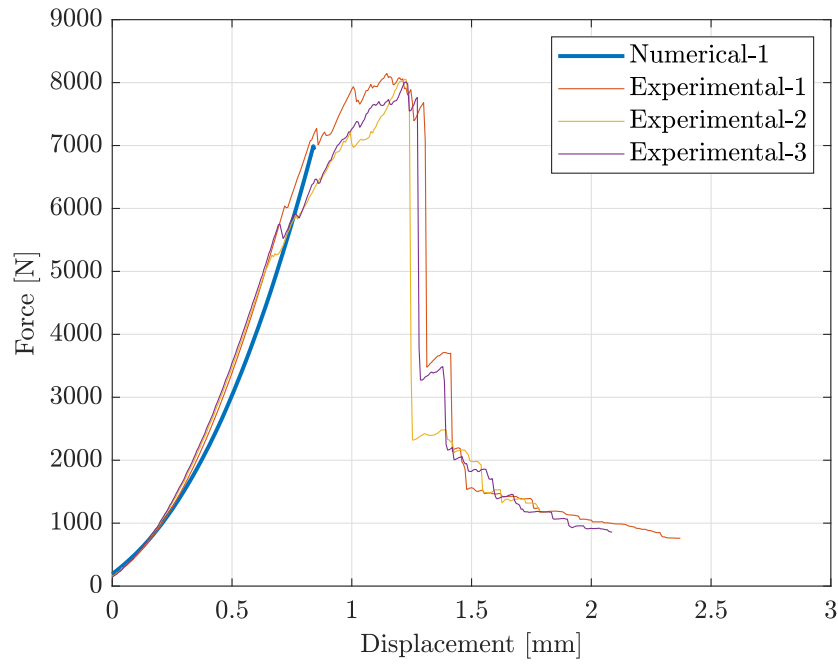


Figure 4.33: Force-displacement curves comparing the simulation results with experimental data for samples 8b. The displacements are normalized.

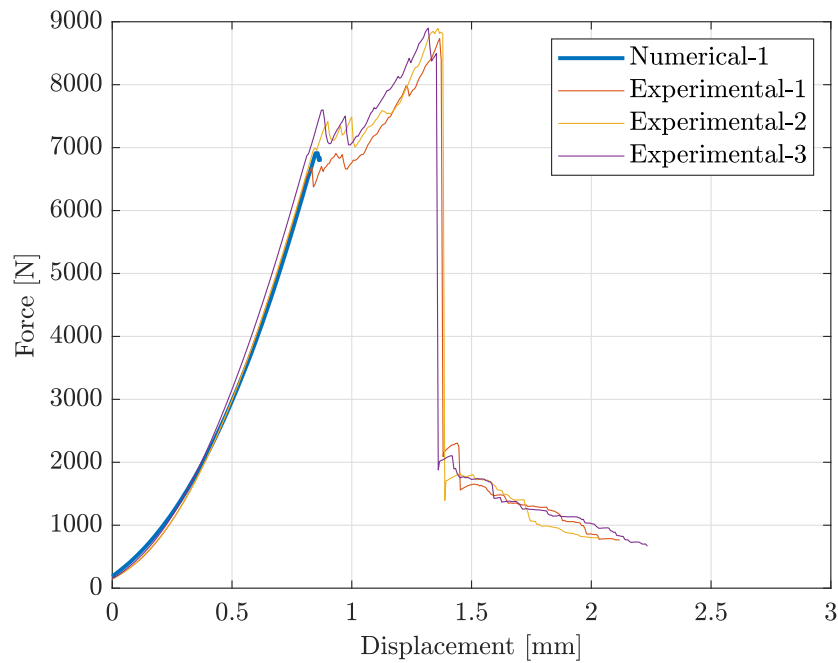


Figure 4.34: Force-displacement curves comparing the simulation results with experimental data for samples 8c. The displacements are normalized.

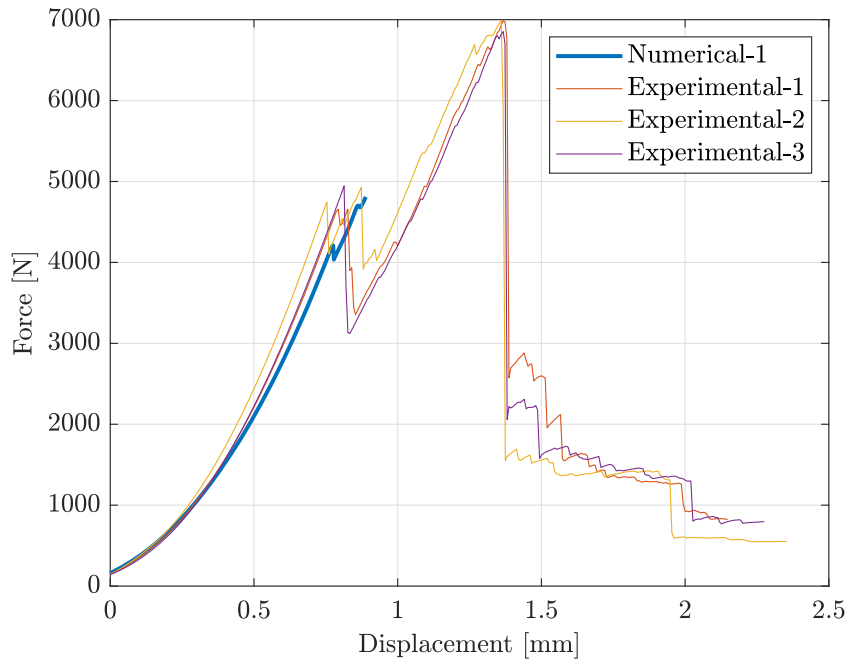


Figure 4.35: Force-displacement curves comparing the simulation results with experimental data for samples 8d. The displacements are normalized.

In addition to representing force-displacement curves, the modeling of the perimeter shear test also allows for the visualization of stress distribution within the sample subjected to the test. As shown in the following figures, the displacement, Von Mises stress, and inverse reserve factor are symmetrical in all cases. This symmetry is logical, given that the applied displacement and the lay-up configuration are also symmetrical. This symmetry in the results indicates that the loading conditions and material properties have been applied consistently with respect to the sample's geometry. Thus, the analysis confirms the validity of the modeling while providing valuable insights into the internal stress distribution, which is essential for anticipating critical areas in the sample where failures may occur. The results presented correspond to the solution step that exactly matches the FPF. Figures 4.36 to 4.43 show that, depending on the lay-up, the deformation mode varies. Figures 4.44 to 4.51 illustrate that the maximum stress is reached in each case on the upper outer layer, above the contact area between the support and the sample. It can be observed that the regions where the stress is highest correspond to the orientation of the fibers in the upper outer layer. For the lower face of the samples, the stresses are maximal in the area corresponding to the contact between the load applicator and the upper surface of the sample. Figure 4.52 shows that the stresses are maximal in the outer layers of the lay-up. Figures 4.53 to 4.56 allow for the comparison of failure criteria. Thus, it is noted that the maximum stress theory appears more optimistic than the Tsai-Wu failure criterion. In both cases, failure occurs in the regions where the stress is maximal. For the lower layer, this area can be easily compared to the failure observed experimentally in Figure 4.64, while for the upper layer, this failure appears in an area with a slightly larger diameter than that of the cylinder imposing the displacement. Figure 4.63 also shows fiber failure in this area. However, based on experimental observations, one might expect the FPF of the upper layer to also occur in the contact area with the load applicator. This difference between numerical and experimental results can be explained by the contact modeling, which could be improved to increase the accuracy of the simulation results.

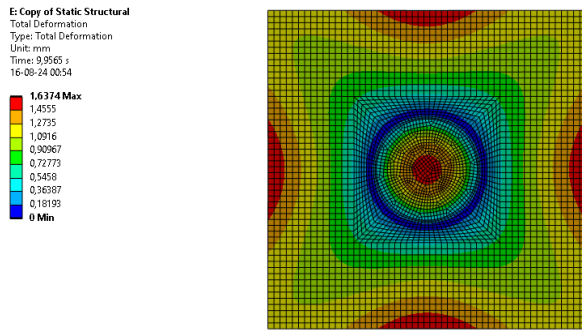


Figure 4.36: Displacement. Top view of sample 8a.

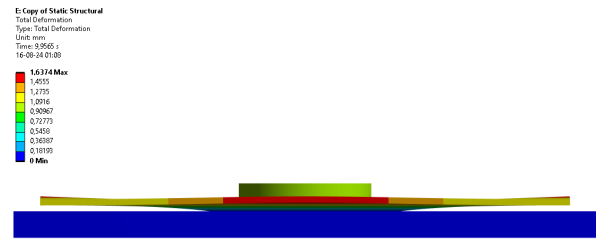


Figure 4.37: Displacement. Side view of sample 8a.

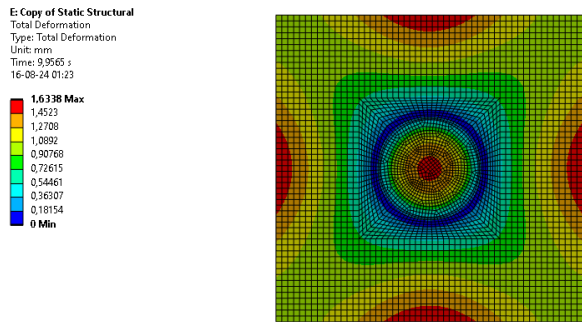


Figure 4.38: Displacement. Top view of sample 8b.

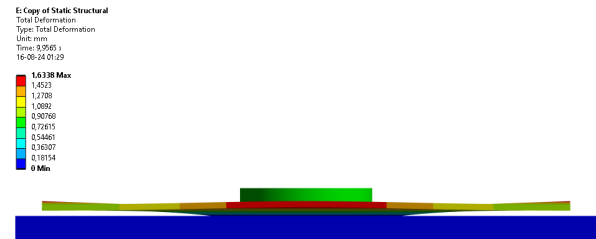


Figure 4.39: Displacement. Side view of sample 8b.

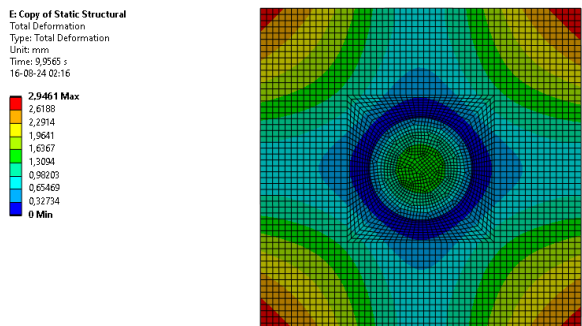


Figure 4.40: Displacement. Top view of sample 8c.

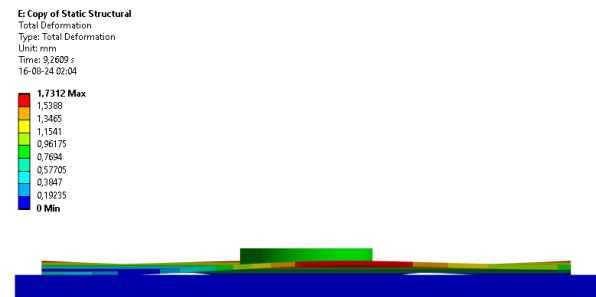


Figure 4.41: Displacement. Side view of sample 8c.

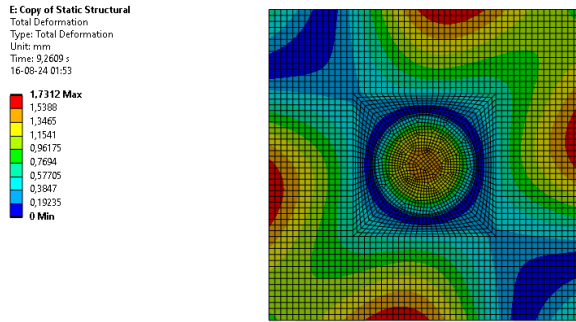


Figure 4.42: Displacement. Top view of sample 8d.

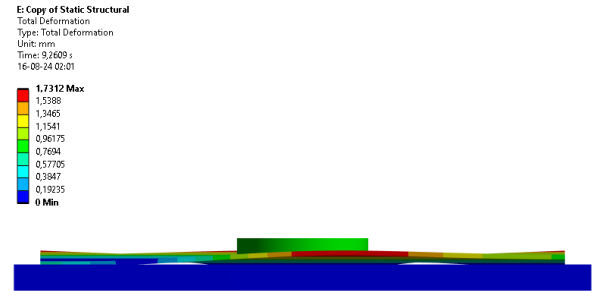


Figure 4.43: Displacement. Side view of sample 8d.

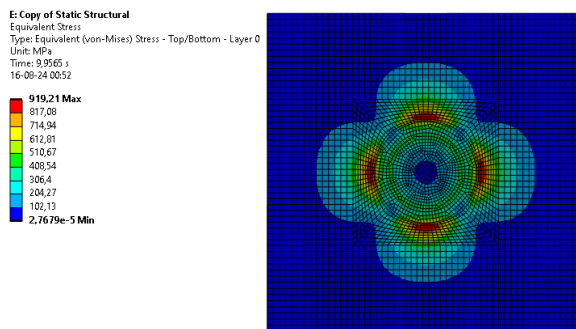


Figure 4.44: Von Mises stress. Top view of sample 8a.

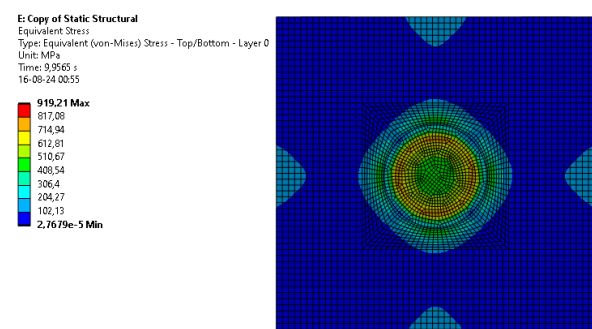


Figure 4.45: Von Mises stress. Bottom view of sample 8b.

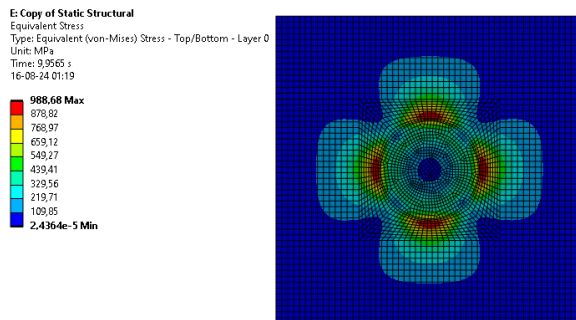


Figure 4.46: Von Mises stress. Top view of sample 8b.

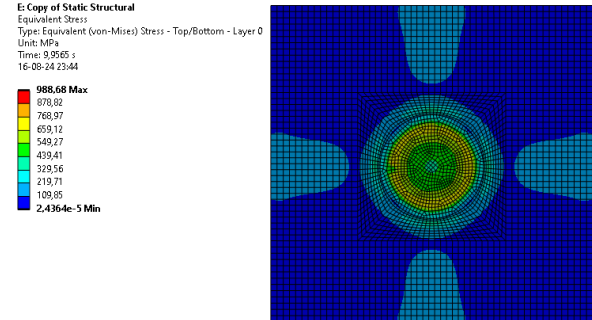


Figure 4.47: Von Mises stress. Bottom view of sample 8b.

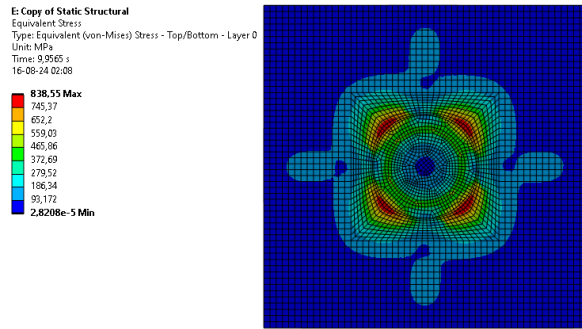


Figure 4.48: Von Mises stress. Top view of sample 8c.

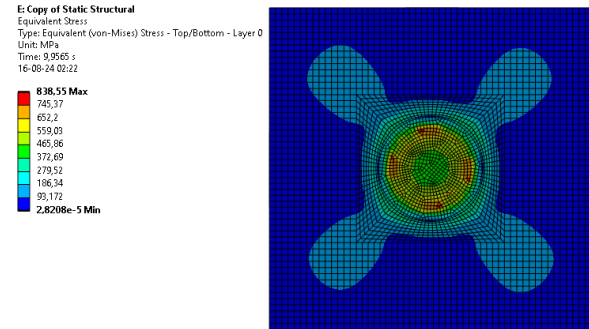


Figure 4.49: Von Mises stress. Bottom view of sample 8c.

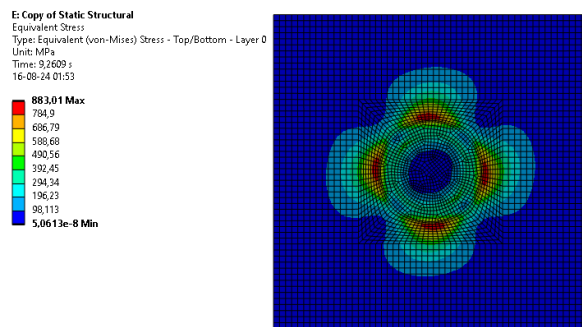


Figure 4.50: Von Mises stress. Top view of sample 8d.

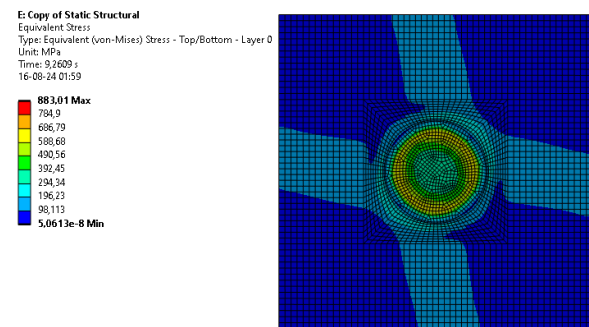


Figure 4.51: Von Mises stress. Bottom view of sample 8d.

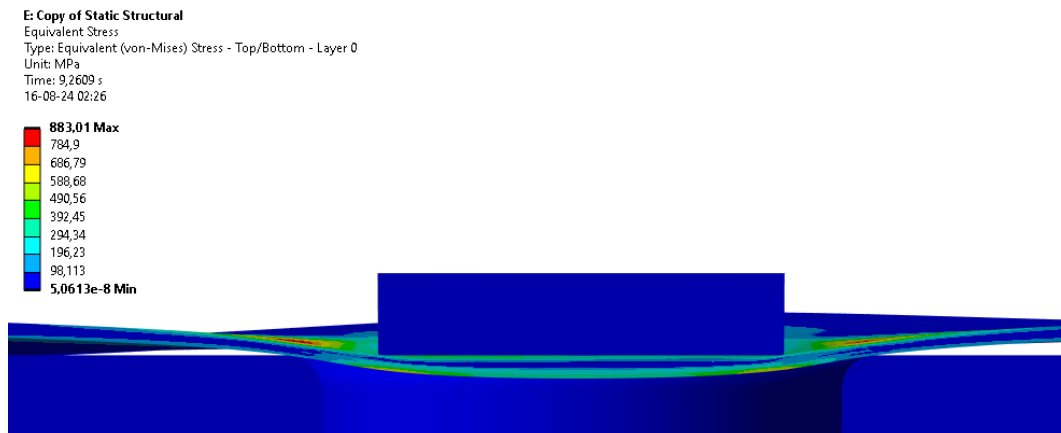


Figure 4.52: Von Mises stress. Cross-sectional view of sample 8c

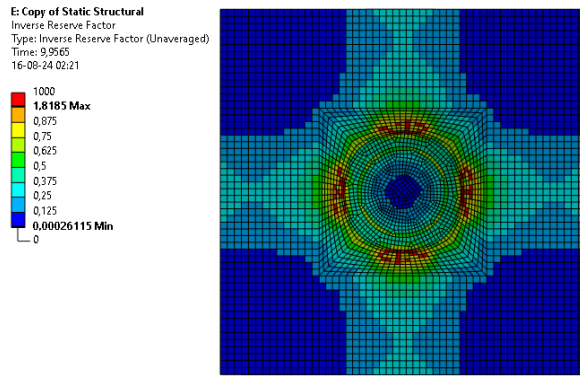


Figure 4.53: Max stress criterion inverse reserve factor. Top view of sample 8c.

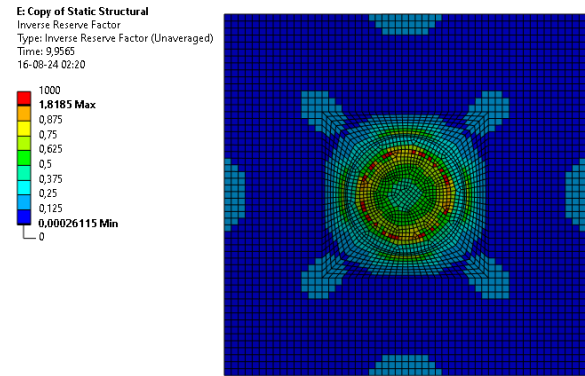


Figure 4.54: Max stress criterion inverse reserve factor. Bottom view of sample 8c.

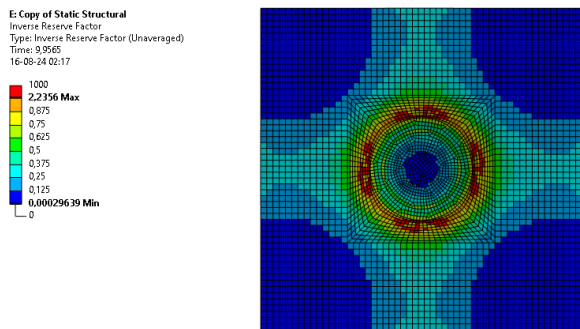


Figure 4.55: Tsai-Wu criterion inverse reserve factor. Top view of sample 8c.

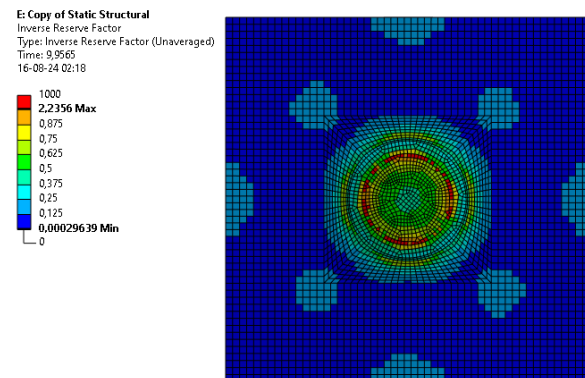


Figure 4.56: Tsai-Wu criterion inverse reserve factor. Bottom view of sample 8c.

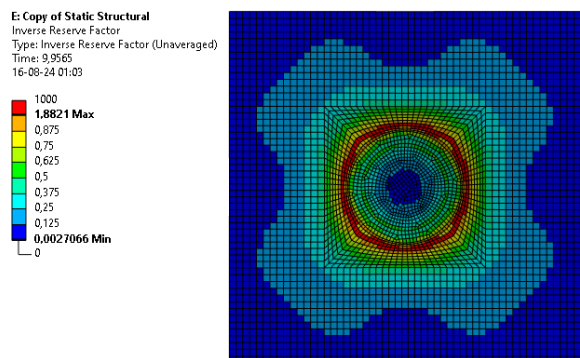


Figure 4.57: Tsai-Wu criterion inverse reserve factor. Top view of sample 8a.

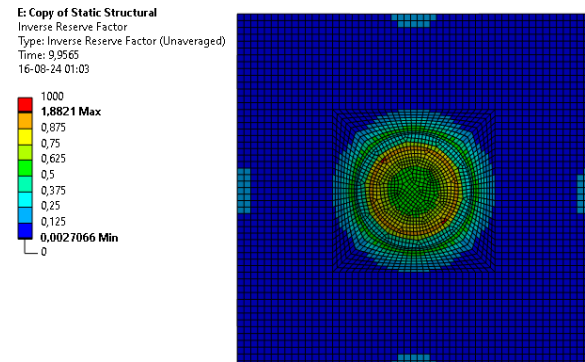


Figure 4.58: Tsai-Wu criterion inverse reserve factor. Bottom view of sample 8a.

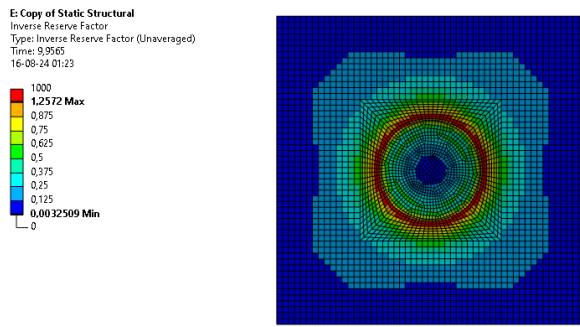


Figure 4.59: Tsai-Wu criterion inverse re-serve factor. Top view of sample 8b.

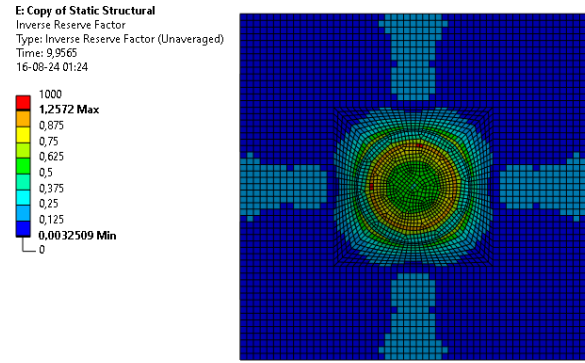


Figure 4.60: Tsai-Wu criterion inverse re-serve factor. Bottom view of sample 8b.

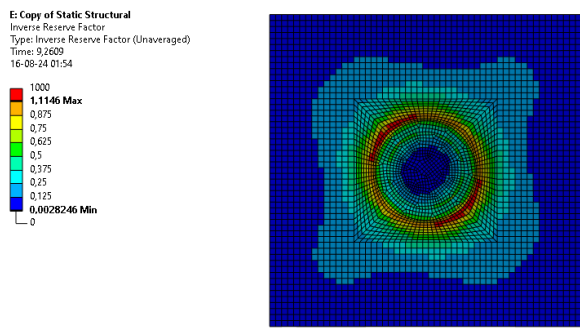


Figure 4.61: Tsai-Wu criterion inverse re-serve factor. Top view of sample 8d.

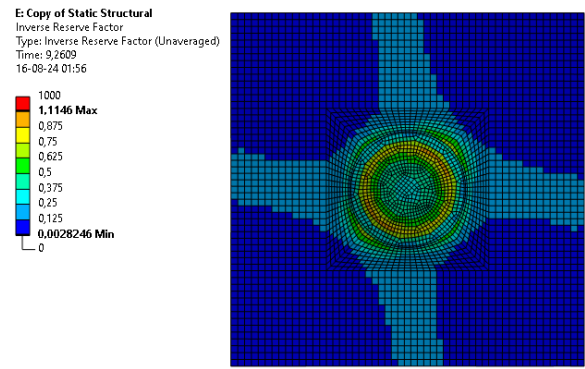


Figure 4.62: Tsai-Wu criterion inverse re-serve factor. Bottom view of sample 8d.

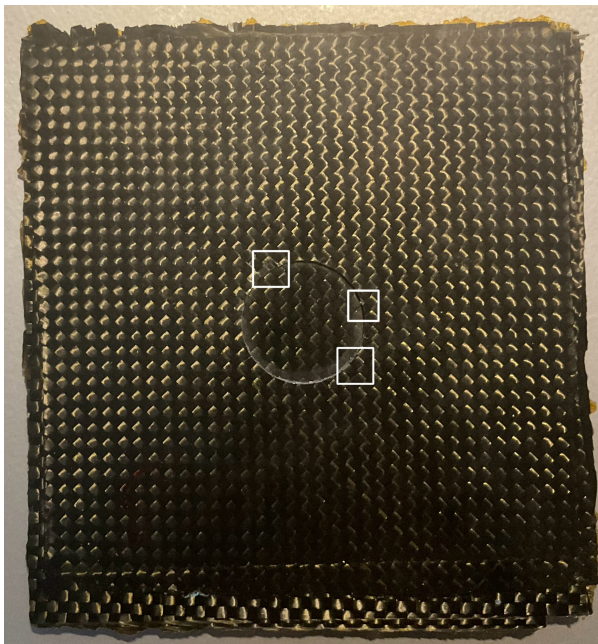


Figure 4.63: Top view of the sample 8c.

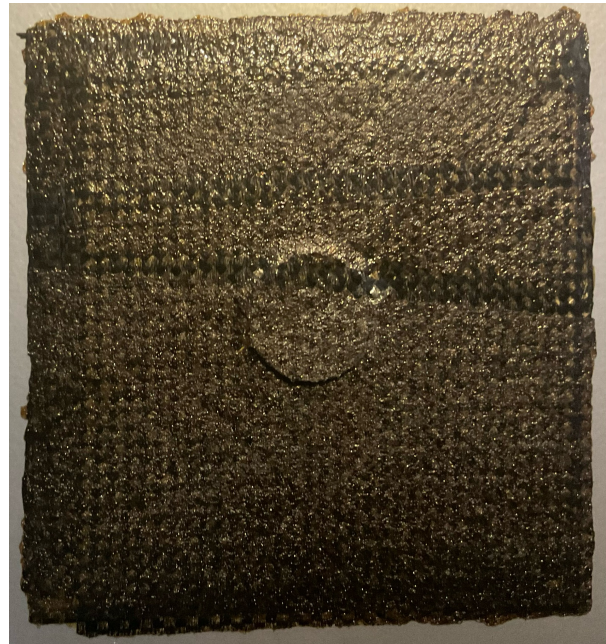


Figure 4.64: Bottom view of the sample 8c.

4.4 Flax fiber parameters calibration

Unlike carbon fiber, numerical simulations using flax fiber are relatively rare. This trend can be easily explained, as the use of natural fibers in industrial applications is a relatively recent development. Moreover, as discussed in Chapters 2 and 3, the mechanical properties of flax fiber vary depending on its quality, and the manufacturing processes that utilize flax fiber as a base material for composites have not yet reached the same level of industrial maturity as those for carbon fiber. As a result, it is uncommon to find comprehensive datasheets, and there is no established database like ESAComp for synthetic fibers. As explained in Chapter 3, the other consequence of this low industrial maturity is the challenge of finding a supplier that offers high-quality flax fiber prepregs compatible with carbon fiber prepregs. The use of dry fiber was thus necessitated by this constraint, further complicating the acquisition of reliable data for numerical simulations. Indeed, with vacuum infusion, it is impossible to precisely control the amount of resin absorbed by the fibers. The properties of the resin used also vary depending on the product, which makes it challenging to estimate the mechanical properties accurately. Furthermore, at this stage of the work, it would be far too time-consuming to consider a testing campaign to determine all the necessary properties for simulations in Ansys. Given the lack of alternative options, it was decided to use properties derived from studies [22, 23, 65, 66] involving flax fiber prepregs, as the fibers themselves are comparable to those used in the manufacturing of the samples 6 thus allowing to use them as experimental references. Since these articles consistently concluded that their simulations were realistic, they provide a solid foundation for our study. However, one must maintain a critical perspective on our results and consider that the simulations are primarily intended to provide an initial understanding of the behavior of flax fiber and to verify whether the numerical model previously developed for carbon fiber is also applicable to flax. The characteristics of the fibers and of the samples are shown in Tables 4.8 and 4.9.

	Flax 350g	Flax 150g
Density [kg/m^3]	1290	1257
E_x [GPa]	10.3	8.702
E_y [GPa]	10.3	8.702
E_z [GPa]	4.298	4.298
X_t [MPa]	232.71	103
Y_t [MPa]	232.71	103
Z_t [MPa]	31	31
X_c [MPa]	-393.41	-60
Y_c [MPa]	-393.41	-60
Z_c [MPa]	-45	-45
Ply type	Twill 2x2	Twill 2x2

Table 4.8: Main mechanical properties of selected materials. The data are selected from different articles [22, 23, 65, 66].

	Lay-up	Thickness [mm]
Samples 6a	[0F /0F /0F /0F]	1.86
Samples 6b	[45F /0F /0F /45F]	1.86

Table 4.9: Lay-up and thickness of the samples 6 produced and used for simulations. The thickness is determined here by ACP.

	Flax 350g	Flax 150g
d_{ft} [-]	0.5	0.5
d_{fc} [-]	0.5	0.5
d_{mt} [-]	0.5	0.5
d_{mc} [-]	0.5	0.5

Table 4.10: Damage variables for woven FFRP plies.

4.4.1 Calibration process

For damage modeling, the same procedure as for carbon fiber will be followed. Firstly, the number of steps will also be set to 20. However, given the damage parameters, no large convergence issues were observed in this case, allowing the use of only three substeps for each solution step. Concerning the applied displacement, the value selected is arbitrary. The objective is to capture the post-first ply failure behavior and observing the progressive failure mechanisms that occur before total rupture. Although the simulation does not necessarily reach the final rupture point, it provides a useful approximation of advanced failure scenarios while allowing the simulation solution to converge, thus avoiding the issues encountered with samples 8. Regarding the damage parameters, the material property degradation method was also used, which required defining the parameters listed in Table 4.10. However, due to an even more pronounced lack of data for flax fibers, it was decided to use on the damage parameter for softening of fiber tensile strength after failure used in the MAT54 material model as starting value. From [23], this value is equal to 0.2. However, as it can be seen on the Figure 4.65, the curve 'Numerical-1', that corresponds to a solution that use this value for all the damage parameters, has a too steep slope and does not appear to fail even at large displacement imposed. It was therefore decided to increase the value of these parameters until the experimental curves align with the simulation results. By adopting this trial-and-error approach, the 'Numerical-2' curve was obtained, demonstrating a closer alignment with the experimental curves and a sample failure pattern that more closely resembles the experimental cases. This method, though somewhat iterative and observation-based, allowed for fine-tuning of the parameters until the numerical results matched the expected experimental behavior. The values of the parameters resulting of this method are shown in Table 4.10. The approach presented in this section might seem delicate due to the numerous approximations made. However, given the lack of data and prior research, it is the only viable solution available. Moreover, this approach is also employed in the sources used to parameterize our simulations [22, 23, 65, 66].

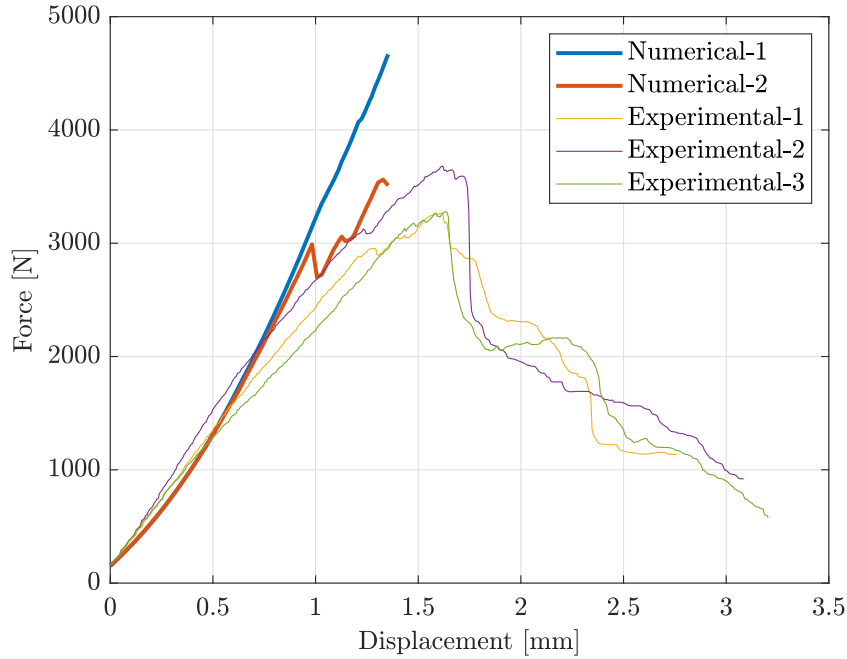


Figure 4.65: Force-displacement curves for different types of simulations compared with experimental curves for samples 6a. Displacement are normalized.

4.4.2 Analysis of the results

Despite all the estimations used, the simulation results shown in Figures 4.66 and 4.67 still exhibit a strong similarity to the experimental curves. These experimental curves generally show an almost linear evolution up to the point of failure, while the curves from the numerical simulations are slightly nonlinear, causing them to diverge from the experimental results after approximately 0.75 [mm]. While the failure of the carbon fiber samples was relatively sudden, here it can be observed that the peak force is reached shortly after the initial signs of failure but does not result in a significant drop in the applied force. Regarding failure in the simulations, one can see that despite these similarities to reality, it often appears too abrupt, with force decreasing too sharply. However, the simulations still manage to capture the high strain-to-failure characteristic of flax fiber, as evidenced by the displacements achieved at the point of FPF.

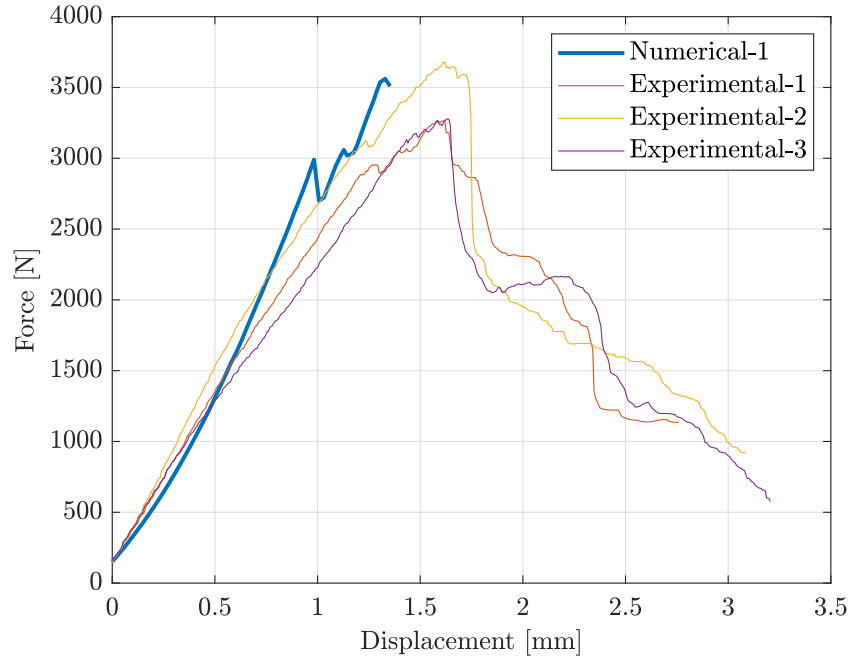


Figure 4.66: Force-displacement curves comparing the simulation results with experimental data for samples 6a. The displacements are normalized.

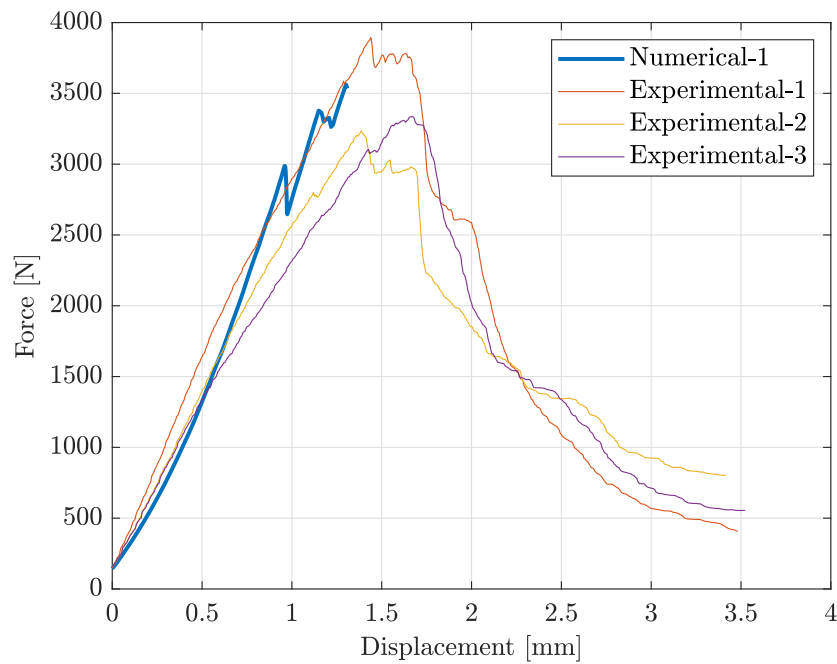


Figure 4.67: Force-displacement curves comparing the simulation results with experimental data for samples 6b. The displacements are normalized.

Regarding the results obtained in Ansys, similar observations to those made for carbon fiber can be noted. However, it is noticeable that, as expected, failure occurs at a much lower stress level. Due

to the greater thickness of the samples, Figures 4.68 to 4.71 show that the displacements reached are significantly smaller. When it comes to failure, it can be observed that it occurs over a larger area compared to carbon fiber, which seems to be more in line with the experimental results shown in Figures 4.81 and 4.82. Finally, it is worth highlighting that despite the FPF observed in a large number of elements, the force-displacement curves continue to increase thereafter, illustrating the superior toughness of flax fiber.

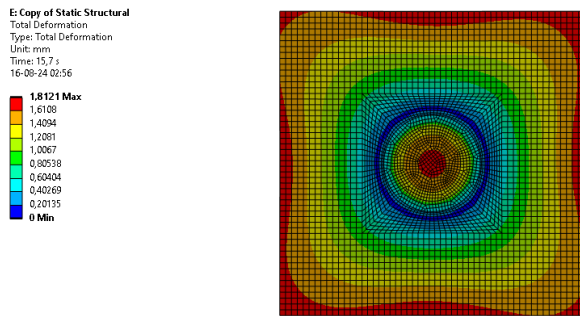


Figure 4.68: Displacement. Top view of sample 6a.

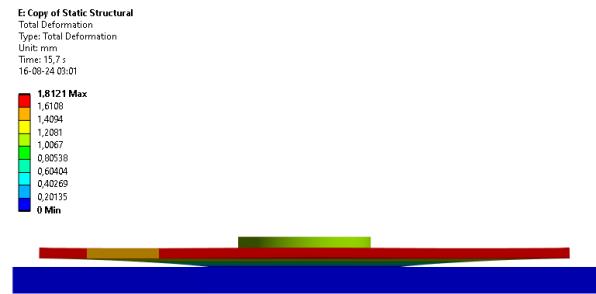


Figure 4.69: Displacement. Side view of sample 6a.

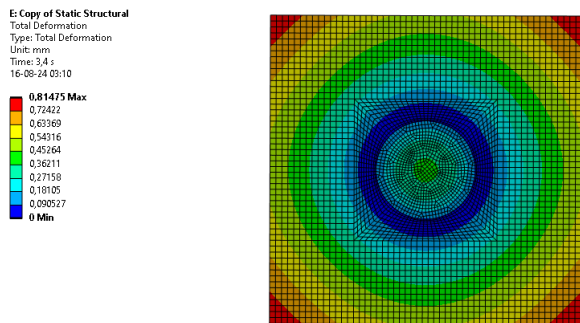


Figure 4.70: Displacement. Top view of sample 6b.

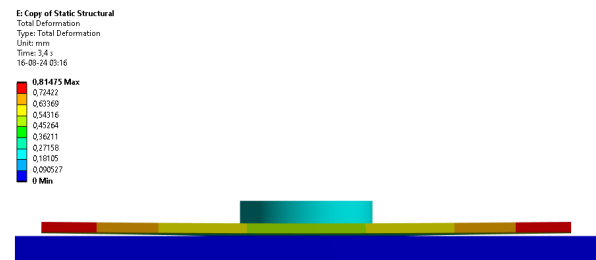


Figure 4.71: Displacement. Side view of sample 6b.

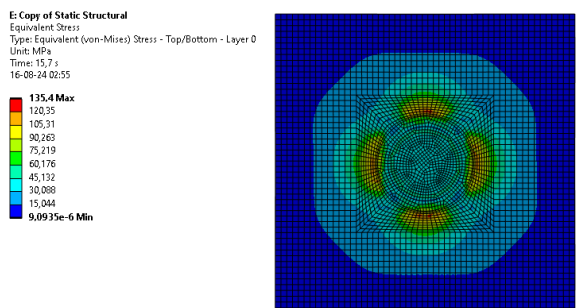


Figure 4.72: Von Mises stress. Top view of sample 6a.

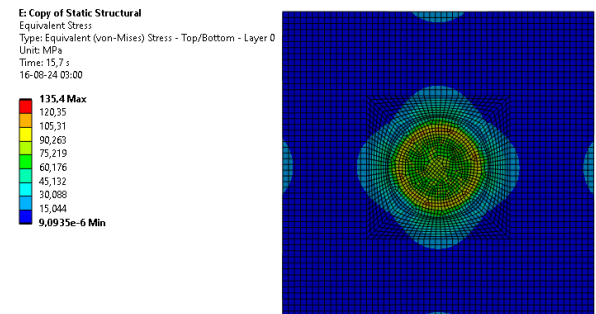


Figure 4.73: Von Mises stress. Bottom view of sample 6a.

E: Copy of Static Structural
Equivalent Stress
Type: Equivalent (von-Mises) Stress - Top/Bottom - Layer 0
Unit: MPa
Time: 14 s
16-08-24 03:09

133,2 Max
118,4
105,6
88,803
74,003
59,202
44,402
29,601
14,801
9,8187e-6 Min

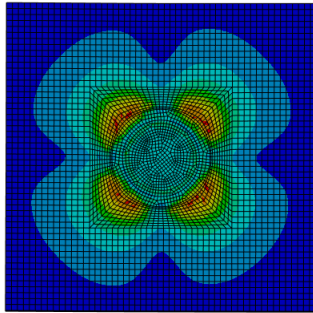


Figure 4.74: Von Mises stress. Top view of sample 6b.

E: Copy of Static Structural
Equivalent Stress
Type: Equivalent (von-Mises) Stress - Top/Bottom - Layer 0
Unit: MPa
Time: 14 s
16-08-24 03:15

133,2 Max
118,4
105,6
88,803
74,003
59,202
44,402
29,601
14,801
9,8187e-6 Min

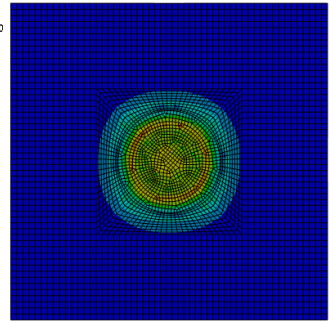


Figure 4.75: Von Mises stress. Bottom view of sample 6b.

E: Copy of Static Structural
Equivalent Stress
Type: Equivalent (von-Mises) Stress - Top/Bottom - Layer 0
Unit: MPa
Time: 15,7 s
16-08-24 03:05

135,4 Max
120,35
105,31
90,263
75,219
60,176
45,132
30,088
15,044
9,0935e-6 Min

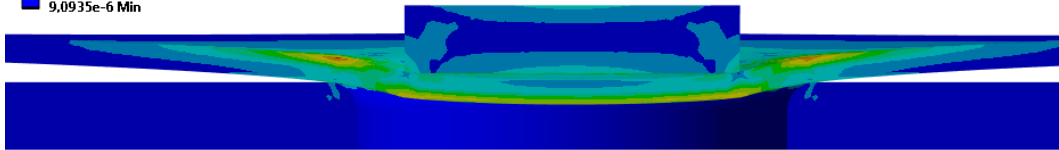


Figure 4.76: Von Mises stress. Cross-sectional view of sample 6a.

E: Copy of Static Structural
Inverse Reserve Factor
Type: Inverse Reserve Factor (Unaveraged)
Time: 15,7
16-08-24 02:56

1000
2,3378 Max
0,875
0,75
0,625
0,5
0,375
0,25
0,125
0,0012258 Min
0

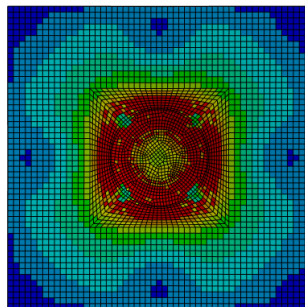


Figure 4.77: Tsai-Wu criterion inverse reserve factor. Top view of sample 6a.

E: Copy of Static Structural
Inverse Reserve Factor
Type: Inverse Reserve Factor (Unaveraged)
Time: 15,7
16-08-24 02:58

1000
2,3378 Max
0,875
0,75
0,625
0,5
0,375
0,25
0,125
0,0012258 Min
0

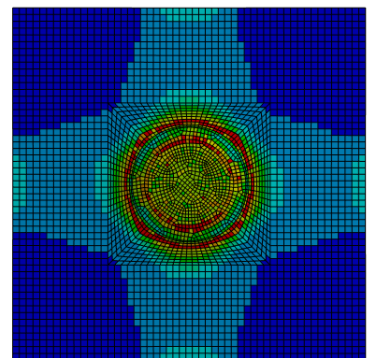


Figure 4.78: Tsai-Wu criterion inverse reserve factor. Bottom view of sample 6a.

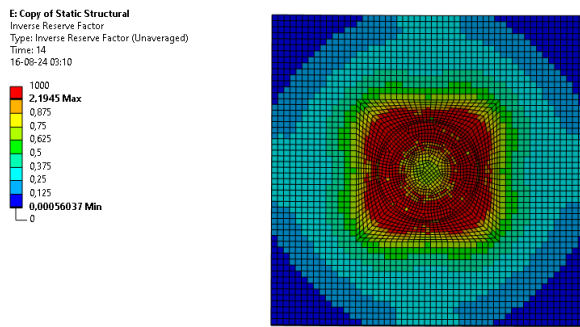


Figure 4.79: Tsai-Wu criterion inverse re-serve factor. Top view of sample 6b.

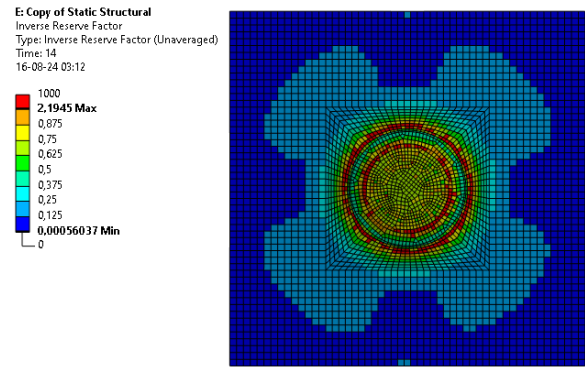


Figure 4.80: Tsai-Wu criterion inverse re-serve factor. Bottom view of sample 6b.

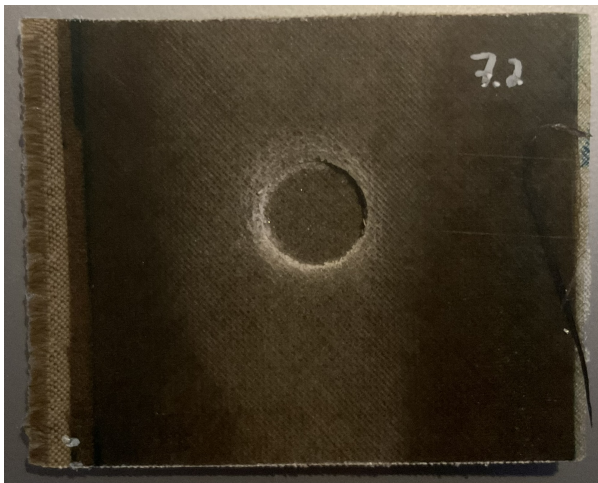


Figure 4.81: Top view of the sample 6b.

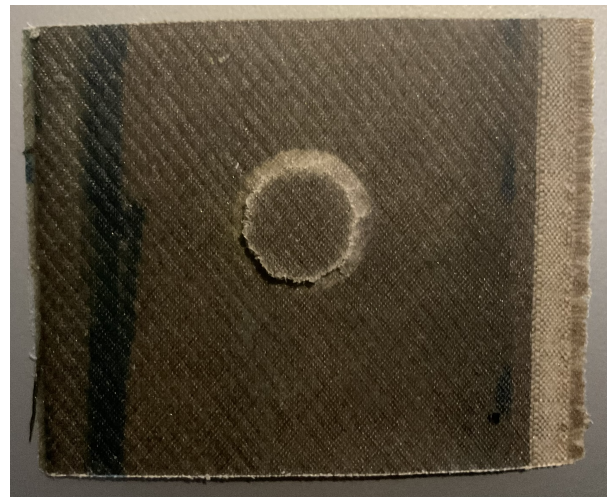


Figure 4.82: Bottom view of the sample 6b.

4.5 Conclusion

The simulations presented in this chapter demonstrate the feasibility of developing a reliable numerical model with a multistep solution for the shear test. However, significant simplifications of this model are not possible, making it necessary to include both frictional contact modeling and large deflection analysis of the sample. Despite this, the contact model employed is not entirely perfect from a numerical standpoint and may lead to stress and failure results that do not always align precisely with experimental data.

Modeling damage is a highly complex topic that needs further exploration in the future. Although achieving the highest accuracy in simulating these damages was not possible, the force-displacement curves obtained numerically are highly reliable and can be used to study various parameters involved in lay-up design.

CHAPTER 5

Conclusion

The aim of this thesis was to find a more sustainable composite lay-up for a Formula Student race car monocoque, allowing for mechanical properties equivalent to carbon fiber while maintaining a similar weight. This objective was achieved by dividing the study into two key components: an experimental chapter focused on investigating the influence of stacking sequence and flax fiber mass fraction on the properties of hybrid composites, and a numerical chapter aimed at modeling the shear test in Ansys to optimize the testing strategy for the composite materials currently in use. All the steps related to this new testing strategy have been thoroughly covered in this work, from the lay-up design to experimental testing, including numerical simulations and sample fabrication. The findings indicate that carbon-flax hybrid composites are promising materials for use in monocoque structures, particularly for areas subject to impacts, such as the front bulkhead. However, further optimization and accurate modeling through finite element simulations remain complex challenges that warrant in-depth investigation in the future.

Chapter 2 provided a theoretical examination of composite materials as a whole to identify potential alternatives to carbon fiber. Due to their low carbon footprint, flax fibers immediately showed promising potential. They are the only natural fibers that have reached a certain level of industrial maturity while offering satisfactory mechanical properties. Unlike the current applications of these fibers, a monocoque structure requires materials with very high strength and stiffness. The solution adopted was to create a carbon-flax hybrid composite that combines the strength of carbon fibers with the toughness of natural fibers, allowing the resulting composites to remain functional even under overload conditions. A study of the properties of these hybrid materials quickly revealed their superior impact resistance compared to carbon fiber, further reinforcing their relevance for use in a monocoque structure.

In the Chapter 3, vacuum-assisted resin infusion method was used to produce high-quality hybrid composites. It was noted that the main issue with hybrid composites is the high absorption rate of epoxy resin, leading to an increase in the composite's mass and a reduction in its mechanical properties. Thanks to the experimental perimeter tests conducted on hybrid samples, it was concluded that the hybridization of carbon fibers with flax fibers appears to have a positive effect on the results. The study revealed that the stacking sequence and flax fiber mass ratio are the parameters that most significantly influence the performance of hybrid composites. By placing flax fiber in the outer layers and alternating carbon and flax fibers within the lay-up, it is possible to achieve a maximum force of 27454 [N] with only 10 fiber layers. Therefore, it would theoretically be possible to use a hybrid composite in the skins that make up the front bulkhead structure, thereby reducing its mass by at

least 22% and its CO₂ footprint by 43.21%, provided that a more advanced optimization is carried out beforehand.

Finally, Chapter 4 demonstrated that it is possible to create a reliable numerical model of the perimeter shear test. A study of different contact types led to the conclusion that a model incorporating frictional contacts and accounting for large deflections closely matches the experimental results. Damage modeling was implemented to determine the first ply failure. Despite some discrepancies in the numerical results, the force-displacement curves obtained are highly accurate and permit to determine the first ply failure of the sample. They can therefore be used to study various parameters involved in lay-up design. However, this type of simulation is highly complex, making it challenging to accurately simulate the complete failure of the sample.

Future work

As mentioned repeatedly throughout this work, the present results leave room for future developments.

Firstly, the use of pre-impregnated flax fibers appears essential for integrating hybrid composites into the monocoque. This would simplify the manufacturing processes, improve mechanical properties, and further reduce the weight of the components. It would enable the testing of different front bulkhead prototypes to optimize the amount of unidirectional and woven fibers and determine the optimal ply orientations. Additionally, more reliable mechanical properties could be obtained through data sheets, allowing for more accurate simulations of flax fiber samples.

Secondly, before even considering simulating the entire sandwich structure, it would be beneficial to improve the damage models used to achieve a better representation of composite failure. Implementing delamination in the current model would also enable more realistic simulations of hybrid samples. The material model MAT54/55 used in LS-DYNA is able to simulate damage progression in dynamic failure simulations. Its advantage is that it is very well-documented and many parameters for modeling the failure of carbon and flax fibers have already been determined. However, the simulation parameters would need to be adapted to reproduce the quasi-static conditions of the perimeter shear test. Finally, to reduce the computational cost of simulations, it could be considered to model only half of the geometry in the case of symmetrical lay-ups.

References

- [1] Formula Student Germany. *Chronicle*. <https://www.formulastudent.de/about/chronicle/>. Accessed: 10/07/2024. 2022.
- [2] Institution of Mechanical Engineers. *About Formula Student*. <https://www.imeche.org/events/formula-student/about-formula-student>. Accessed: 10/07/2024. 2024.
- [3] Formula Electric Belgium. *Aerodynamics banner*. Accessed: 14/04/2024. 2024.
- [4] Jin Zhang et al. “Past, present and future prospective of global carbon fibre composite developments and applications”. In: *Composites Part B: Engineering* 250 (2023), p. 110463. ISSN: 1359-8368. DOI: <https://doi.org/10.1016/j.compositesb.2022.110463>. URL: <https://www.sciencedirect.com/science/article/pii/S1359836822008368>.
- [5] Irene Jerez Sotoca. “Impact Damage Modelling on Composite Structures”. MA thesis. Liège, Belgium: University of Liège, 2022-2023.
- [6] “McLaren: 40 years in the lead in automotive carbon fiber”. In: *Reinforced Plastics* 65.6 (2021), pp. 34–37. ISSN: 0034-3617. DOI: [https://doi.org/10.1016/S0034-3617\(21\)00272-1](https://doi.org/10.1016/S0034-3617(21)00272-1). URL: <https://www.sciencedirect.com/science/article/pii/S0034361721002721>.
- [7] Siyuan Zhang et al. “Environmental impacts of carbon fiber production and decarbonization performance in wind turbine blades”. In: *Journal of Environmental Management* 351 (2024), p. 119893. ISSN: 0301-4797. DOI: <https://doi.org/10.1016/j.jenvman.2023.119893>. URL: <https://www.sciencedirect.com/science/article/pii/S0301479723026816>.
- [8] Sanjay Mavinkere Rangappa et al. *Plant Fibers, their Composites, and Applications*. en. Woodhead Publishing, May 2022.
- [9] Formula Student Germany. *Formula Student Rules 2024*. Germany: Formula Student Germany, 2023-2024.
- [10] David Krzikalla et al. “Analysis of Torsional Stiffness of the Frame of a Formula Student Vehicle”. In: *Journal of Applied Mechanical Engineering* 08.01 (2019). DOI: 10.35248/2168-9873.19.8.315. URL: <http://dx.doi.org/10.35248/2168-9873.19.8.315>.
- [11] *Encyclopedia of Continuum Mechanics*. Springer Berlin Heidelberg, 2020. ISBN: 9783662557716. DOI: 10.1007/978-3-662-55771-6. URL: <http://dx.doi.org/10.1007/978-3-662-55771-6>.
- [12] Formula Electric Belgium. *Formula Wiki: Monocoque*. <https://formula-wiki.yfrickx.be/index.php/Category:Monocoque>. Accessed: 07/03/2024. 2024.
- [13] Marco Nevache. “FSAE Monocoque Design and Composite Materials Testing”. MA thesis. Torino, Italia: Politecnico di Torino, 2023.

-
- [14] Anni Wang et al. “Effect of volume ratio and hybrid mode on low-velocity impact properties of unidirectional flax/carbon fiber hybrid reinforced polymer composites”. In: *Thin-Walled Structures* 187 (2023), p. 110764. ISSN: 0263-8231. DOI: <https://doi.org/10.1016/j.tws.2023.110764>. URL: <https://www.sciencedirect.com/science/article/pii/S0263823123002422>.
 - [15] Anni Wang et al. “Tensile properties hybrid effect of unidirectional flax/carbon fiber hybrid reinforced polymer composites”. In: *Journal of Materials Research and Technology* 24 (2023), pp. 1373–1389. ISSN: 2238-7854. DOI: <https://doi.org/10.1016/j.jmrt.2023.03.078>. URL: <https://www.sciencedirect.com/science/article/pii/S2238785423005410>.
 - [16] Textile Technology. *Replacing carbon with flax*. <https://www.textiletechnology.net/fibers/trendreports/bmwbcomp-replacing-carbon-with-flax-33208>. Accessed: 02/07/2024. 2022.
 - [17] Bcomp. *Porsche’s Mission R Concept is Built with Natural Fibre Parts*. <https://www.bcomp.com/news/porsches-mission-r-concept-is-built-with-natural-fibre-parts/>. Accessed: 02/07/2024. 2022.
 - [18] YCOM. *WORLD-FIRST SUSTAINABLE ALTERNATIVE TO CARBON-FIBRE REVEALED FOR MOTORSPORT CRASH STRUCTURES*. <https://www.ycom.it/natural-fibre-crash-box-ycom-bcomp/>. Accessed: 02/07/2024. 2020.
 - [19] Robin Wikström. “Composite optimization of FSAE Chassis”. MA thesis. Stockholm, Sweden: KTH Royal Institute of Technology, 2022-2023.
 - [20] Łukasz Święch, Radosław Kołodziejczyk, and Natalia Stącel. “Experimental Analysis of Perimeter Shear Strength of Composite Sandwich Structures”. In: *Materials* 14.1 (2021). ISSN: 1996-1944. DOI: 10.3390/ma14010012. URL: <https://www.mdpi.com/1996-1944/14/1/12>.
 - [21] Jeff Flynn, Ali Amiri, and Chad Ulven. “Hybridized carbon and flax fiber composites for tailored performance”. In: *Materials Design* 102 (2016), pp. 21–29. ISSN: 0264-1275. DOI: <https://doi.org/10.1016/j.matdes.2016.03.164>. URL: <https://www.sciencedirect.com/science/article/pii/S0264127516304579>.
 - [22] Katharina Henschel, Nicolas André, and Manfred Hajek. “Hybrid Natural Fiber Composites in a Helicopter Cabin Door - Mechanical Properties and Ecological Efficiency”. In: (May 2019). DOI: 10.4050/F-0075-2019-14721.
 - [23] Rostislav Svidler and R. Rinberg. “Bio-based hybrid cabin door of ultralight helicopter with variable-axis fiber design”. In: *CEAS Aeronautical Journal* 14.1 (Oct. 2022), pp. 115–125. ISSN: 1869-5590. DOI: 10.1007/s13272-022-00617-y. URL: <http://dx.doi.org/10.1007/s13272-022-00617-y>.
 - [24] Carl Andersson Eurenus et al. “Analysis of Composite Chassis”. BA thesis. Göterborg, Sweden: Chalmers University of Technology, 2013-2014.
 - [25] Michaël Bruyneel. *Mechanics of composites*. Liège, Belgium: University of Liège, 2022-2023.
 - [26] Liliana Bejan and V.F. Poterasu. “Woven composite material design by orthotropic compliance averaging method using mathematica”. In: *Computer Methods in Applied Mechanics and Engineering* 179.1 (1999), pp. 53–65. ISSN: 0045-7825. DOI: [https://doi.org/10.1016/S0045-7825\(99\)00040-7](https://doi.org/10.1016/S0045-7825(99)00040-7). URL: <https://www.sciencedirect.com/science/article/pii/S0045782599000407>.
-

-
- [27] Warren C. Young and Richard G. Budynas. *Roark's Formulas for Stress and Strain*. Liège, Belgium: McGraw-Hill, 2002. ISBN: 0-07-072542-X.
 - [28] Silvestre Pinho et al. "Failure Models and Criteria for FRP Under In-Plane or Three-Dimensional Stress States Including Shear Non-Linearity". In: (Mar. 2005).
 - [29] Bhagwan D. Agarwal, Lawrence J. Broutman, and K. Chandrashekhara. *Analysis and performance of Fiber Composites*. Wiley, 2018.
 - [30] Marcus Andersson and Petter Liedberg. "Analysis of Composite Chassis". MA thesis. Göterborg, Sweden: Crash behavior of composite structures, 2013-2014.
 - [31] Jacob Aboudi, Steven Arnold, and Brett Bednarczyk. "4 - Failure criteria and margins of safety". In: *Practical Micromechanics of Composite Materials*. Ed. by Jacob Aboudi, Steven Arnold, and Brett Bednarczyk. Butterworth-Heinemann, 2021, pp. 161–214. ISBN: 978-0-12-820637-9. DOI: <https://doi.org/10.1016/B978-0-12-820637-9.00008-8>. URL: <https://www.sciencedirect.com/science/article/pii/B9780128206379000088>.
 - [32] Muhammad Ilyas. "Damage modelling of carbon epoxy laminated composites submitted to impact loading". PhD thesis. Institut Supérieur de l'Aéronautique et de l'Espace, 2010.
 - [33] L. Ouwehand, ed. *Damage Modeling of Composites and Reliability Analysis*. Vol. 727. ESA Special Publication. June 2014, 102, p. 102.
 - [34] Ansys. *Ansys Help: 4.22. Material Damage*. https://ansyshelp.ansys.com/account/secured?returnurl=/Views/Secured/corp/v201/en/ans_mat/mat_damageall.html?q=damage. Accessed: 25/07/2024. 2020.
 - [35] Umeyr Kureemun et al. "Effects of hybridization and hybrid fibre dispersion on the mechanical properties of woven flax-carbon epoxy at low carbon fibre volume fractions". In: *Composites Part B: Engineering* 134 (2018), pp. 28–38. ISSN: 1359-8368. DOI: <https://doi.org/10.1016/j.compositesb.2017.09.035>. URL: <https://www.sciencedirect.com/science/article/pii/S1359836816326981>.
 - [36] H.N. Dhakal et al. "Development of flax/carbon fibre hybrid composites for enhanced properties". In: *Carbohydrate Polymers* 96.1 (2013), pp. 1–8. ISSN: 0144-8617. DOI: <https://doi.org/10.1016/j.carbpol.2013.03.074>. URL: <https://www.sciencedirect.com/science/article/pii/S014486171300324X>.
 - [37] Anni Wang, Xiaojun Wang, and Guijun Xian. "The influence of stacking sequence on the low-velocity impact response and damping behavior of carbon and flax fabric reinforced hybrid composites". In: *Polymer Testing* 104 (2021), p. 107384. ISSN: 0142-9418. DOI: <https://doi.org/10.1016/j.polymertesting.2021.107384>. URL: <https://www.sciencedirect.com/science/article/pii/S0142941821003299>.
 - [38] Eric Béchet. *Private communication*. 2024.
 - [39] Emmanuel Chukwueloka Onyibo and Babak Safaei. "Application of finite element analysis to honeycomb sandwich structures: a review". In: *Reports in Mechanical Engineering* 3.1 (Dec. 2022), pp. 283–300. ISSN: 2683-5894. DOI: 10.31181/rme20023032022o. URL: <http://dx.doi.org/10.31181/rme20023032022o>.
 - [40] D. Zenkert. *An Introduction to Sandwich Construction*. Engineering Materials Advisory Services, 1995. ISBN: 9780947817770. URL: <https://books.google.be/books?id=zc-GQgAACAAJ>.
 - [41] Jean-Philippe Ponthot. *Finite Element Method*. Liège, Belgium: University of Liège, 2021-2022.
-

-
- [42] Özgün Sunar. *3 Tips to Improve Your FE Model*. <https://www.mechhead.com/3-tips-to-improve-your-fe-model/>. Accessed: 03/05/2024. 2021.
 - [43] Michael Heitzer and Manfred Staat. “Basis reduction technique for limit and shakedown problems”. In: Central Institute for Applied Mathematics, Feb. 2003, pp. 1–55. ISBN: 3-00-0100001-6.
 - [44] Nitin Garg and Chung-Souk Han. “A penalty finite element approach for couple stress elasticity”. In: *Computational Mechanics* 52 (Sept. 2013), pp. 709–720. DOI: 10.1007/s00466-013-0842-y.
 - [45] M. Mofakhami and Christian Boller. “Scattering of Lamb waves from edge cracks in circular holes for understanding damage detection in more complex structures”. In: *Materials Forum* 33 (Jan. 2009).
 - [46] Ansys. *Introduction to Connections*. Ansys Innovation Space, 2020.
 - [47] P.D. Herrington and M. Sabbaghian. “Factors affecting the friction coefficients between metallic washers and composite surfaces”. In: *Composites* 22.6 (1991), pp. 418–424. ISSN: 0010-4361. DOI: [https://doi.org/10.1016/0010-4361\(91\)90198-P](https://doi.org/10.1016/0010-4361(91)90198-P). URL: <https://www.sciencedirect.com/science/article/pii/001043619190198P>.
 - [48] Anthony Opoku, Satyanarayan Panigrahi, and Lope Tabil. “Frictional properties of natural and chemically-treated flax fibers”. In: vol. 13. Jan. 2007. DOI: 10.13031/2013.23461.
 - [49] Ansys Learning. *Designating the Contact and Target Sides Properly*. <https://youtu.be/yUhTaTwM-c4?si=LTnzokAYkdnMwxj0>. Accessed: 05/04/2024. 2020.
 - [50] Ansys. *Lecture 2- Ansys Mechanical- Introduction to Structural Nonlinearities*. Ansys Innovation Space, 2020.
 - [51] FEA tips. *Ansys Solver Control Settings Explained*. <https://featips.com/2023/05/15/ansys-solver-control-settings-explained/>. Accessed: 05/04/2024. 2023.
 - [52] Özgün Sunar. *What is Large Deflection in Ansys?* <https://www.mechhead.com/what-is-large-deflection-in-ansys/>. Accessed: 09/08/2024. 2023.
 - [53] Mallett Technology. *Nonlinear contacts in ANSYS - Best practices for convergence*. <https://youtu.be/O-qTAiE8Kdo?si=tOaJEBlD5iSctDj>. Accessed: 20/04/2024. 2019.
 - [54] EDRMedeso. *How to achieve convergence in Ansys Mechanical : Modeling contact | Ansys Tutorials*. https://youtu.be/sZf5p_evq0k?si=7tr_tcdBmw68e2vD. Accessed: 20/04/2024. 2021.
 - [55] Ansys. *CONVERGENCE PROBLEMS IN STATIC STRUCTURAL ANALYSIS WITH FRICTION CONTACT*. <https://innovationspace.ansys.com/forum/forums/topic/convergence-problems-in-static-structural-analysis-with-friction-contact/>. Accessed: 20/04/2024. 2021.
 - [56] Özgün Sunar. *3 Tips to Improve Your FE Model*. <https://www.mechhead.com/what-is-large-deflection-in-ansys/>. Accessed: 24/08/2024. 2021.
 - [57] National Research Council. *High-Performance Structural Fibers for Advanced Polymer Matrix Composites*. Washington, DC: The National Academies Press, 2005. ISBN: 978-0-309-09614-0. DOI: 10.17226/11268. URL: <https://nap.nationalacademies.org/catalog/11268/high-performance-structural-fibers-for-advanced-polymer-matrix-composites>.
-

-
- [58] Jai Singh, Singh Sehijpal, and Vikas Dhawan. “Effect of Curing Temperature on Mechanical Properties of Natural Fiber Reinforced Polymer Composites”. In: *Journal of Natural Fibers* 15 (Sept. 2017). DOI: 10.1080/15440478.2017.1354744.
- [59] Silvia Hernández Rueda. “Curing, Defects and Mechanical Performance of Fiber-Reinforced Composite”. PhD thesis. Escuela Técnica Superior de Ingenieros de Caminos, Canales y Puertos, 2013.
- [60] Composites Today. *Quality issues related to usage of expired and off-spec carbon fiber prepreg*. <https://www.compositestoday.org/quality-issues-related-to-usage-of-expired-and-off-spec-carbon-fiber-prepreg/>. Accessed: 24/06/2024. 2024.
- [61] Ansys. *Ansys Help: 3.9.3. Solid Elements*. https://ansyshelp.ansys.com/public/account/secured?returnurl=////Views/Secured/corp/v242/en/acp_ug/solid_elements_acp.html. Accessed: 25/07/2024. 2020.
- [62] Marie Puissant. “Structural modelling, testing and correlation of the Athena X-IFU Aperture Cylinder composite structure and investigation of its thermo-mechanical topology optimisation”. MA thesis. Liège, Belgium: University of Liège, 2022-2023.
- [63] Hexcel. *E-Documents*. <https://www.hexcel.com/Resources/DataSheets/Prepreg>. Accessed: 2/05/2024. 2024.
- [64] Michaël Bruyneel. *Private communication*. 2024.
- [65] Elena Raponi et al. “Temperature effect on impact response of flax/epoxy laminates: Analytical, numerical and experimental results”. In: *Composite Structures* 274 (2021), p. 114316. ISSN: 0263-8223. DOI: <https://doi.org/10.1016/j.compstruct.2021.114316>. URL: <https://www.sciencedirect.com/science/article/pii/S0263822321007789>.
- [66] Benedict Lawrence Sy, Zouheir Fawaz, and Habiba Bougherara. “Numerical simulation correlating the low velocity impact behaviour of flax/epoxy laminates”. In: *Composites Part A: Applied Science and Manufacturing* 126 (2019), p. 105582. ISSN: 1359-835X. DOI: <https://doi.org/10.1016/j.compositesa.2019.105582>. URL: <https://www.sciencedirect.com/science/article/pii/S1359835X19303318>.